

KINETIC NUMERICAL SIMULATIONS OF PARTICLE ACCELERATION MECHANISMS IN RELATIVISTICALLY MAGNETIZED JETS

Author: José Ortuño-Macías
Supervisor: Dr hab. Krzysztof Nalewajko



A thesis submitted for the degree of
Doctor of Philosophy

from the

Nicolaus Copernicus Astronomical Center
Polish Academy of Sciences

August 2022

Contents

Abstract	3
Acknowledgements	7
1 Introduction	8
1.1 Jets of Active Galactic Nuclei	8
1.1.1 Jets characteristics	9
1.1.2 Radiative processes in jets	12
1.2 Blazars	14
1.2.1 Non-thermal emission from other high-energy astrophysical phenomena	15
1.3 Particle acceleration mechanisms	16
1.3.1 Fermi mechanism	16
1.3.2 Magnetized turbulence	17
1.3.3 Magnetic Reconnection	17
1.3.4 Instabilities of magnetized jets	20
1.4 Particle-In-Cell kinetic simulations	23
1.4.1 ZELTRON code	26
1.5 Simulation details	28
1.5.1 Implementation of open boundary condition for the RMR simulations	28
1.5.2 Implementation of plasmoid tracker for the RMR simulations	30
1.6 Motivation and thesis overview	31
1.6.1 Paper I: Radiative kinetic simulations of steady-state relativistic plasmoid magnetic reconnection	31
1.6.2 Paper II: Kinetic Simulations of Instabilities in Cylindrical Magnetized Jets	32
1.7 Future prospects	33
2 Paper 1: Radiative kinetic simulations of steady-state relativistic plasmoid magnetic reconnection	35
3 Paper 2: Kinetic simulations of instabilities and particle acceleration in cylindrical magnetized relativistic jets	53
Bibliography	76

Abstract

Around 10% of galaxies that present Active Galactic Nuclei (AGN) produce relativistic jets. These jets are collimated relativistic outflows of plasma and magnetic fields. Jets, among other high-energy astrophysical phenomena, such as gamma-ray bursts, and pulsar wind nebulae, present non-thermal emission signatures originating from non-thermal particle energy distributions. These particle distributions result from non-thermal acceleration in low-density collisionless plasma environments. In addition, from observations of synchrotron emission, magnetic fields are thought to play a fundamental role in the particle acceleration and radiation processes. These two conditions, low densities and strong magnetic fields, imply relativistic magnetizations, which means that the magnetic energy density dominates the rest-mass energy density of matter.

For a long time, it has been under debate which dissipation mechanism (in particular shock waves or magnetic reconnection) best suits the observed emission signatures, how efficient it is, and where exactly it happens. It has been only during the last years when kinetic simulations became available to investigate from first principles the effects of instabilities beyond their linear phases in relativistically magnetized plasmas, the results of those simulations are being adapted to emission models in order to explain observations.

The main topic of this thesis is the analysis of two particle acceleration mechanisms in relativistically magnetized jets through particle-in-cell (PIC) kinetic simulations. The mechanisms studied are: (1) the steady-state relativistic magnetic reconnection, and (2) the current- and pressure-driven instabilities of cylindrical magnetized jets.

Chapter 2, which consists of the paper [Ortuño-Macías and Nalewajko \(2020\)](#), presents the results of 2D PIC simulations of radiative relativistic magnetic reconnection in pair plasma, where the steady-state was achieved by means of open boundaries, that allows for unimpeded outflows. We included radiation reaction due to the synchrotron process and we regulated the radiative cooling efficiency by the choice of initial plasma temperature. We confirmed the anti-correlation between plasmoid size and plasmoid velocities found in [Sironi et al. \(2016\)](#), hence small plasmoids are relatively fast and large plasmoids are slow. We observed that the relativistic outflows between plasmoids (minijets) have small contribution to observed radiation because of their low densities. We found that main contributors to the observed emission are large/slow plasmoids with the major part of the radiation originating from their central cores. The obtained synchrotron lightcurves show conspicuous signatures in the form of rapid bright flares that we identified as being produced at tail-on merger events between small/fast and large/slow plasmoids.

The second paper [Ortuño-Macías et al. \(2022\)](#), contained in Chapter 3, presents the results of 3D kinetic simulations of cylindrical relativistically magnetized jets populated with electron-positron pair plasma. Our simulation setup was designed to bridge between the two models considered before, the

pressure balanced configuration studied by [Alves et al. \(2018\)](#), and the force-free configuration studied by [Davelaar et al. \(2020\)](#), using a single parameter that defines how much pressure is asserted by the gas over the pressure and tension of the toroidal component of the magnetic field. We also investigated the effect of the power-law index of the radial profile of the toroidal magnetic field. We argue that the particle energy limit found by [Alves et al. \(2018\)](#) is due to the finite duration of the fast magnetic dissipation phase. For any of the configurations studied, we found a rather minor contribution of the parallel electric field (associated with guide-field magnetic reconnection events) to particle acceleration. In all investigated cases kink modes arise from the central core of the jet. In the gas pressure-dominated cases, we also observe a comparable contribution of the pinch modes. We argue that pressure-driven modes are important where enough gas pressure is produced by other dissipation mechanisms.

Streszczenie

(Abstract in Polish)

Około 10% galaktyk posiadających aktywne jądra produkuje relatywistyczne dżety. Dżety te są skolimowanymi relatywistycznymi wypływami plazmy oraz pól magnetycznych. Dżety, a także inne wysokoenergetyczne zjawiska astrofizyczne, takie jak błyski gamma czy mgławice pulsarowe, prezentują nietermiczne sygnały promieniowania pochodzące od nietermicznych rozkładów energii cząstek. Te rozkłady cząstek wynikają z nietermicznego przyspieszania w środowisku bezkolizyjnej plazmy o niskiej gęstości. Dodatkowo, z obserwacji emisji synchrotronowej uważa się, że pola magnetyczne odgrywają fundamentalną rolę w przyspieszaniu cząstek oraz w procesach promienistych. Te dwa warunki, niskie gęstości oraz silne pola magnetyczne, implikują relatywistyczne magnetyzacje, co oznacza, że gęstość energii magnetycznej dominuje nad gęstością energii spoczynkowej materii.

Przez długi czas debatowano, który mechanizm dysypacji (w szczególności fale uderzeniowe czy rekoneksja pól magnetycznych) najlepiej odpowiada obserwowanym sygnałom promieniowania, jak efektywny jest ów mechanizm i gdzie dokładnie zachodzi. Dopiero w ciągu ostatnich lat symulacje kinetyczne stały się narzędziem do badania od podstaw efektów niestabilności, wychodząc poza ich fazę liniową, w relatywistycznie zmagetyzowanych plazmach, a wyniki tych symulacji są stosowane w modelach emisji pozwalających na wyjaśnienie obserwacji.

Głównym tematem tej rozprawy jest analiza dwóch mechanizmów przyspieszania cząstek w relatywistycznie zmagetyzowanych dżetach poprzez kinetyczne symulacje typu „cząstka w komórce” (ang. „particle-in-cell”; PIC). Mechanizmami tymi są: (1) stacjonarna relatywistyczna rekoneksja pól magnetycznych oraz (2) niestabilności napędzane prądem lub ciśnieniem gazu w cylindrycznym zmagetyzowanym dżecie.

Rozdział 2, który stanowi publikacja [Ortuño-Macías and Nalewajko \(2020\)](#), przedstawia wyniki dwuwymiarowych symulacji PIC relatywistycznej rekoneksji pól magnetycznych w promieniującej plazmie elektronowo-pozytronowej, gdzie stacjonarność uzyskano poprzez otwarte warunki brzegowe pozwalające na swobodne wypływy. Uwzględniliśmy reakcję promienistą na proces synchrotronowy, natomiast efektywność chłodzenia promienistego regulowana była poprzez wybór początkowej temperatury plazmy. Potwierdziliśmy antykorelację pomiędzy rozmiarami a prędkościami plazmoidów wykazaną w pracy [Sironi et al. \(2016\)](#), co oznacza, że małe plazmoidy są szybkie, a duże plazmoidy są wolne. Zauważyliśmy, że relatywistyczne wypływy pomiędzy plazmoidami (minidżety) mają niewielki wkład do obserwowanego promieniowania ze względu na ich niskie gęstości. Stwierdziliśmy, że główny wkład do obserwowanej emisji pochodzi od dużych/wolnych plazmoidów, w których najwięcej promieniowania produkowane jest w ich centralnych rdzeniach. Otrzymane synchrotronowe krzywe blasku wykazują

charakterystyczne sygnały w postaci szybkich i intensywnych pojaśnień, które zidentyfikowaliśmy jako produkowane podczas zderzeń pomiędzy plazmoidami małym/szybkim a dużym/wolnym poruszającymi się w tym samym kierunku.

Druga publikacja [Ortuño-Macías et al. \(2022\)](#), zawarta w Rozdziale 3, przedstawia wyniki trójwymiarowych symulacji kinetycznych cylindrycznych relatywistycznie zmagnetyzowanych dżetów wypełnionych plazmą elektronowo-pozytronową. Konfiguracja naszych symulacji została pomyślana jako pomost pomiędzy dwoma modelami rozważanymi dotychczas, pomiędzy konfiguracją podtrzymywaną ciśnieniem gazu (badaną w pracy [Alves et al., 2018](#)) a konfiguracją podtrzymywaną składową poloidalną pola magnetycznego (badaną w pracy [Davelaar et al., 2020](#)), używając jednego parametru, który określa ile ciśnienia wywieranego jest przez gaz w porównaniu z ciśnieniem oraz napięciem składowej toroidalnej pola magnetycznego. Badaliśmy także efekt indeksu potęgowego profilu radialnego toroidalnego pola magnetycznego. Pokazujemy, że limit na energię cząstek określony w pracy [Alves et al. \(2018\)](#) wynika ze skończonego czasu trwania tzw. szybkiej fazy dysypacji magnetycznej. Dla każdej z badanych konfiguracji stwierdziliśmy niewielki wkład od równoległych pól elektrycznych (związanych z obszarami rekoneksji magnetycznej z tzw. polem wiodącym) do przyspieszania cząstek. We wszystkich badanych przypadkach mody typu kink narastają od centralnego rdzenia dżetu. W przypadkach zdominowanych ciśnieniem gazu obserwujemy także porównywalny wkład modów typu pinch. Argumentujemy, że mody napędzane ciśnieniem gazu są istotne tam, gdzie ciśnienie gazu produkowane jest przez inne mechanizmy dysypacyjne.

Acknowledgements

This thesis not only contains the scientific work done during my Ph.D. studies but also represents life experiences that will accompany me wherever I go. I would like to express my gratitude to everyone, including persons not mentioned here, who strongly influenced me through meaningful moments.

First and foremost, I would like to thank my supervisor, Dr hab. Krzysztof Nalewajko, for his dedication, patience, and support at every stage of the Ph.D. I am sure that without his continuous help I could not have accomplished the goals of our research work.

I would like to acknowledge the technical and administrative staff of the Nicolaus Copernicus Astronomical Center for their kindness and support, especially during the first years of studies when every process was new.

Definitely, I have to thank my parents for their immeasurable help through all these years. They were always keen on providing advice during the difficult moments that I faced. They, together with professors from my high school and university, triggered and encouraged my motivation to study Astrophysics.

During these years abroad, I would not have been able to feel comfortable without supportive friends back in Spain, where I always share a heartwarming feeling with them no matter how long it was without seeing each other. For that, I would like to thank Adrián, Andrés, Edgard, Jesús, Juan Miguel, Pablo, and Víctor.

Undoubtedly, I must thank the friends made here, Agostino, David, Dorota, Dominik, Ekaterina, Filip, Gonzalo, Katarzyna, Nicole, and Saikruba. Without your constant source of joy and support throughout the whole Ph.D. path, I could not have reached where I am.

Last but not least, I would like to recognize the support provided by my partner, Karolina. The last stage of my Ph.D. path was one of the most stressful moments in my life and her affection, empathy, and motivation helped tremendously to mitigate the complicated moments.

Chapter 1

Introduction

1.1 Jets of Active Galactic Nuclei

Active galactic nuclei (AGN) have been extensively sampled through observations over all the electromagnetic spectrum. Certain galaxies present active nuclei that have luminosities higher than common galaxies, in particular at high energies (X rays and gamma rays) and in the radio. AGN can be classified in several ways. One classification depends on whether the host galaxy is visible or not, as the emission from the central region could outshine the star emission of the host galaxy, they are named Seyfert galaxies and quasars, respectively. Another classification is based on the presence of broad emission lines, type 1 AGN present spectra with broad and narrow lines, while type 2 AGN only show narrow lines.

The engine of the active nucleus is an accretion disk that is dragging material onto a central supermassive black hole (SMBH). The accretion disk is surrounded by a puffed torus that obscures the emission that passes through it (see Fig. 1.1). It is thought that the observation of broad emission lines depends on the viewing angle at which we observe the galaxy, i.e., if there is no obscuring torus in our line of sight, we will see the inner part of the accreting zone where the emission regions present high-velocity dispersion, $\sim 10^3$ km/s, that generate the broadening of the spectral lines (Urry and Padovani, 1995).

Radio observations show that AGN present differences in radio luminosity. Depending on the ratio of the radio and optical luminosities, AGN can be classified as radio loud (RL) or radio quiet (RQ). About 10 % of the AGN are RL (e.g., de Vries et al., 2006), whose radio emission is identified as being produced at their relativistic jets and regions where these jets interact with the intergalactic medium. The remaining 90 % of observed AGN are classified as RQ and their low radio emissions are due to weak jets or lack of them.

Besides, among radio galaxies, two types can be distinguished: Fanaroff-Riley (FR) I and FR II (Fanaroff and Riley, 1974). The former, i.e., FR I class, shows the highest radio brightness from the inner jet close to the nucleus. The jet gradually decreases its brightness and steepens the spectrum with distance from the jet source. The second class, FR II, on the other hand, presents the highest radio brightness from hotspots at the ends of the jets, where they collide with the extragalactic medium. When they present double-sided jets, see Fig. 1.2, they often are roughly symmetric in size and brightness (although knots, jet regions with higher brightness, are not symmetrically distributed along both jets). The jet that bridges the central active nucleus and the hotspot, propagates approximately in a straight

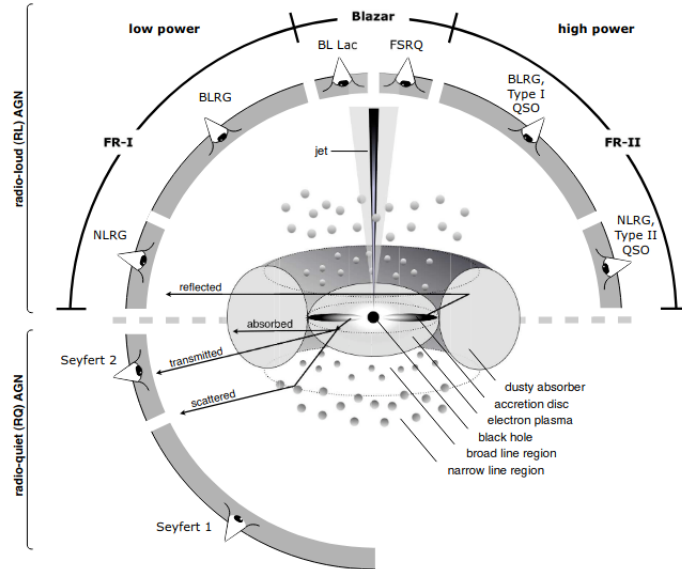


Figure 1.1: Representation of the unified scheme for AGN (Urry and Padovani, 1995). The type of object observed depends on the viewing angle, the power of the AGN engine, and the efficiency of the jet production. From Beckmann and Shrader (2012).

direction, and in some cases radio emitting plasma, after passing through the lobes, flows back (e.g., Leahy and Williams, 1984).

Jets are thought to be collimated relativistic outflows of plasma and magnetic fields originating from the AGN powered by the accretion of matter onto the SMBH (Kellermann et al., 2016; Madejski and Sikora, 2016; Blandford et al., 2019). The two main mechanisms for jet launching are: the Blandford-Znajek mechanism, in which energy and angular momentum are extracted electromagnetically from the spinning SMBH (Blandford and Znajek, 1977); and the Blandford-Payne mechanism, in which the energy and angular momentum are extracted from the accretion disk by magnetic stresses (Blandford and Payne, 1982).

1.1.1 Jets characteristics

Jet radio emission is thought to be produced by means of synchrotron emission, which requires magnetic fields, while inverse Compton radiation dominates at high energies (see subsection 1.1.2 on radiative processes). The study of the magnetic field structure is crucial for revealing how and where this emission is produced. The global picture of the magnetic field structure, its dissipation, and the mechanism of particle acceleration, are complex and have been under active investigation for a long time. For instance, Rees (1978) argued that M87 knots require in-situ particle acceleration provided by a local energy dissipation mechanism (shocks from jet velocity irregularities were proposed).

The magnetic field structure of a jet is often simplified to be formed of two main components, the poloidal magnetic field, i.e., in the direction of the jet axis, and the toroidal magnetic field in the azimuthal direction around the jet axis. As the jet outflows from the launching region, it expands roughly conically. It is expected that the plasma in the jet, due to being an electrically conducting fluid, carries magnetic field which is frozen into the fluid (according to the Alfvén's theorem). This

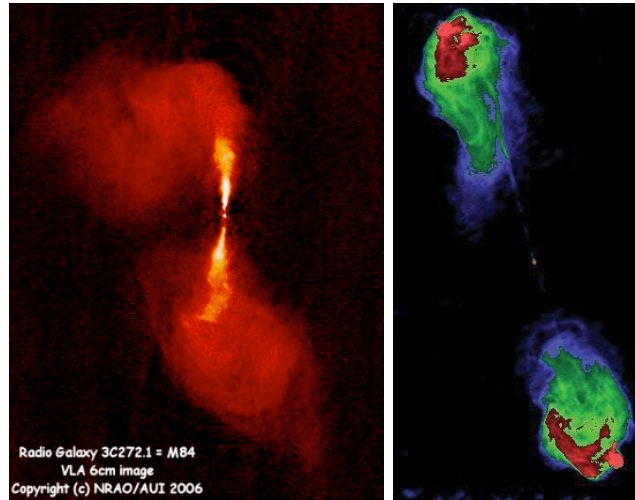


Figure 1.2: Radio galaxies M84 (3C272.1), a FRI radio galaxy; and Cygnus A (3C405), a FRII radio galaxy, observed by the Very Large Array (VLA) at the frequency of 5 GHz. Credits to the website Britannica and NRAO Charlottesville.

means that as the jet expands conically, the poloidal magnetic field decays with distance r as r^{-2} while the toroidal field decays as r^{-1} . Hence, even if the poloidal field is dominant at the onset of the jet, the toroidal field is likely to become dominant at some distance; as studies of the polarization of these objects have revealed, e.g., Gabuzda et al. (2004); Hovatta et al. (2012); Martí-Vidal et al. (2015); Wardle (2018). As the jet expands, the magnetic field strength decays, allowing the external medium pressure to constrain the expansion and recollimate the jet. A recent study of the jet magnetic field structure of M87, Pasetto et al. (2021), has shown that a helical magnetic field structure is present at large distances from the launching source ~ 1 kpc (projected on the plane of the sky).

Recollimation zones could be prone to MHD instabilities that dissipate magnetic fields and accelerate particles. For example, in the jet of M87 superluminal knots are found in the recollimation region HST-1, at ~ 70 pc (projected distance, i.e., apparent distance), (Biretta et al., 1999; Cheung et al., 2007) and polarimetric observations suggest that the jet is dominated by a toroidal magnetic field close to the SMBH, $\lesssim 0.2$ pc projected on the plane of the sky (Walker et al., 2018).

Jets are found to have a conical shape at large distances from their origin ($\sim 10^2 - 10^3$ parsecs) (Pushkarev et al., 2017) with a parabolic shape at sub-pc distances from the SMBH, where the acceleration to relativistic bulk velocities appears to happen (Asada et al., 2014). The change of the geometry might be an indicator of a transition from the Poynting flux-dominated outflow to particle kinetic flux-dominated outflow (Kovalev et al., 2020). This transition to particle kinetic flux-dominated has attracted the interest of astrophysicists for a long time (e.g., Begelman and Li, 1994); currently, it is thought that it requires a magnetic dissipation mechanism that may involve an interplay of thermal gas pressure and magnetic pressure (e.g., Giannios and Spruit, 2006).

Radio observations with very long baseline interferometry (VLBI) measure superluminal apparent motions (up to $v_{\text{app}} \sim 50c$) of knots along the jets. This is due to relativistic velocities, with $\beta = v/c \simeq 1$ the bulk speed of the emitting material normalized to the speed of light, and a small viewing angle $\Theta \sim 1/\gamma$, where $\gamma = (1 - \beta^2)^{-1/2}$ is the Lorentz factor, with the apparent speed described by the



Figure 1.3: Image of the M87 jet from the Hubble Space Telescope (Hubble Heritage Team; STScI/AURA; NASA/ESA). The visible jet is relativistically beamed because it is approaching us at a relatively small angle. Its knots move with apparent velocities up to $6c$, which is evidence of relativistic motions. From [Biretta et al. \(1999\)](#).

expression:

$$\beta_{\text{app}} = \frac{\beta \sin \Theta}{1 - \beta \cos \Theta}. \quad (1.1)$$

Emission from relativistic flows, $\gamma \gg 1$, is strongly affected by relativistic beaming, i.e., isotropically emitted photons in the rest frame of the emitting source, will be contained within an angle of $\theta \sim 1/\gamma$ in the forward direction in the SMBH rest frame. As in the case of M87, with knots traveling at relativistic speeds $\sim 6c$, it is common to observe only the jet moving toward us whose emission luminosity is enhanced by relativistic effects. On the other hand, the counter-jet is either faint or not detectable because its luminosity is diminished as it outflows away from us (see Fig. 1.3). In addition, the relativistic Doppler effect enhances the radiation frequency

$$\frac{\nu_{\text{obs}}}{\nu'_{\text{em}}} = \frac{1}{\gamma(1 - \beta \cos \Theta)} \sim \frac{\sqrt{1 - \beta^2}}{1 - \beta^2} \sim \gamma \quad (1.2)$$

and the radiation intensity

$$\frac{I_{\text{obs}}(\nu_{\text{obs}})}{I'_{\text{em}}(\nu'_{\text{em}})} = \left(\frac{\nu_{\text{obs}}}{\nu'_{\text{em}}} \right)^3 \sim \gamma^3 \quad (1.3)$$

where $I_{\text{obs}}(\nu_{\text{obs}})$ is the observed intensity, and $I'_{\text{em}}(\nu'_{\text{em}})$ is the emitted intensity.

Monitoring of blazar jets with VLBI reveals knots accelerating on distance scales up to 100 pc from the nucleus ([Lister et al., 2016](#)), which suggests that jets are still significantly magnetized beyond pc scales. Besides, gamma-ray emission is associated with jets of high bulk Lorentz factors ([Blandford et al., 2019](#)).

Theoretical studies suggest that jets are initially Poynting dominated (e.g., [Sikora et al., 2005](#)), i.e., the magnetic energy density is much higher than the kinetic energy density; and they become kinetically dominated and terminate the bulk acceleration at distances where MHD instabilities probably play a key role in the process. The dissipative mechanism responsible for the conversion of magnetic energy into particle kinetic energy has been long discussed (e.g., [Sironi et al., 2015](#)). These mechanisms may be related to the region where blazar activity events are produced (see Section 1.2). We will briefly describe the main particle acceleration mechanisms in Section 1.2.1.

Recollimation of jets by external pressure is thought to make them internally unstable and dissipative, where it would become prone to kink instability (see the review article [Begelman et al., 1984](#)). By means of global MHD simulations, [Tchekhovskoy and Bromberg \(2016\)](#) showed that jets with power

above a certain threshold are able to escape the galactic core before any instability fully disrupts them. This provides a reasonable explanation of the main process behind the Fanaroff–Riley dichotomy.

1.1.2 Radiative processes in jets

Synchrotron radiation

Synchrotron emission is produced when a charged particle is moving at relativistic speeds in the presence of magnetic fields. In magnetic field \mathbf{B} , the Lorentz force $\mathbf{F} = m\mathbf{a} = (q/c)(\mathbf{v} \times \mathbf{B})$ results in the gyration of charged particles. Accelerated charged particles emit photons that take away the particle energy at a rate of $P = (2q^2/3c^3)a^2$, where q is the electric charge and a the acceleration (Jackson, 1998). For a relativistic electron, the acceleration is $a = \gamma^2 v_\perp^2/r$ and the gyration frequency can be expressed as $\omega_B = v_\perp/r = eB/(\gamma m_e c)$. For an isotropic distribution of electrons with relativistic velocities, the average power emitted is

$$P_{\text{syn}} = \frac{4\sigma_T c}{3} \beta^2 \gamma^2 U_B \quad (1.4)$$

where $\sigma_T = 8\pi r_e^2/3$ is the Thomson cross-section, $\beta = v/c$ is the velocity normalized to the speed of light, $U_B = B^2/8\pi$ is the magnetic energy density, and $r_e = e^2/m_e c^2$ is the classical radius of the electron (Smith, 2012). For highly relativistic electrons, $\beta \approx 1$, the spectral power is

$$P_{\text{syn}}(\nu) = \frac{\sqrt{3}e^3 B}{m_e c^2} \frac{\nu}{\nu_c} \int_{\nu/\nu_c}^{\infty} d\xi K_{5/3}(\xi), \quad (1.5)$$

where $\nu_c = 3eB\gamma^2/4\pi m_e c$ is the critical synchrotron frequency and $K_{5/3}$ is a modified Bessel function of the second kind (Blumenthal and Gould, 1970).

The integration of the previous expression for a power-law energy distribution of particles, $N(E) \propto E^{-p}$, provides a total emitted power per frequency for non-thermal particle distribution:

$$P_{\text{syn, tot}}(\nu) \propto \nu^{-(p-1)/2} \quad (1.6)$$

(Rybicki and Lightman, 1979). Therefore, the power-law spectra observed in relativistic jets are identified as synchrotron emission originating from non-thermal particle energy distributions, relating the spectral index with the particle distribution index as, $s = (p - 1)/2$.

The synchrotron radiation is partially polarized (Rybicki and Lightman, 1979). The degree of polarization is quantified as the ratio of the intensity of the polarized radiation, I_{pol} , to the total intensity, I , which can be expressed as follows

$$\Pi \equiv \frac{I_{\text{pol}}}{I} = \frac{\sqrt{Q^2 + U^2 + V^2}}{I}, \quad (1.7)$$

where Q , U , and V are the Stokes parameters and V indicates the degree of circular polarization, Q indicates the linear polarization in a Cartesian basis (\hat{x}, \hat{y}) , and U indicates the linear polarization in a Cartesian basis rotated $\pi/4$ rad (thus, the ratio Q/U determines the polarization angle). Hence, further knowledge about magnetic field structure in jets could be obtained from polarization studies, e.g., Kim et al. (2019).

Polarized radiation can be affected by Faraday rotation, a process by which the intrinsic polarization direction is rotated when passing through magnetized foreground plasma. The rotation of the polarization angle, θ_{rot} , is given by $\theta_{\text{rot}} = RM\lambda^2$ where λ is the radiation wavelength and RM is the

rotation measure that depends on the strength of the projected magnetic field along the line of sight B_{\parallel} , the density of charged particles n , and the thickness of the magnetized region L ,

$$RM = \frac{2\pi q^3}{m^2 c^2 \nu^2} \int_0^L n B_{\parallel} ds \quad (1.8)$$

(Rybicki and Lightman, 1979). Faraday rotation is important in understanding the polarization degree of observed synchrotron radiation, since it helps to estimate the strength and constrain the structure of magnetic fields across the jets, e.g., Zavala and Taylor (2004); Pushkarev et al. (2017).

Inverse Compton radiation

The scattering of low-energy photons by relativistic charged particles results in an energy transfer from the particles to the photons, a process known as Inverse Compton scattering and believed to be the main mechanism behind the gamma-ray emission of blazars and other AGN. The averaged energy loss rate by inverse Compton scattering for a single electron is given by the equation

$$P_{\text{IC}} = \frac{4}{3} \sigma_T c \gamma^2 \beta^2 U_{\text{ph}}, \quad (1.9)$$

with U_{ph} the energy density of low-energy photons. Comparing the energy losses for synchrotron and inverse Compton processes, one finds that

$$\frac{P_{\text{syn}}}{P_{\text{IC}}} = \frac{U_B}{U_{\text{ph}}}. \quad (1.10)$$

Similarly to the synchrotron spectrum, the inverse Compton spectral index for a power-law energy distribution of particles, $N(E) \propto E^{-p}$, is $s = (p - 1)/2$ (Blumenthal and Gould, 1970; Rybicki and Lightman, 1979).

Another radiative process is the synchrotron self-Compton (SSC). SSC is the inverse Compton upscattering of synchrotron photons produced by the same population of electrons. Motivated by the observed correlation of temporal variations between the low-energy and high-energy components of certain blazars (see Section 1.2), single-zone SSC models were proposed (Abdo et al., 2009; Potter and Cotter, 2012). In particular, SSC is often applied to modeling the high-energy component in low-luminosity high-energy peaked BL Lacs (HBLs).

Radiation reaction limit

Radiative processes constrain the energy gain of particles undergoing acceleration events. As the particle accelerates, the radiative losses increase until the moment when the acceleration and the radiation reaction force become equal. This moment defines the maximum energy achievable by the particles and it is known as the radiation reaction limit.

The radiation reaction limit for a relativistic electron radiating via synchrotron process can be estimated from the radiation reaction force

$$\mathbf{F}_{\text{syn}} = -\frac{2e^2}{3c^4} \gamma^2 \mathbf{a}_{\perp}^2 \boldsymbol{\beta}, \quad (1.11)$$

where $\mathbf{a}_{\perp} = (e/m_e)(\mathbf{E} + \boldsymbol{\beta} \times \mathbf{B})_{\perp}$ is the component of the Lorentz acceleration perpendicular to the particle direction, γ is the Lorentz factor, and $\boldsymbol{\beta} = \mathbf{v}/c$ is the particle velocity in units of c (see Yuan

et al., 2016). Equating the radiation drag force to the accelerating force from an electric field, $\mathbf{F}_{\text{acc}} = e\mathbf{E}$, with the same strength as the magnetic field, $E = B$, one can estimate for the synchrotron radiation reaction limit:

$$\gamma_{\text{rad}} = \sqrt{\frac{2 m_e c^2}{3 e B r_e}}, \quad (1.12)$$

with $r_e = e^2/m_e c$ the classical electron radius.

This limit plays an important role in the estimation of physical conditions for high-energy astrophysical phenomena, such as, for instance, the Crab Nebula. The synchrotron radiation reaction limit has consistently explained the high-energy cutoff in the synchrotron spectrum of the Crab Nebula, $\sim 160(E/B)$ MeV (e.g., de Jager et al., 1996). Later observations of gamma-ray flares, performed with *AGILE* and *Fermi* telescopes, revealed synchrotron emission above this limit, at photon energies up to 375 MeV (Buehler et al., 2012). By means of Particle-In-Cell simulations Cerutti et al. (2013, 2014), were able to demonstrate that acceleration of electrons beyond the radiation reaction limit is possible in relativistic reconnection layers, where there is a strong coherent electric field and weak magnetic field perpendicular to particle motion, $E > B_{\perp}$.

1.2 Blazars

Blazars are radio loud AGN in which one of the jets is directed towards the observer (Urry and Padovani, 1995). Among all AGN types, blazars stand out due to their extremely luminous emission that spans the whole electromagnetic spectrum, from radio to very high energies (\sim TeV), being the main object type in the γ -ray source catalogs (e.g., Acero et al., 2015). The broad-band spectral energy distributions (SED) of blazars are characterized by two broad components (see Figure 1.4), a low-energy one extending from radio to UV or soft X-rays, and a high-energy one extending up to the γ -rays. The main classification among them is based on the presence of broad emission lines in their optical spectra: BL Lac objects are blazars whose spectra show weak or no lines, and flat-spectrum radio quasars (FSRQ) are blazars that show strong lines and are systematically more luminous than BL Lacs.

Modeling of the blazar SEDs allows to constrain the particle composition of jets. All models describe the low-energy SED component as originating from synchrotron emission from a highly energized population of electrons (and positrons), which is in accordance with the high polarization observed in this electromagnetic range (e.g., Angel and Stockman, 1980; Perlman et al., 2006). There are two main branches of models that attempt to explain the observed high-energy SED component of blazars. The first, and most prominently studied, are the leptonic models. The high-energy SED component can be modeled with SSC in most BL Lacs (e.g., Potter and Cotter, 2012), this was also attempted in the case of some FSRQs (e.g., Maraschi et al., 1992), but achieving their high gamma-ray luminosities requires weak magnetic fields that make the model radiatively inefficient. Then, external photon fields have been proposed as seed photons for the inverse Compton scattering emission to explain the high-energy component of FSRQs, see Sikora et al. (1994); Błażejowski et al. (2000); Ghisellini and Tavecchio (2009).

The second branch of models to explain the high-energy SED component are the hadronic models that propose relativistic protons or ions, possibly together with leptons, to be the sources of blazar spectra, e.g., Sikora et al. (2009). The motivation for hadronic models is that protons can be accelerated in jets as well as electrons, providing a plausible explanation for the highest-energy cosmic rays

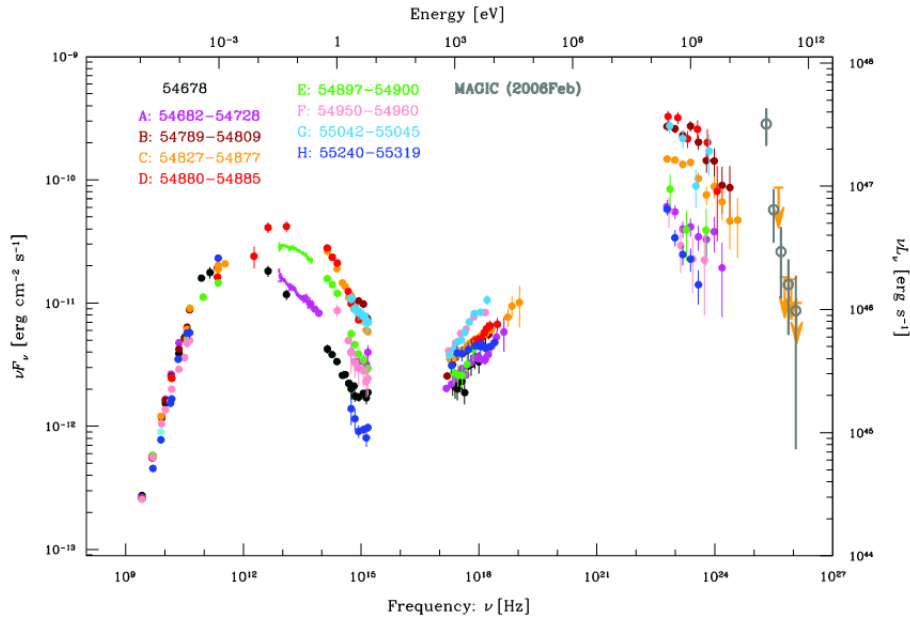


Figure 1.4: Broadband, ranging from radio to high-energy γ -rays, spectral energy distributions of the blazar 3C 279 obtained for several epochs, with time periods in MJD indicated in the legend. From Hayashida et al. (2012).

(Petropoulou et al., 2015). However, these models predict very low radiative efficiency which requires an extremely high accretion rate in order to provide the necessary jet power, see Zdziarski and Bottcher (2015).

Blazars also present highly variable emission on a wide range of time scales, ranging from decades (Ahnen et al., 2016) to minutes (Aharonian et al., 2007; Rani et al., 2017), see Fig.1.5. The shortest time scales observed are shorter than the light crossing time (\sim hours) of the SMBH gravitational radius, $r_g \equiv GM_{\text{SMBH}}/c^2$, which suggests that the emission comes from compact regions within the jet (Levinson, 2007). If the mechanism producing the high-energy component of the blazar SEDs is inverse Comptonization, then, high Lorentz factors of the emitting region are required, $\gamma \gtrsim 50$, in order to enhance the emission luminosity, by means of relativistic effects, to avoid higher photon densities which could trigger electron-positron production, which in turn would absorb gamma-ray photons (e.g., Begelman et al., 2008). These Lorentz factors are much larger than the bulk motions inferred from radio measurements of, $\gamma \sim 10$, which suggests an additional local bulk acceleration of the emitting regions.

Besides, the blazar SEDs can be well described as power laws, $P(\nu) \propto \nu^{-\alpha}$, with the indices, α within the range 1.3 to 1.7 (Madejski and Sikora, 2016). This is an indicator of emitting plasma with non-thermal particle energy distributions that require highly efficient particle acceleration mechanisms (Kirk et al., 1998; Ghisellini et al., 2017).

1.2.1 Non-thermal emission from other high-energy astrophysical phenomena

Like blazars, other high-energy astrophysical phenomena present broad spectra that extend as power laws, corresponding to emission from non-thermal particle energy distributions. Such phenomena include pulsar wind nebulae, PWN, (e.g., Buehler et al., 2012) and gamma-ray bursts, GRB (Piran, 2004). The radiation observed from PWN is most likely produced in highly magnetized regions. The emission

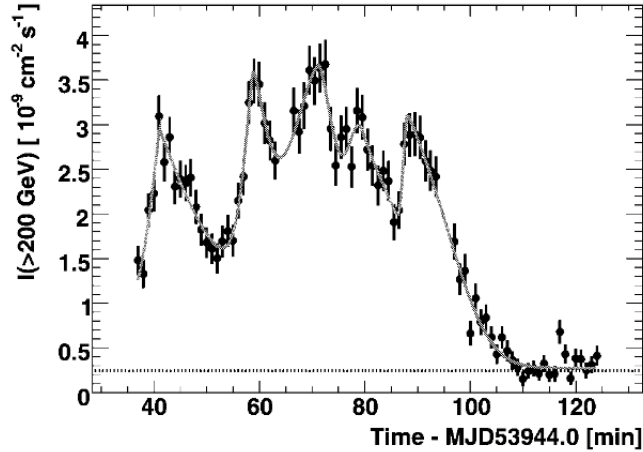


Figure 1.5: Light curve of very high energy (VHE) gamma-ray photon flux observed from PKS 2155-304 blazar with the H.E.S.S. array of Cerenkov telescopes in Namibia. We can see several flares on very short time-scales, \sim mins, which constrains the emission models for blazars. Image from [Aharonian et al. \(2007\)](#).

from GRB might also originate from highly magnetized regions. These regions are characterized by a magnetic energy density of the order or greater than the internal energy density (including the rest energy density). This can be expressed using the magnetization parameter $\sigma = B^2/(4\pi n\Theta m_e c^2) > 1$, where n is the number density, $\Theta = k_B T/m_e c^2$ is the dimensionless temperature, and k_B is the Boltzmann constant.

In order to transfer the magnetic energy to the particles, efficient magnetic dissipation mechanisms are required. Due to the low density of these particle accelerating regions, collisions between particles are uncommon in comparison with their interactions with electromagnetic fields, hence, particles are unable to thermalize.

1.3 Particle acceleration mechanisms

Non-thermal emission signatures are present in highly energetic astrophysical phenomena, thought to be produced by highly energetic particle populations. Such energetic populations of particles require efficient non-thermal particle acceleration mechanisms. Historically, several mechanisms have been proposed and tested numerically: diffusive shock acceleration (e.g., [Niemić and Ostrowski, 2004](#); [Spitkovsky, 2005](#); [Sironi and Spitkovsky, 2011](#)), scattering by magnetic turbulence (e.g., [Petrosian, 2012](#); [Comisso and Sironi, 2018](#)), acceleration in velocity shear layers (e.g., [Stawarz and Ostrowski, 2002](#)), or magnetic reconnection (e.g., [Sironi and Spitkovsky, 2014](#); [Werner et al., 2016](#)).

1.3.1 Fermi mechanism

Aiming at explaining the origin of cosmic rays, [Fermi \(1949\)](#) proposed a mechanism by which charged relativistic particles would gain energy from repeated interactions with magnetic clouds, acting as magnetic mirrors, with random motions. Collisions between a particle and a magnetic cloud traveling in opposed directions, head-on collision, results in a net energy gain for the charged relativistic particle,

while a collision of a particle and a target cloud traveling in the same direction, tail-on collision, results in an energy loss for the particle. It turns out that, on average, the head-on collisions are more probable, so the average particle energy gain per collision is proportional to $\langle(\Delta E)/E\rangle \propto (V/c)^2$, where V is the typical velocity of magnetic clouds. Hence, this mechanism is known as the *second-order Fermi* acceleration and provides a plausible mechanism for producing non-thermal particle energy distribution of the form, $N(E) \propto E^{-p}$ with $p = 1 + (\tau_{\text{col}}c^2)/(2V^2\tau_{\text{esc}})$, where τ_{col} is the timescale between subsequent collisions and τ_{esc} is the timescale for particles escape from acceleration region (Blandford and Eichler, 1987; Courvoisier, 2013).

A Fermi mechanism can also be realized in a collisionless shock, where the mean free path for particle collisions is longer than the shock width. If at both sides of the shock, upstream and downstream, particles interact with electromagnetic fluctuations, they will diffuse in momentum space. This means that a particle, with sufficient initial energy to enter the game¹, can cross the shock repeatedly. On average, the particle energy gain when crossing the shock is expressed as $\langle\Delta p\rangle/p = (2\Delta U)/(3v)$, where p is the particle momentum, v its velocity module, and ΔU is the difference in flow velocity between the upstream and the downstream (Drury, 1983). This mechanism is named as *first-order Fermi* or as *diffusive shock acceleration* (DSA). However, in the case of relativistic shocks, the maximum particle energy is limited even by weak magnetizations (Sironi et al., 2013).

1.3.2 Magnetized turbulence

Turbulence within magnetized plasmas is expected to be a generic by-product of different instabilities present in astrophysical sources of high-energy emission, which may provide particle acceleration. For instance, Ferrari et al. (1979) argued that Kelvin-Helmholtz instabilities at the boundary layer of the jet could accelerate electrons to high energies (Sironi et al., 2021). Stochastic interactions of particles with turbulent fluctuations within magnetized plasmas are capable to energize particles via a process akin to the second-order Fermi mechanism, i.e., via interaction with magnetic mirrors. This process can be modeled with a Fokker-Planck approach:

$$\frac{d\langle\gamma\rangle}{dt} = \frac{1}{\gamma^2} \frac{\partial}{\partial\gamma} \left[\gamma^2 D_p \right], \quad (1.13)$$

where D_p is the diffusion coefficient in momentum space (see Petrosian, 2012). Comisso and Sironi (2018) showed that power-law particle energy spectra are generated by turbulence in relativistically magnetized plasmas where particles were first efficiently accelerated by relativistic magnetic reconnection (RMR), i.e., magnetic reconnection in the $\sigma > 1$ regime, and later further accelerated by stochastic interactions with turbulent fluctuations.

1.3.3 Magnetic Reconnection

Magnetic reconnection is a dissipation mechanism that changes the topology of magnetic field lines and transforms the magnetic energy into thermal heating of the plasma, bulk plasma acceleration, and non-thermal particle acceleration, see Zweibel and Yamada (2009) for a review.

¹The need for sufficient energy in order to cross the shock several times is known as the injection problem, which means that an additional pre-acceleration mechanism is necessary.

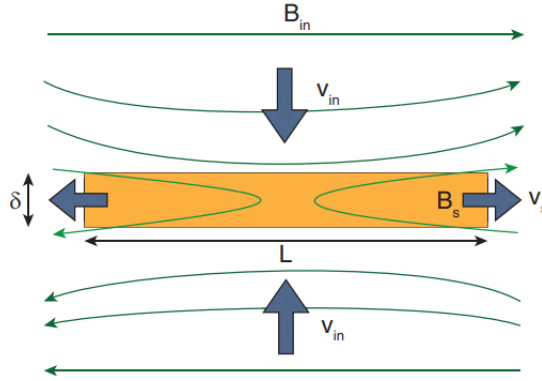


Figure 1.6: Illustration of the Sweet-Parker model of magnetic reconnection. The yellow area represents the current layer (magnetic diffusion region) of microscopic width δ and macroscopic length $L \gg \delta$. Plasma inflows to the layer with characteristic velocity v_{in} , the reconnection rate, and outflows with a much larger velocity v_s . From Takamoto (2013).

Magnetic reconnection is able to accelerate particles by means of the electric field that appears in a current layer separating locally reversed magnetic fields. The plasma outside the current layer is dragged towards it with characteristic inflow velocity u_{rec} , which induces a motional electric field $\mathbf{E} = \mathbf{B} \times \mathbf{u}_{rec}/c$. This velocity u_{rec} is also known as the reconnection rate, it is a key parameter measuring the efficiency of magnetic reconnection.

There are two classical models of magnetic reconnection: the Sweet-Parker model and the Petschek model. The Sweet-Parker model (Parker, 1957; Sweet, 1958) is the simplest one in which magnetic field lines are antiparallel and uniform magnetic diffusivity is assumed, see Figure 1.6. Assuming that the plasma inflows towards the reconnection region of microphysical thickness δ and macroscopic length $L \gg \delta$, conservation of mass and magnetic flux allows to relate the reconnection rate to the outflow velocity u_{out} , which is of the order of the background Alfvén velocity u_A : $u_{rec} \sim (\delta/L)u_A$. However, since the δ/L ratio might be expected to be extremely small, the implied reconnection rates would be extremely slow compared with the values required to explain, for instance, the solar flares.

Higher reconnection rates are required in order to induce electric fields that could accelerate particles to energies needed to explain observations. Thus, a second configuration, named Petschek reconnection (Petschek, 1964) was proposed assuming that the magnetic diffusion region is of intermediate length, $L_{diff} \sim 10\delta \ll L$, which allows higher reconnection rates $u_{rec} \sim (\delta/L_{diff})u_A \sim 0.1u_A$ (Liu et al., 2022).

Both the Sweet-Parker and Petschek models have been extended to the case of relativistically magnetized plasma (Lyubarsky, 2005) expected in relativistic jets and pulsars. It has been shown analytically that the outflows can be mildly relativistic in the Sweet-Parker model and ultrarelativistic in the Petschek model.

Since approximations are made in order to derive the analytical models of reconnection, the associated particle acceleration can be studied self-consistently by means of Particle-In-Cell (PIC) simulations (see Section 1.4 for more details). Kinetic simulations allow to calculate from the first principles particle energy distributions resulting from the RMR. The RMR has been extensively studied, e.g., Cerutti et al. (2013); Werner et al. (2016); Sironi et al. (2016). In all of the previous studies, the magnetic reconnection proceeds from the tearing instability that forms a series of magnetic X-points (diffusion

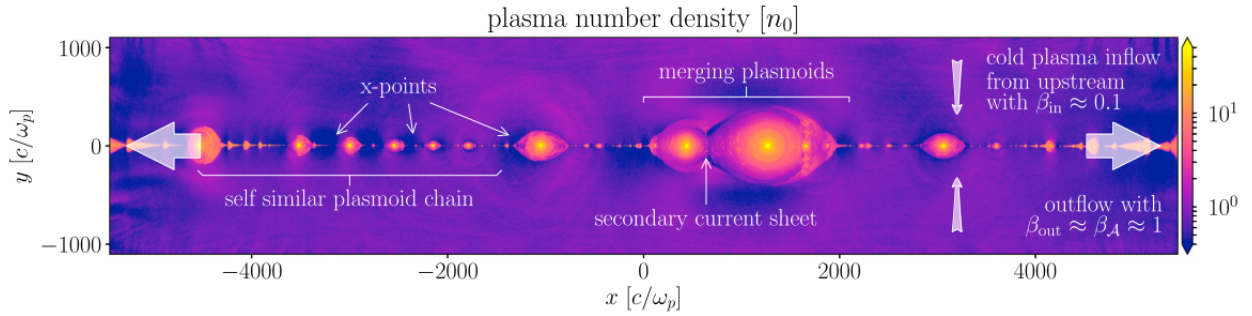


Figure 1.7: Snapshot of a 2D relativistic magnetic reconnection simulation from [Hakobyan et al. \(2019\)](#). Thick arrows indicate the direction of the inflow background plasma and the ultrarelativistic plasma outflow, $\beta_{\text{out}} \approx 1$. The color indicates plasma density. The highest density is achieved in the plasmoid cores.

regions). As long as there is an inflow of background plasma, the current sheet is continuously breaking into shorter sheets separated by X-points ([Loureiro et al., 2007](#)). Plasmoids, also known as magnetic islands, are regions of closed magnetic loops trapping energetic particles. Plasmoids undergo hierarchical mergers along the reconnection layer, resulting in a broad range of their sizes, see Figure 1.7.

In the relativistically magnetized regime, magnetic reconnection has been proven to provide hard spectra with power-law indices $p \lesssim 2$ in 2D simulations with electron-positron pair plasma ([Sironi and Spitkovsky, 2014](#); [Guo et al., 2014](#); [Werner et al., 2016](#)), with electron-ion plasma ([Guo et al., 2016](#); [Werner et al., 2018](#)), and with electron-positron-ion plasma ([Petropoulou et al., 2019](#)). Similar particle energy distributions were also found in 3D simulations, despite showing additional effects that partially disrupt the reconnection layer, e.g., [Sironi and Spitkovsky \(2014\)](#); [Zhang et al. \(2021\)](#). In magnetic reconnection simulations, both in relativistic and non-relativistic regimes, particle acceleration has been described as effectively a first-order Fermi mechanism ([Drake et al., 2006](#); [Guo et al., 2014](#)).

The observed gamma-ray flares of blazars show variability on very short timescales (of the order of few minutes), even shorter than the light-crossing time of their supermassive black holes. Studies of the RMR have shown that plasmoids and relativistic plasma outflows between them, termed minijets, are continuously formed. These minijets were proposed as sources of fast blazar flares ([Giannios et al., 2009](#); [Nalewajko et al., 2011](#)). Motivated by studies in which the plasmoids are shown to reach macroscopic scales ([Loureiro et al., 2012](#)), [Giannios \(2013\)](#) proposed a model where the large plasmoids power the emission from fast blazar flares. The RMR is a dynamical process where new plasmoids are continuously being generated and ejected from the reconnection layer, hence, in order to capture the plasmoid formation and characteristics during their evolution, simulations with open boundaries were needed. This allows the outflow to be unimpeded, avoiding artificial effects that restrict plasmoid generation. By means of kinetic non-radiative simulations [Sironi et al. \(2016\)](#) found that plasmoids are formed with different sizes with an anti-correlation between plasmoid size and bulk velocity. Small plasmoids were found to contain anisotropic particle distributions and larger plasmoids have isotropic particle distributions (in the plasmoid comoving frame). Large plasmoids remain for longer in the current layer growing by collecting plasma from reconnection outflows and merging with smaller plasmoids, reaching widths of $\sim 0.2 L$, where L is the current layer length.

These statistical properties of plasmoids and their particle energy distributions, were used in the

study of non-thermal radiative signatures (calculated by post-processing simulation results without accounting for radiative cooling) in [Petropoulou et al. \(2016\)](#); [Christie et al. \(2019\)](#), showing that a plasmoid chain generated during a reconnection event could reproduce the temporal and spectral properties of blazar emissions. In particular, flares of duration \sim hours-days could be produced by the large plasmoids that contain highly energetic particles ([Petropoulou et al., 2016](#)). Besides, the observed variability was found to be highly dependent upon the orientation of the relativistic outflow from the reconnection region with respect to the jet direction. As expected from relativistic effects, the fully aligned configuration, i.e., reconnection outflows parallel to the jet direction, produces the shortest variability timescales ([Christie et al., 2019](#)).

1.3.4 Instabilities of magnetized jets

Jets are believed to be launched with most of their energy in the form of Poynting flux, i.e., as magnetic energy. It is still under active debate how and where this energy transfers to the plasma. Relativistic magnetic reconnection could be one of the main dissipation mechanisms, but it has a main requirement, to have local inversions of the magnetic field lines. Models have been proposed where magnetic reversals are advected through the jet base from the accretion disk ([Spruit et al., 2001](#); [Nalewajko et al., 2011](#); [Giannios and Uzdensky, 2019](#)). However, it is more often assumed that the magnetic reconnection configuration is achieved by jet instabilities ([Giannios and Spruit, 2006](#); [Begelman, 1998](#)), that eventually may disrupt the jet ([Mizuno et al., 2011](#); [Tchekhovskoy and Bromberg, 2016](#)). With the aim of investigating numerically these instabilities, jets are approximated as being cylindrical, since the instabilities depend mainly on the radial profile of the jet ([Mizuno et al., 2011, 2012](#)).

Analytical descriptions of the instabilities of non-relativistic cylindrical plasma columns are well-known (e.g., [Bateman, 1978](#)). They derive from an ideal MHD² static equilibrium configuration of the axisymmetric magnetized plasma column. The static condition requires that the bulk velocity of the plasma is zero, $\mathbf{u} = 0$, and that there are no changes in time, so, $\partial/\partial t = 0$. Applying this to the momentum (Euler) equation

$$\rho \left(\frac{\partial \mathbf{u}}{\partial t} + \mathbf{u} \cdot \nabla \mathbf{u} \right) = -\nabla P + \frac{\mathbf{j} \times \mathbf{B}}{4\pi} = 0 \quad (1.14)$$

(where \mathbf{u} is the flow velocity, ρ is the mass density, and P is the gas pressure), yields the force balance equation. Using the Ampère's law, $\mathbf{j} = (c/4\pi)\nabla \times \mathbf{B}$, and assuming axial symmetry $\partial/\partial\phi = 0$ and translational symmetry $\partial/\partial z = 0$ (which ensures that all profiles depend only on the radius), we can obtain the r-component of the force balance equation expressed in cylindrical coordinates:

$$\frac{B_\phi}{4\pi r} \frac{d}{dr}(rB_\phi) + \frac{1}{8\pi} \frac{dB_z^2}{dr} + \frac{dP}{dr} = 0, \quad (1.15)$$

where B_ϕ and B_z are the ϕ and z-component of the magnetic field. From Eq. 1.15, two force balance configurations are traditionally distinguished, Z-pinch and screw-pinch.

²The Ohm's law that expresses the electric field in the frame of the fluid element moving at velocity \mathbf{u} : $\mathbf{E}' = \mathbf{E} + (\mathbf{u} \times \mathbf{B})/c = \rho \mathbf{j}' \simeq \rho \mathbf{j}$ where \mathbf{E} is the electric field in the laboratory frame and ρ is the resistivity. When resistivity is negligible, MHD equations simplify to the case of ideal MHD. Resistivity can be neglected in most of the volumes of astrophysical plasmas of interest here.

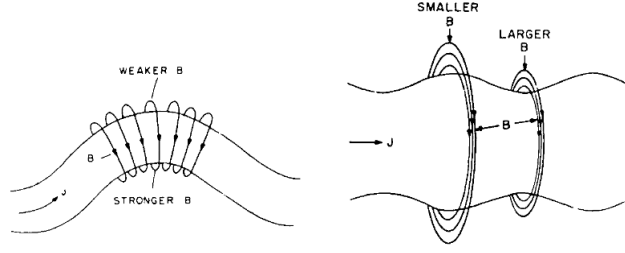


Figure 1.8: Schematic representation of the kink, $m=1$ (left) and pinch, $m=0$ (right) instabilities of an axisymmetric plasma column. Regions where the plasma gets compressed drag with them the magnetic field lines that result in an increase of magnetic pressure that triggers the development of the instability. Figure from [Liberman et al. \(1999\)](#).

Z-pinch

In the Z-pinch configuration the axial component of the magnetic field, B_z , is neglected, and the pressure and tension exerted by the toroidal magnetic field, B_ϕ , is compensated by the thermal gas pressure gradient, i.e., a gas-pressure-balanced configuration. The instabilities arising from this equilibrium configuration are known as pressure-driven instabilities (PDI). The two most unstable modes, in this case, are the pinch and kink instability modes, with $m = 0$ and $m = 1$ (see Fig. 1.8), respectively, where m is the wave number of the Fourier transform of the perturbation in the azimuthal direction,

$$\xi(r, \phi, z) = \sum_m \sum_k \xi(r) \exp(im\phi + ikz), \quad (1.16)$$

with k the wave number in the axial direction ([Schekochihin, 2020](#)). Based on the energy principle (see [Bernstein et al., 1958](#); [Kulsrud, 2005](#)), we know that for an axisymmetric perturbations, $\partial/\partial\phi = 0$, i.e., for the $m = 0$ pinch mode, the Z-pinch configuration is unstable for pressure profiles that satisfy

$$-r \frac{d \ln P(r)}{dr} > \frac{2\Gamma}{1 + \Gamma\beta_{\text{pl}}/2}, \quad (1.17)$$

where $P(r)$ is the radial pressure profile, Γ is the adiabatic index ($\Gamma = 4/3$ in the relativistic regime), and $\beta_{\text{pl}} = (8\pi P)/(B^2)$ is the ratio of gas to magnetic pressures, which for Z-pinch configuration is $\beta_{\text{pl}} \sim 1$.

For non-axisymmetric perturbations with $m > 0$, the energy principle results in the following instability criterion

$$-r \frac{d \ln P(r)}{dr} > \frac{m^2}{\beta_{\text{pl}}}. \quad (1.18)$$

We can see that for non-axisymmetric modes, the most unstable ones are the modes with the smallest azimuthal wavenumber m , i.e., $m = 1$ kink mode. Hence, the Z-pinch configuration is unstable to pinch and kink modes for sufficiently steep radial gas pressure profiles (steeper than $1/r$ for the kink, $m = 1$, mode).

Screw-pinch

In the screw-pinch case, all components of Eq. 1.15 are non-negligible, although often a force-free equilibrium is assumed, i.e., $\mathbf{j} \times \mathbf{B} = 0$ (hence $\nabla P = 0$), which means that toroidal magnetic field

must be balanced by the poloidal component. Instabilities arising from this configuration are called current-driven instabilities (CDI) and are dominated by the kink modes (Appl et al., 2000). Screw-pinch configuration is stable when the Kruskal-Shafranov criterion is fulfilled

$$Q_0 \gtrsim \frac{L}{2\pi}, \quad (1.19)$$

where L is the length of the electric current column, $Q_0 = Q(r = 0)$ is the magnetic pitch value at the axis, where magnetic pitch is defined as $Q(r) = rB_z(r)/B_\phi(r)$ (Kruskal and Tuck, 1958; Bromberg et al., 2019). This condition means that the equilibrium approaches instability as the toroidal magnetic field increases, i.e., the magnetic field lines get more tightly wrapped (Bateman, 1978).

Previous PIC studies

In order to study the development of the instabilities together with the evolution of the particle energy distribution, kinetic simulations are needed. Only recently, PIC simulations (see Section 1.4) were performed in the relativistic regime for either Z-pinch or screw-pinch configurations.

Alves et al. (2018) investigated a 3D static cylindrical jet composed of pair plasma (electrons and positrons) with strong toroidal magnetic field supported by gas pressure and weak uniform poloidal field. During the nonlinear development of the instabilities, they found that a large-scale induced coherent electric field appears in the axial direction. This electric field was found to be able to accelerate electrons and produce a power-law tail in the particle energy spectrum, $dN/d\epsilon \propto \epsilon^{-p}$ with index $p = 2.75$. This means that a new mechanism of efficient particle acceleration was found. The mechanism proceeds as follows: first, the MHD instabilities are triggered by the thermal fluctuation of the plasma; second, as the instability develops, the transverse motions of the plasma induce an electric field, $\mathbf{E} = -\mathbf{v} \times \mathbf{B} \simeq E_z \hat{\mathbf{z}}$; third, during the nonlinear development of the instabilities, regions with same electric field polarity align and allow charged particles to move along the jet's spine while being energized, see Figure 1.9. Alves et al. (2018) argued that a particle energy limit, $\epsilon_{\text{conf}} \equiv eB_0R_c$ is set due to confinement of the particles within the jet core of radius R_c and typical field strength B_0 (this is basically the Hillas criterion that tells that the particle acceleration is finished when the Larmor radius of the particle, $\rho_0 = \gamma mc^2/(qB)$, becomes comparable to the jet core radius, R_c). Particles were found to be accelerated mostly by ideal electric fields, $\mathbf{E} \perp \mathbf{B}$. Alves et al. (2018) also found non-ideal electric fields, $\mathbf{E} \parallel \mathbf{B}$, to have little contribution to particle acceleration.

Davelaar et al. (2020) investigated the other main cylindrical magnetic jet configuration, i.e., the force-free screw-pinch configuration, where the pressure balance is provided only by the toroidal and poloidal magnetic fields. They also performed 3D PIC simulations in the co-moving frame of the jet, studying static, cylindrical pair plasma columns. Arguing that relativistic jets of AGN are thought to be launched and accelerated with highly magnetized cold plasma as long as no magnetic dissipation mechanism acts, they set up simulations with cold pair plasma and high magnetization, $\sigma \geq 10$. They found formation of current sheets at the outer fronts of the developing instability, including regions of non-ideal electric field, $\mathbf{E} \parallel \mathbf{B}$. They associated the non-ideal electric field acceleration to magnetic reconnection in the strong guide field regime, which is less efficient in accelerating particles (Werner and Uzdensky, 2017). They also reported additional minor acceleration by weak turbulence induced in the later stages of the instability. They found steep power-law energy distributions, $p \sim 3-5$, hence particle acceleration in this case is less efficient compared with the results of Alves et al. (2018).

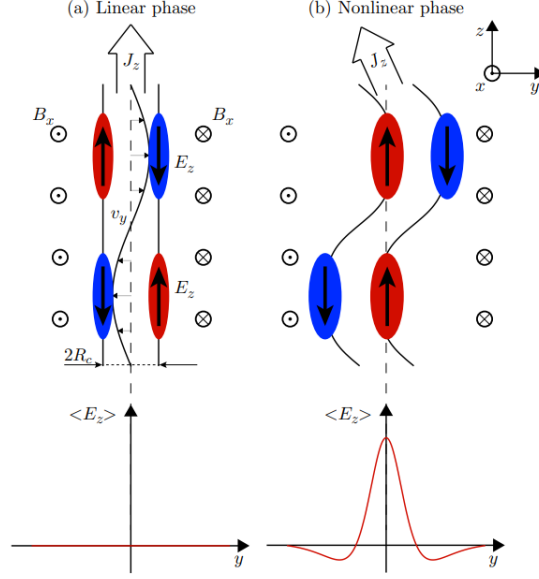


Figure 1.9: Illustration of the alignment of the regions with the same electric field polarity during the nonlinear phase of the instability growth. The electric field is induced by the plasma motions perpendicular to the local magnetic field, $\mathbf{E} = -\mathbf{v} \times \mathbf{B}$. Illustration from [Alves et al. \(2018\)](#).

1.4 Particle-In-Cell kinetic simulations

Jets from relativistic astrophysical sources are expected to have low densities due to their nonthermal signatures that denote collisionless plasmas. The collisionless approach assumes that the average distance that particles travel between collisions, i.e., the mean free path λ_{mfp} is sufficiently large for Coulomb collisions to be unimportant, namely, $\lambda_{\text{mfp}} \gg \lambda_{\text{D}}$, where λ_{D} is the Debye length that for thermalized plasma would be defined as

$$\lambda_{\text{D}} = \left(\frac{4\pi n e^2}{k_{\text{B}} T} \right)^{-1/2}, \quad (1.20)$$

where n is the mean number density of the plasma, T is the plasma temperature, k_{B} is the Boltzmann constant, and e is the electric charge of the electron. The Debye sphere with radius λ_{D} shields the electric field when a sufficient number of particles are contained within, i.e., $\lambda_{\text{D}} \gg \Delta r$ where $\Delta r \sim n^{1/3}$ is the typical separation between particles. If the kinetic energy is much higher than the electrostatic potential energy, $k_{\text{B}} T \gg U \sim e^2/(\Delta r) \sim e^2 n^{1/3}$, meaning that $\Delta r \gg d$, with $d \sim e^2/(k_{\text{B}} T)$ the Coulomb length, we have that

$$\lambda_{\text{mfp}} \sim 1/(n\sigma) \sim (\Delta r)^3/d^2 \sim (\Delta r/d)^2 \Delta r \sim (\Delta r/d)^{3/2} \lambda_{\text{D}} \gg \lambda_{\text{D}} \quad (1.21)$$

(where $\sigma \sim d^2$ is the cross-section for Coulomb collisions) and

$$\lambda_{\text{D}} \sim (nd)^{-1/2} \sim (\Delta r)^{3/2}/d^{1/2} \sim (\Delta r/d)^{1/2} \Delta r \gg \Delta r, \quad (1.22)$$

i.e., the relations $\lambda_{\text{mfp}} \gg \lambda_{\text{D}} \gg \Delta r \gg d$ are satisfied. This tells us that particles travel long distances without experiencing interactions between each other and only macroscopic fields are altering their

trajectories (Schekochihin, 2020). The kinetic approach of PIC simulations is to calculate the particles-fields interactions and the evolution of the particle energy distributions.

The *Vlasov-Maxwell* equation describes the time evolution for the distribution function f of an ensemble of charged articles of the same species:

$$\frac{\partial f}{\partial t} + \mathbf{v} \cdot \nabla f + \frac{q}{m} \left(\mathbf{E} + \frac{\mathbf{v} \times \mathbf{B}}{c} \right) \cdot \frac{\partial f}{\partial \mathbf{v}} = 0 \quad (1.23)$$

where $\nabla = \partial/\partial \mathbf{r}$ is the spatial gradient, q the particle electric charge, and m the particle mass. This equation assumes that particles interact only with the fields through the Lorentz force. In order to account for collisions between particles, additional terms would need to be included.

Kinetic simulations discretize the distribution function and compute the dynamics of an ensemble of macroparticles

$$f(\mathbf{r}, \mathbf{p}, t) \approx \sum_{k=1}^{N_\alpha} w_k \delta(\mathbf{r} - \mathbf{r}_k(t)) \delta(\mathbf{p} - \mathbf{p}_k(t)) \quad (1.24)$$

where w_k is the weight of the k -particle and δ is the Dirac delta function.

Each macroparticle followed within the computational domain represents a set of identical particles (could be electrons, positrons, or ions) in order to reduce the computational cost of the simulations. These macroparticles are within a computational domain that is organized as a grid. Particle-In-Cell methods compute both the motion of the charged particles propagating under the Lorentz force and the evolution of the electric and magnetic fields from the integration of the Maxwell equations. Due to the flexibility of this method, additional physical effects can be added, such as synchrotron and inverse Compton radiation drag forces.

In order to advance particles and electromagnetic fields, the leapfrog integration method is used (Pritchett, 2003). This method is an explicit (field and particle values calculated from values at previous time steps) time-centered, finite-difference scheme. In the leapfrog method, particle positions and momenta, as well as electromagnetic field components, are updated at alternating times, with a difference of half time step (see Fig. 1.10).

This second-order integration method (truncation error is proportional to $(\Delta t)^2$) provides sufficient accuracy for oscillatory motions, which is required for the dynamics of charged particles in magnetic fields. Furthermore, as an explicit time integration method, it is required to satisfy the Courant–Friedrichs–Lewy (CFL) condition (Courant et al., 1928). The CFL condition establishes that the time step of the explicit finite-difference scheme, Δt , must be shorter than the time required by the fastest traveling wave to cross a single grid cell. Since we are performing relativistically magnetized simulations, MHD waves have speeds close to c (for instance, in the case of Alfvén waves, $v_a/c = \sqrt{\sigma/(\sigma + 1)}$, see Sironi et al. (2016)). Hence, the CFL condition is expressed as:

$$c\Delta t \leq c\Delta t_{\text{CFL}} = \Delta x / \sqrt{N_D}, \quad (1.25)$$

where Δx is the grid spacing, which is uniform and equal along x, y, z axes; and N_D is the number of dimensions (Cerutti et al., 2013).

The electric and magnetic fields are staggered on a grid mesh following the prescription of Yee (1966) (see Fig. 1.11) which allows to preserve the condition $\nabla \cdot \mathbf{B} = 0$ with numerical precision.

The procedure for the n -th timestep of a PIC simulation is the following:

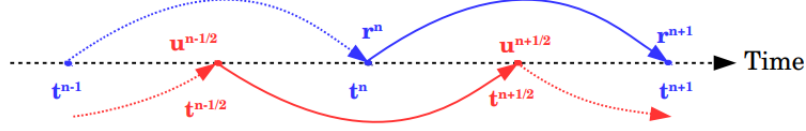


Figure 1.10: Schematic illustration of the leapfrog integration method. From lecture notes of Dr. Benoît Cerutti given at the Astrosim summer school held in ENS Lyon, 2017, France.

1. Determine the fields \mathbf{E}^n , \mathbf{B}^n and particle positions \mathbf{r}^n at the time t^n , and particle momenta $\mathbf{u}^{n-1/2}$ at the time $t^{n-1/2}$. Since the fields are determined at the staggered mesh nodes, their values at the particle positions are calculated using bilinear (trilinear) interpolation in the 2D (3D) simulations.
2. Advance the momentum and position for each macroparticle, following Newton's equations, $d\mathbf{u}/dt = q/(mc)(\mathbf{E} + \mathbf{u} \times \mathbf{B}/\gamma)$ and $d\mathbf{r}/dt = c\mathbf{u}/\gamma$, with $\mathbf{u} = \gamma\boldsymbol{\beta} = \gamma\mathbf{v}/c$ the dimensionless momentum (four-velocity) and γ the Lorentz factor. With that, the particle momentum equation is discretized in time:

$$\frac{\mathbf{u}^{n+1/2} - \mathbf{u}^{n-1/2}}{\Delta t} = \frac{q\mathbf{E}^n}{mc} + \frac{q}{mc} \left(\frac{\mathbf{u}^{n+1/2} + \mathbf{u}^{n-1/2}}{2\gamma^n} \right) \times \mathbf{B}^{n-1/2}. \quad (1.26)$$

As one can see, the value of the momentum at the $n + 1/2$ time step also appears on the right hand side. By means of the Boris push method, the particle momentum is computed explicitly (see Boris, 1970; Birdsall and Langdon, 1991). After defining $\mathbf{u}^- = \mathbf{u}^{n-1/2} + (q\mathbf{E}^n \Delta t)/(2mc)$ and $\mathbf{u}^+ = \mathbf{u}^{n+1/2} - (q\mathbf{E}^n \Delta t)/(2mc)$, Eq. 1.26 gives:

$$\mathbf{u}^+ = \mathbf{u}^- + \mathbf{u}^- \times \mathbf{s} + (\mathbf{u}^- \times \mathbf{w}) \times \mathbf{s}, \quad (1.27)$$

where $\mathbf{w} = (q\mathbf{B}^{n-1/2} \Delta t)/(2mc\gamma^n)$ and $\mathbf{s} = (2\mathbf{w})/(1 + w^2)$. The parameter \mathbf{u}^+ is then used to calculate $\mathbf{u}^{n+1/2}$. The particle positions are advanced simply as

$$\mathbf{r}^{n+1} = \mathbf{r}^n + \left(\frac{c\Delta t}{\gamma^{n+1/2}} \right) \mathbf{u}^{n+1/2}. \quad (1.28)$$

3. Charge density ρ and current density \mathbf{J} are deposited at the appropriate positions in the Yee lattice. The contribution of macroparticle k located at \mathbf{r}_k to the charge density at the node i located at \mathbf{r}_i is $\rho_{i,k} = q_k w_k S(\mathbf{r}_i - \mathbf{r}_k)$, where q_k is the macroparticle charge, w_k is the macroparticle weight, and S is the *shape function* that describes the spatial distribution of a charge cloud associated with each macroparticle. Hence, the charge associated with a node is given by the sum of the contribution of all the macroparticles (N) whose associated charge cloud intersects the cell corresponding to the node:

$$\rho_i = \sum_{k=1}^N q_k w_k S(\mathbf{r}_i - \mathbf{r}_k(t)). \quad (1.29)$$

For our 2D simulation the shape function corresponds to a square cloud of size (dx, dy) centered at the particle position, while for our 3D simulations the shape function corresponds to a cube of size (dx, dy, dz) centered at the particle position. The charge from a particle deposited at every cell in 2D (3D) is proportional to the area (volume) of the shape function that is contained within that cell.

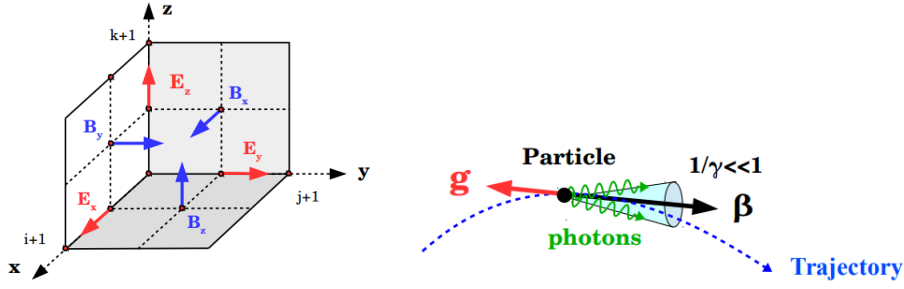


Figure 1.11: *Left*: 3D Yee mesh, magnetic and electric fields are computed at staggered positions (Yee, 1966). *Right*: Schema of the radiation reaction force, presented in red, due to acceleration of a relativistic charged particle that is traveling at speed β . From Benoît Cerutti’s lecture notes on PIC simulations.

For the current density deposition, we use the shape functions introduced by Esirkepov (2001), which allow to conserve charge to numerical precision³.

4. Solve Maxwell’s equations in order to update the fields from the previous values. The electric and magnetic fields are advanced in time using the Maxwell’s equations involving time derivatives $\partial \mathbf{E} / \partial t = c \nabla \times \mathbf{B} - 4\pi \mathbf{J}$ and $\partial \mathbf{B} / \partial t = -c \nabla \times \mathbf{E}$. There are again two leapfrogged steps, magnetic field is advanced from $t^{n-1/2}$ to $t^{n+1/2}$ using electric field at t^n , and electric field is advanced from t^n to t^{n+1} using magnetic field and current density at $t^{n+1/2}$,

$$\frac{\mathbf{B}^{n+1/2} - \mathbf{B}^{n-1/2}}{\Delta t} = -c \nabla \times \mathbf{E}^n \quad (1.30)$$

and

$$\frac{\mathbf{E}^{n+1} - \mathbf{E}^n}{\Delta t} = c \left(\nabla \times \mathbf{B}^{n+1/2} \right) - 4\pi \mathbf{J}^{n+1/2}. \quad (1.31)$$

Each cycle of the PIC algorithm advances the positions and momenta of all particles, as well as the electric and magnetic fields, from $\{\mathbf{r}^n, \mathbf{u}^{n-1/2}, \mathbf{E}^n, \mathbf{B}^{n-1/2}\}$ to $\{\mathbf{r}^{n+1}, \mathbf{u}^{n+1/2}, \mathbf{E}^{n+1}, \mathbf{B}^{n+1/2}\}$.

1.4.1 ZELTRON code

For the presented research, we have performed PIC simulations with customized versions of the ZELTRON code (Cerutti and Werner, 2013). ZELTRON is written in Fortran and fully parallelized via implementing Message Passing Interface (MPI). This allows to perform extended simulations on large computing clusters with parallel architecture, such as *Prometheus* located at Cyfronet AGH, Poland (access provided by the PLGrid). By means of the decomposition of the computational domain, the workload can be distributed among multiple computing units (≈ 2000 CPUs). The main novelty of ZELTRON, compared with most other PIC codes, is the implementation of the radiation drag force \mathbf{g} (see the right schema of Fig. 1.11) in the particle equation of motion:

$$\frac{d\mathbf{u}}{dt} = \frac{q}{mc} \left(\mathbf{E} + \frac{\mathbf{u} \times \mathbf{B}}{\gamma} \right) + \mathbf{g} \quad (1.32)$$

³In earlier versions of Zeltron, a simplified charge deposition scheme did not guarantee satisfying the charge conservation equation, resulting in nonphysical electric fields that did not satisfy the Gauss equation $\nabla \cdot \mathbf{E} = 4\pi\rho$. The electric field was corrected by solving Poisson’s equation every time step.

where, in the ultra-relativistic regime, $\gamma \gg 1$, the drag force can be expressed as:

$$\mathbf{g} = -\frac{2}{3}r_e^2\gamma \left[\left(\mathbf{E} + \frac{\mathbf{u} \times \mathbf{B}}{\gamma} \right)^2 - \left(\frac{\mathbf{u} \cdot \mathbf{E}}{\gamma} \right)^2 \right] \mathbf{u} \quad (1.33)$$

where $r_e = e^2/mc^2$ is the classical electron radius and $\mathbf{u} = \gamma\boldsymbol{\beta}$ is the dimensionless momentum of a particle (see Cerutti et al., 2013).

The radiative cooling rate of a charged particle is given by $d\mathbf{u}/dt = -P_{\text{emi}}\mathbf{u}/(\gamma mc^2)$, with P_{emi} the total emitted power (Cerutti et al., 2013). Noting that for $\gamma \gg 1$ we have $u \simeq \gamma$, then the radiative cooling rate for synchrotron becomes

$$\frac{d\gamma}{dt} = \frac{\mathbf{u}}{\gamma} \cdot \frac{d\mathbf{u}}{dt} \simeq -\frac{P_{\text{syn}}}{mc^2}. \quad (1.34)$$

In our first project, one of our aims was to contain the emission of plasmoids within the simulation box. For that, we set a configuration such that the cooling length of relativistic electrons was smaller than the size of the simulation box. Using eq. 1.4, the cooling length for synchrotron emitting particle can be estimated as

$$l_{\text{cool}} = c\tau_{\text{cool}} = \frac{\langle \gamma \rangle}{\langle |d\gamma/cdt| \rangle} \simeq \frac{\langle \gamma \rangle}{\langle \gamma^2 \rangle} \frac{3mc^2}{4\sigma_T U_B}. \quad (1.35)$$

All of our simulations are initiated with particle energies following the Maxwell-Jüttner distribution, which has the form

$$f(\gamma) = \frac{\gamma^2 \beta}{\Theta K_2(1/\Theta)} \exp\left(-\frac{\gamma}{\Theta}\right), \quad (1.36)$$

where K_2 is a modified Bessel function of the second kind, $\Theta = k_B T/mc^2$ is the dimensionless temperature, and β and γ have the usual meaning. For this distribution the first and second moments are $\langle \gamma \rangle \simeq 3\Theta$ and $\langle \gamma^2 \rangle \simeq 12\Theta^2$, respectively, yielding

$$l_{\text{cool}} \simeq \frac{(3\pi/2)e}{\sigma_T \Theta^2 B_0} \rho_0, \quad (1.37)$$

with $\rho_0 = \Theta mc^2/(eB_0)$ the relativistic plasma gyroradius and B_0 the characteristic magnetic field strength (Kirk and Skjæraasen, 2003). Thus, we could regulate the synchrotron radiation efficiency by changing the dimensionless temperature Θ .

ZELTRON code can also return radiation output in the form of spectral energy distributions and lightcurves for the synchrotron process. The emitted synchrotron spectrum is computed by summing the contributions from every macroparticle:

$$\begin{aligned} L_{\text{syn}}(\nu) &= \frac{\sqrt{3}e^2}{c} \sum_k N_k F(\xi) \Omega_{\text{syn}} \\ F(\xi) &= \xi \int_{\xi}^{\infty} K_{5/3}(x) dx \\ \xi &= \frac{4\pi\nu}{3\gamma^2 \Omega_{\text{syn}}}, \quad \Omega_{\text{syn}} = \frac{e}{m_e c} |(\mathbf{E} + \mathbf{n} \times \mathbf{B}) \times \mathbf{n}| \end{aligned} \quad (1.38)$$

where N_k is the number of electrons represented by the k-macroparticle, $\mathbf{n} = \mathbf{v}/|\mathbf{v}|$ is the macroparticle velocity unit vector, and $K_{5/3}$ is a modified Bessel function of the second kind (see Blumenthal and Gould, 1970; Nalewajko et al., 2018).

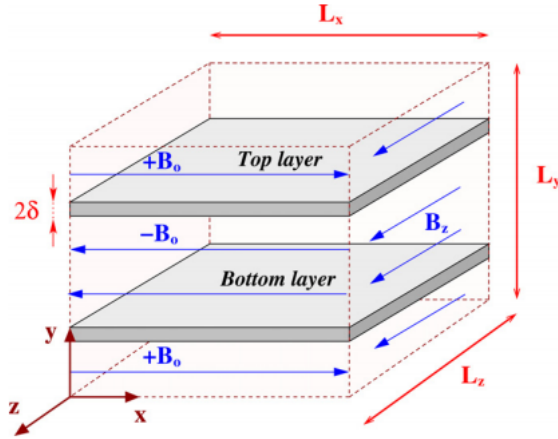


Figure 1.12: Initial setup for 3D magnetic reconnection simulations with periodic boundaries. Since the magnetic field is reversed twice, electromagnetic perturbations crossing either boundary emerge at the opposite boundary. Similarly, particles escaping through any boundary are injected at the opposite boundary with the same momenta. Schematic figure from [Cerutti et al. \(2014\)](#).

1.5 Simulation details

The simulation setups are described in the papers, although some further details were not included in the description of the simulations in our first article. In the following subsections, we explain in more detail the open boundary configuration and the method used to identify plasmoids from the simulation results.

1.5.1 Implementation of open boundary condition for the RMR simulations

In order to perform simulations of magnetic reconnection, an equilibrium subject to instabilities is initialized. [Harris \(1962\)](#) presented an equilibrium configuration with an extended current layer separating magnetic reversal, where the magnetic field gradient across the layer is supported by the electric current and the plasma pressure of the current layer. This configuration is known as the Harris layer configuration,

$$B_x = -B_0 \tanh(y/\delta), \quad n = n_0 \left(\cosh\left(\frac{y}{\delta}\right) \right)^{-2} \quad (1.39)$$

where B_0 , δ , n_0 are, respectively, the magnetic field strength outside the current layer, the half-thickness of the layer, and the plasma number density at the layer center. In our simulations, the current layer is realized using a population of drifting particles with a Maxwell-Jüttner momentum distribution that is Lorentz-boosted in the z -direction with drift velocity $\beta_d = 0.3$. Besides, we used a population of background particles characterized by uniform density and zero drift velocity.

Most of the simulations performed for the study of relativistic magnetic reconnection are initialized with a configuration including two Harris layers, e.g., [Cerutti et al. \(2014\)](#); [Nalewajko et al. \(2015\)](#); [Werner et al. \(2016\)](#). Since the two Harris layers have opposite current directions, they reverse twice the magnetic field direction, see Fig. 1.12. This configuration can be implemented in the simulation domain with periodic boundary conditions for particles and fields.

Magnetic reconnection in periodic boundaries is not steady since the outflows, at both sides of the

reconnecting region, interact with each other. In order to maintain a steady-state relativistic magnetic reconnection, we had to implement open boundary conditions against the reconnection outflows. They would prevent the reconnection from stalling due to impeded outflows resulting from periodic boundary conditions, which may result in the underestimation of the outflow velocities that have a strong influence on the emission models due to the importance of the relativistic beaming effect. We adopted a configuration with a single Harris layer along the x coordinate ($y = 0$) within a tall 2D domain $0 \leq x \leq L_x$, $-L_y/2 \leq y \leq L_y/2$ of length ratio $L_y = 4L_x$. This configuration results in a large reservoir of fresh magnetized plasma inflowing towards the reconnecting region, and the reconnection process is unaffected by perturbations that may travel along L_y .

Absorbing boundary conditions for the fields were fully implemented at the left/right boundaries of the 2D computational domain, $x = 0$ and $x = L_x$. For that, we defined a new parameter $\lambda(x) = 0.5(|x - x_{\text{abs}}|/\Delta_{\text{abs}})^3$ where x_{abs} is the position of the inner edge of the absorbing layer and $\Delta_{\text{abs}} = 30 \text{ dx}$ is the thickness of the absorbing layer (dx is the length in the x -direction of a computational grid cell). Two absorbing layers were placed just within the left/right boundaries and the field absorption was performed every time step:

$$\begin{aligned} \mathbf{B}(x) &\longrightarrow \mathbf{B}(x) + \lambda(x)[\mathbf{B}_{\text{ini}}(x) - \mathbf{B}(x)] \\ \mathbf{E}(x) &\longrightarrow \mathbf{E}(x) + \lambda(x)[\mathbf{E}_{\text{ini}}(x) - \mathbf{E}(x)], \end{aligned} \quad (1.40)$$

where $\mathbf{B}_{\text{ini}}(x)$ and $\mathbf{E}_{\text{ini}}(x)$ are the initial profiles of magnetic and electric fields, i.e., $B_{\text{ini},x}$ follows the Harris layer prescription (see Eq.1.39) and the rest of the initial fields are set to zero. Across the top/bottom boundaries, $y = -L_y/2$ and $y = L_y/2$, we reversed the magnetic field component B_x . Since the particle momenta were unaffected when the particles crossed the top/bottom boundaries, we also reversed the electric field component E_z across the top/bottom boundaries, however, there were still some spurious electric perturbations that we decided to suppress using absorbing layers for E_z similar to those along the left/right boundaries.

For the particles, we had periodic boundary conditions at top/bottom boundaries, so particles could cross with unaffected momenta. On the other hand, at the left/right boundaries, we implemented open boundary conditions. The escaping particles were removed from the memory and fresh particles were introduced. The injection of fresh particles was required in order to avoid a pressure and current gap, left at the current layer edges by the escaping particles, that would travel towards the central region of the current layer where the reconnection was taking place. In order to maintain a steady configuration, the flux and distribution of fresh particles should match the flux and distribution of escaping particles. The particle flux across the $x = 0$ and $x = L_x$ boundaries, $F(u, \mu)$ (with u the dimensionless particle momentum, and $\mu = u_x/u$ the relative momentum component normal to the boundary) would be given by

$$F(u, \mu) = \frac{dN(u, \mu)}{dt} = v_x \frac{dN(u, \mu)}{dx} \quad (1.41)$$

where $N(u, \mu)$ is the steady-state momentum distribution of particles and $v_x = v\mu = c\beta\mu = (cu/\gamma)\mu$ is the x -component of the velocity for each particle. Assuming that u and μ are not related, we can write $N(u, \mu) = Nf(u)g(\mu)$, with the f and g distributions normalized as, $\int_0^\infty f(u)du = 1$, $\int_{-1}^1 g(\mu)d\mu = 1$. For isotropic distribution, $g(\mu) = 1/2$. Then,

$$F(u, \mu) = \frac{u\mu c}{\gamma} \frac{dN}{dx} f(u) \frac{1}{2} = \frac{u\mu c}{\gamma} n f(u) \frac{1}{2} \quad (1.42)$$

where $n = dN/dx$ is the particle density per unit of x .

The total flux of fresh particles through the left boundary ($\mu > 0$):

$$F_{\text{tot}} = \int_{\mu=0}^{\mu=1} \int_{u=0}^{u=\infty} F(u, \mu) du d\mu = \frac{n}{2} \int_{\mu=0}^{\mu=1} \mu d\mu \int_{u=0}^{u=\infty} \frac{u}{\gamma} f(u) du = \frac{nc}{4} \int_{u=0}^{u=\infty} \beta f(u) du. \quad (1.43)$$

The last integral is the average of β . In our case, the initial momentum distribution for relativistic particles is the Maxwell-Jüttner distribution, which for $\Theta \gg 1$ results in $\int_{u=0}^{u=\infty} \beta f(u) du \simeq 1$. Finally, with our choice of time step $dt = (0.9/\sqrt{2})(dx/c)$, we have that

$$F_{\text{tot}} dt = n \frac{0.9}{4\sqrt{2}} dx \int_{u=0}^{u=\infty} \beta f(u) du \approx 0.15 dN \quad (1.44)$$

Hence, at every computational iteration, we were injecting, at each cell along the boundaries, around 15% of the initial number of particles. Both initial particle distributions, background and drifting particle populations, were injected as they were initialized.

1.5.2 Implementation of plasmoid tracker for the RMR simulations

Studies focused on the properties of plasmoids require identification of the boundaries that delimit them. Since plasmoids are magnetic islands, they are commonly identified (in 2D setups in the (x,y) plane) as centered at the maxima of the z-component of the magnetic vector potential, A_z , separated by X-points (see Fig. 1.7) that are identified as the minima of A_z . Sironi et al. (2016) were defining plasmoids as regions within equipotential lines corresponding to a higher level of two adjacent A_z minima. They used all of such plasmoid areas to average their parameters.

In order to save computational resources, rather than frequently storing 2D images of the computational domain, we were saving one-dimensional x-profiles every timestep. Each of these x-profiles contained the parameters y-averaged across a narrow rectangle with size $L_x \times \delta$ and centered at the reconnection layer (where L_x is the extension in the x-direction of our computational domain and δ is the initial Harris layer half-thickness). This rectangle was chosen to be narrow in order to resolve the internal structure of plasmoids of different sizes, since they have quasi-spherical shapes (Sironi et al., 2016; Ortuño-Macías and Nalewajko, 2020). In addition to the condition of maximum-minimum A_z pairs for the identification of plasmoids, we had to check more requirements in order to avoid false identifications of irregularities in the A_z x-profiles. Thus, we searched for pairs of a B_y minimum followed to the right by a B_y maximum, between which are located the peaks of A_z and particle density n . Besides, we constrained the plasmoid identification to the pairs whose n and A_z maxima were placed at distances less than $4 dx$, with dx the x-dimension of a grid cell. Finally, in order to reduce irregularities in the definition of plasmoid limits, we chose not to record the plasmoid histories when there was not a gap between plasmoids (i.e., they share a common local A_z minimum), and when one of the plasmoid layer edges were close ($\Delta x \leq 100 dx$, with dx the x-length of a cell) to the left/right boundaries of the computational domain. In contrast to Sironi et al. (2016), we distinguished two plasmoid structures, the *core* delimited by the minimum-maximum B_y pair (green vertical stripes in Fig. 1.13) and the *layer* as the remaining region (magenta vertical stripes in Fig. 1.13), with different properties (Petropoulou and Sironi, 2018; Ortuño-Macías and Nalewajko, 2020).

For our simulations with efficient radiative cooling, i.e., synchrotron cooling length of the order of the computational box size, regions of high particle density manifested unphysical numerical electrostatic

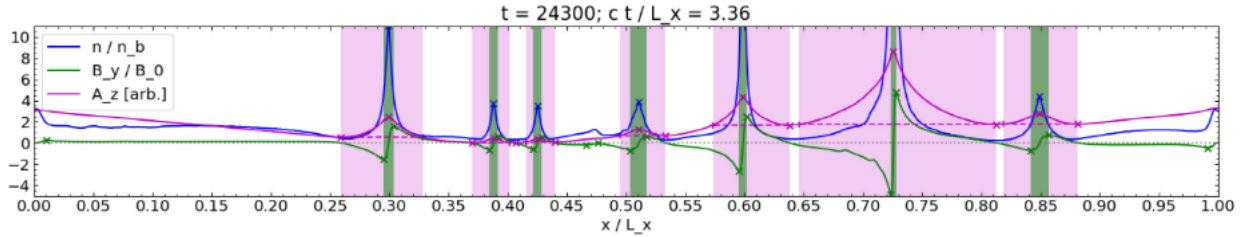


Figure 1.13: X-profiles of y-averaged properties within a narrow rectangle centered at the reconnection layer during one of our simulations of open-boundary plasmoid RMR. The blue, green, and magenta lines correspond to the x-profiles for the density, the magnetic field component B_y , and the magnetic potential vector component A_z . Vertical stripes represent the width assigned to plasmoid cores (green) and to plasmoid layers (magenta). Figure from [Ortuño-Macías and Nalewajko \(2020\)](#).

instability that could eventually scale up to magnitudes higher than B_0 . These instabilities originated from unresolved Debye length, $\lambda_D = \sqrt{(\Theta mc^2)/(4\pi nq^2)}$, where $\Theta = (k_B T)/(mc^2)$ is the dimensionless temperature, and n is the particle density. In order to prevent the Debye length from decreasing too much, we decided to turn off the synchrotron emission losses in those cells where the Debye length became smaller than the size of the cell, $\lambda_D < dx$, similarly to the method used by [Hakobyan et al. \(2019\)](#).

1.6 Motivation and thesis overview

Magnetic dissipation and particle acceleration mechanisms are required in order to explain the observed features of the relativistic jets of AGN and other high-energy astrophysical phenomena. For a long time, it has been under debate what mechanism better suits the emission signatures, how it performs, and where it happens. It has been only during the last years when kinetic simulations became able to calculate, from first principles, the effects of instabilities, such as the tearing instability that is generating plasmoid chains in reconnection layers or the current and pressure-driven instabilities. In our research, we have focused on these two mechanisms.

1.6.1 Paper I: Radiative kinetic simulations of steady-state relativistic plasmoid magnetic reconnection

The study of the steady-state relativistic magnetic reconnection is key in order to characterize the formation of plasmoid chains, providing the statistics of their properties that allow to model them as the emitting regions of the rapid flares of blazars. By means of open-boundary PIC simulations in which a steady state could be reached, it was found that the plasmoid sizes follow a power law and that their bulk acceleration is anti-correlated with their growth ([Sironi et al., 2016](#)). By post-processing plasmoid properties, [Morris et al. \(2019\)](#) found that synchrotron self-Compton emission from plasmoids could not reach the TeV luminosities observed in blazar flares. [Christie et al. \(2019\)](#) calculated synchrotron and inverse Compton emission lightcurves for blazars assuming that the reconnection layer is placed within a jet. Their model was able to explain the multi-timescale variability of blazar emission, and the variability of computed lightcurves was found to be strongly dependent on the orientation of the

relativistic reconnection outflow with respect to the bulk jet motion and the line of sight direction.

However, these post-processing models were based on PIC simulations that did not include radiative effects in the particle equations of motion. Recent kinetic simulations of relativistic magnetic reconnection included synchrotron and inverse Compton radiation drag force in the dynamics of the plasma particles (Nalewajko et al., 2018; Hakobyan et al., 2019; Schoeffler et al., 2019). They consistently found that due to radiation losses the particle acceleration efficiency is reduced in comparison with non-radiative PIC results. Then, it could be expected that the formation, composition, and development of plasmoid chains could also be affected.

In our first study (Ortuño-Macías and Nalewajko, 2020), we perform 2D PIC simulations of radiative pair plasma relativistic magnetic reconnection, where the steady-state is achieved thanks to open boundaries that allow for unimpeded outflows and active reconnection is maintained for a long time thanks to a tall computational domain, i.e., $L_y = 4L_x$ with L_x the physical size in the x-direction.

The generated plasmoid chains show that plasmoids achieve a wide variety of sizes. The plasmoid velocities present anti-correlation with their sizes, which confirms the results of Sironi et al. (2016). Small plasmoids are able to quickly achieve relativistic bulk velocities while large plasmoids slowly reach mildly relativistic velocities, $v \sim 0.4c$, staying for longer in the reconnection layer and trapping small plasmoids. We distinguish between two different regions within the plasmoids, the layer and the core. The layers present weak synchrotron emission that varies with the plasmoid size, while the dominant contribution to the synchrotron emission originates from plasmoid cores. The cores of large plasmoids present the highest emissivity, up to 4 orders of magnitude higher than the cores of small plasmoids. The cores of large plasmoids are thus cooled down much more efficiently, which enhances their densities.

The gaps between plasmoids along the reconnection layer are filled with plasma outflows of highly relativistic bulk velocities. These outflows are called minijets and we find that they contain the most energetic particles, but have a minor contribution to the synchrotron emission because of their low density.

We also collect synchrotron lightcurves observed in two cardinal directions along the reconnection layer. Despite weak relativistic beaming, the dominant emission sources are the large plasmoids. Despite the high radiative efficiency, emission from large plasmoids is not contained within the simulation boundaries. We observe rapid and bright flares that originate from tail-on collisions between small/fast and large/slow plasmoids.

1.6.2 Paper II: Kinetic Simulations of Instabilities in Cylindrical Magnetized Jets

Recently, kinetic simulations have been performed in order to study the evolution of the particle energy distribution in relativistically magnetized jets during the development of current-driven and pressure-driven instabilities, mainly kink and pinch modes. Alves et al. (2018) studied a jet containing pair plasma where the magnetic field is mainly toroidal and the MHD equilibrium is attained by the gas pressure balance, i.e., z-pinch configuration. On the other hand, Davelaar et al. (2020) performed kinetic simulations for the force-free screw-pinch setup, i.e., the support for the toroidal magnetic field required for the MHD equilibrium is achieved by only the poloidal magnetic field. Alves et al. (2018) found particle acceleration due to coherent ideal MHD electric field ($\mathbf{E} = -\mathbf{v} \times \mathbf{B}$) that developed during the instabilities growth. They argued that this electric field is able to accelerate particles while they are confined within the jet, and defined the energy limit, ϵ_{conf} . Davelaar et al. (2020) also found in

their setup particle acceleration reaching $\gamma_{\max} \approx (1/6)\epsilon_{\text{conf}}$. In addition to ideal electric fields, non-ideal electric fields, i.e., parallel to the local magnetic field, were found by them to accelerate particles.

In our second project (Ortuño-Macías et al., 2022), we perform 3D kinetic simulations of cylindrical relativistically magnetized jets populated with pair plasma. Our simulation setup is designed to bridge between the two models proposed before, by means of a single parameter that defines how much pressure is asserted by the gas over the pressure of the poloidal component of the magnetic field. We also investigate the effect of the power-law index of the radial profile of the toroidal magnetic field. We further investigate the energy limit introduced by Alves et al. (2018) in order to better understand the underlying mechanism.

We find that for every investigated configuration, a kink mode consistently arises in the inner core of the jet. The axial electric field presents growth timescales consistent with the results of analytical MHD models. For configurations with sufficient gas pressure support, a pinch mode appears as well, achieving a similar contribution to the axial electric field as the kink mode. We could differentiate between two phases of magnetic dissipation, the fast and slow dissipation phases. We find that particle acceleration is provided mainly by the coherent axial electric field E_z that is induced during the fast magnetic dissipation phase. We argue that the particle energy limit found by Alves et al. (2018) is due to the finite duration of the fast dissipation phase. In contrast with Davelaar et al. (2020), we find that the screw-pinch configuration presents minor net contributions to particle acceleration by non-ideal electric fields ($\mathbf{E} \parallel \mathbf{B}$). This discrepancy could be due to the lower magnetization of our configurations.

1.7 Future prospects

Investigating the mechanisms that drive magnetic dissipation within AGN jets is key to understanding how and where is the Poynting flux dominated regime, in which these jets are expected to be launched, transiting to the particle momentum dominated regime. These mechanisms could be either internal or external, i.e., being localized in small regions compared to the characteristic radius of the jet or affecting the global structure of the jet (which could trigger further localized magnetic dissipation mechanisms). The magnetic dissipation mechanisms may affect the dynamics, kinematics, and global structure of the jet. Furthermore, the particle populations resulting from these acceleration mechanisms are required for modeling the observed emission from blazars.

Direct comparison between simulation results and observations is required in order to differentiate which mechanisms are at play when the most conspicuous features of blazar emission appear. However, kinetic simulations need to resolve microphysical length scales (i.e., gyroradius), which implies a vast length scale separation between simulations and astrophysical objects. Extrapolation of the simulation results (e.g., Petropoulou et al., 2016), has been used in order to reproduce the observations. Another method to overcome the length scale separation is to perform global (computational length scales similar to astrophysical ones) MHD simulations, and identify regions where microphysical acceleration mechanisms may occur (see for instance Kadowaki et al., 2021), adding there the energetic particles obtained from PIC simulation results, and integrating the emission from each of these regions.

Recent PIC simulations have explored the polarization outcome from magnetic reconnection (Zhang et al., 2018; Hosking and Sironi, 2020). They found polarization angle rotations similar to those observed during campaigns of polarimetric blazar monitoring (e.g., Angelakis et al., 2016). Integration

of polarized radiation is yet to be explored by means of PIC simulations for instabilities of cylindrical magnetized jets that accelerate particles.

Further development of modern observatories will certainly help in providing more accurate data. Gamma-ray observations with higher time resolution will allow to distinguish even shorter variability time scales that could be associated with coalescence of plasmoids in the RMR events ([Zhang et al., 2018](#); [Ortuño-Macías and Nalewajko, 2020](#)). Polarimetric campaigns, such as the ongoing observations from the Imaging X-ray Polarimetry Explorer telescope (e.g., [Di Gesu et al., 2022](#)), will further elucidate the jet characteristics and provide clues to constrain the alternative particle acceleration mechanisms.

Chapter 2

Paper 1: Radiative kinetic simulations of steady-state relativistic plasmoid magnetic reconnection

Radiative kinetic simulations of steady-state relativistic plasmoid magnetic reconnection

José Ortuño-Macías[★] and Krzysztof Nalewajko[Ⓘ]

Nicolaus Copernicus Astronomical Center, Polish Academy of Sciences, Bartycka 18, PL-00-716 Warsaw, Poland

Accepted 2020 June 25. Received 2020 May 18; in original form 2019 November 8

ABSTRACT

We present the results of two-dimensional particle-in-cell (PIC) simulations of relativistic magnetic reconnection (RMR) in electron–positron plasma, including the dynamical influence of the synchrotron radiation process, and integrating the observable emission signatures. The simulations are initiated with a single Harris current layer with a central gap that triggers the RMR process. We achieve a steady-state reconnection with unrestricted outflows by means of open boundary conditions. The radiative cooling efficiency is regulated by the choice of initial plasma temperature Θ . We explore different values of Θ and of the background magnetization σ_0 . Throughout the simulations, plasmoids are generated in the central region of the layer, and they evolve at different rates, achieving a wide range of sizes. The gaps between plasmoids are filled by smooth relativistic outflows called minijets, whose contribution to the observed radiation is very limited due to their low-particle densities. Small-sized plasmoids are rapidly accelerated; however, they have lower contributions to the observed emission, despite stronger relativistic beaming. Large-sized plasmoids are slow but produce most of the observed synchrotron emission, with major part of their radiation produced within the central cores, the density of which is enhanced by radiative cooling. Synchrotron light curves show rapid bright flares that can be identified as originating from mergers between small/fast plasmoids and large/slow targets moving in the same direction. In the high-magnetization case, the accelerated particles form a broken power-law energy distribution with a soft tail produced by particles accelerated in the minijets.

Key words: acceleration of particles – magnetic reconnection – plasmas – relativistic processes – methods: numerical.

1 INTRODUCTION

Signatures of non-thermal particle energy distributions are commonly observed in the high-energy astrophysical phenomena such as gamma-ray bursts (e.g. Piran 2004), pulsar wind nebulae (e.g. Buehler et al. 2012), and blazars (e.g. Madejski & Sikora 2016). What these diverse sources have in common is very broad photon spectra indicating broad non-thermal energy distributions of the radiating particles.

Blazars are a subclass of active galactic nuclei (AGN), in which a relativistic jet emerging from the supermassive black hole (SMBH) is aligned with our line of sight (Urry & Padovani 1995). They are extremely luminous sources of radiation that spans the entire electromagnetic spectrum from radio up to very high-energy γ -rays (\sim TeV). The extreme broadness and power-law appearance of the blazar spectra are signatures of an efficient non-thermal particle acceleration (NTPA) process. Two major spectral components are typically observed with regular characteristics (Fossati et al. 1998; Ghisellini et al. 2017), with the low-energy one (radio to optical/UV/X-rays) interpreted as synchrotron emission, and the high-energy one (mainly γ -rays) due to either leptonic (inverse Compton) or hadronic processes (e.g. Sikora et al. 2009; Böttcher et al. 2013).

The emission of blazars is also characterized by strong variability on time-scales ranging from decades (e.g. Ahnen et al. 2016; Goyal et al. 2017) to minutes (e.g. Aharonian et al. 2007, 2009; Albert et al. 2007; Meyer, Scargle & Blandford 2019). The shortest variability time-scales are much shorter than the light-crossing time (\sim hours) of the gravitational radius of the SMBH contained in these type of AGN ($M_{\text{BH}} \sim 10^9 M_{\odot}$). Such short variability time-scales and high luminosities require very compact emitting regions within the jet (Levinson 2007; Begelman, Fabian & Rees 2008; Katarzyński et al. 2008).

Compact regions containing relativistic particles and magnetic fields have been often invoked to explain the multiwavelength emission of blazars (e.g. Kirk, Rieger & Mastichiadis 1998; Chiaberge & Ghisellini 1999). Theoretical models for the formation of collimated jets with relativistic velocities require relativistically magnetized environments¹ (Blandford & Znajek 1977; Li, Chiueh & Begelman 1992; Komissarov et al. 2007). In such environments, shock waves are weak structures that do not provide enough energy dissipation to power the observed emission (Sironi, Petropoulou & Giannios 2015).

Magnetic reconnection is a dissipation mechanism that is most efficient in strongly magnetized plasmas. During the reconnection,

¹In general, magnetization parameter is defined as $\sigma = B^2/(4\pi w)$, where B is the magnetic field strength and w is the relativistic enthalpy density of the matter.

[★] E-mail: jortuno@camk.edu.pl

free magnetic energy is transferred to the thermal heating and bulk acceleration of plasma, as well as to the NTPA process (Zweibel & Yamada 2009). Numerous arguments point to the relativistic magnetic reconnection (RMR) as the process responsible for the multi-wavelength and multi-time-scale variability emission of blazars (Sironi et al. 2015). A basic requirement for reconnection to occur in relativistic jets is to have local inversions of the magnetic field lines, which may be caused by internal jet instabilities, in particular, the current-driven kink modes (Begelman 1998; Giannios & Spruit 2006; Alves, Zrake & Fiuza 2018; Bromberg et al. 2019), or by global magnetic polarity reversals (Lovell, Newman & Romanova 1997; Giannios & Uzdensky 2019).

Traditional models of magnetic reconnection (Parker 1957; Sweet 1958; Petschek 1964) have been adapted to the relativistic regime by Lyutikov & Uzdensky (2003) and Lyubarsky (2005). The latter work became a basis for the minijets model of relativistic bulk outflows driven by the RMR (Giannios, Uzdensky & Begelman 2009; Nalewajko et al. 2011). Other works emphasized the fundamental role of plasmoids (or magnetic flux tubes) that arise spontaneously in sufficiently long and thin current layers due to the tearing instability (Loureiro, Schekochihin & Cowley 2007; Giannios 2013). Plasmoids trap energized particles and evacuate them together with the reconnected magnetic field from the active magnetic X-points, enhancing the overall reconnection rate² (Uzdensky, Loureiro & Schekochihin 2010).

The NTPA mechanism in the case of RMR has been studied extensively by means of kinetic particle-in-cell (PIC) numerical simulations. In the most basic case of electron–positron pair plasma, it has been established that NTPA produces power-law energy distributions of particles $N(E) \propto E^{-p}$ with localized power-law indices as hard as $p \simeq 1$ in the limit of $\sigma \gg 1$ (Zenitani & Hoshino 2001; Guo et al. 2014; Sironi & Spitkovsky 2014; Werner et al. 2016), converging, however, to $p \simeq 2$ in the long term (Petropoulou & Sironi 2018).

Most PIC simulations of the RMR are initiated from Harris-type current layers contained in periodic domains. In the relatively small domains, this leads to the cancellation of reconnection outflows momenta and to the formation of artificially large single plasmoids. An alternative approach is to use open boundaries that allow outgoing particles to escape freely and absorb the outgoing Poynting flux (Daughton, Scudder & Karimabadi 2006). This approach allows to investigate magnetic reconnection as a sustained steady-state process with unimpeded outflows approaching the terminal Alfvén velocity and continuous generation and evolution of plasmoids (Daughton & Karimabadi 2007).

The open-boundary approach has been first applied to the case of RMR by Sironi, Giannios & Petropoulou (2016), who investigated the statistical properties of plasmoids, determined their size distribution as a power law, and demonstrated an anticorrelation between plasmoid growth and bulk acceleration. The corresponding predictions for the variability of non-thermal radiation were applied to explain the observational characteristics of blazar flares (Petropoulou, Giannios & Sironi 2016). Based on the plasmoid scaling laws, a stochastic model for the evolution of plasmoid chains was developed by Petropoulou et al. (2018). The results of these PIC simulations were also post-processed to calculate light curves of synchrotron and inverse Compton emission as would be observed if the reconnection region was located in a relativistic jet (Christie et al. 2019a, 2020). A semi-analytical model of broad-band emission

from reconnection plasmoids in the context of blazar flares was also developed by Morris, Potter & Cotter (2019).

Other numerical studies of the RMR were performed in the context of γ -ray flares from the Crab Nebula, taking into account the effect of radiation reaction on individual particles (e.g. Cerutti et al. 2013, 2014). Recent PIC simulations that included the effects of synchrotron and inverse Compton cooling have shown that the particle acceleration can be decreased in comparison with previous non-radiative results (Nalewajko 2018; Hakobyan, Philippov & Spitkovsky 2019; Schoeffler et al. 2019; Sironi & Beloborodov 2019). We may therefore expect that evolution of plasmoids will be affected by radiative cooling.

In this work, we present the results of PIC simulations of the steady-state RMR process allowed by the open boundaries under strong radiative energy losses due to the synchrotron radiation reaction. We investigate in detail the evolution of individual plasmoids under different levels of radiative cooling and calculate accurate light curves of synchrotron radiation. We demonstrate a connection between rapid radiation flares and tail-on mergers of small/fast and large/slow plasmoids.

Plan of this work: Section 2: simulations setup; Section 3: analysis methods; Section 4.1: initial sequence; Section 4.2: evolved reconnection layer; Section 4.3: spacetime diagrams of the current layer; Section 4.4: particle density and mean energy distributions; Section 4.5: analysis of individual plasmoids; Section 4.6: acceleration and cooling of selected individual particles; Section 4.7: synchrotron light curves; Section 4.8: global energy conservation; Section 4.9: energy distributions of particles and photons; Section 5: discussion; and Section 6: conclusions.

2 SIMULATION SETUP

We make use of a custom version of the PIC code Zeltron (Cerutti et al. 2013). We perform two-dimensional simulations of relativistically magnetized pair plasma in a fixed tall domain of dimensions $L_x \times L_y$ with $L_y = 4L_x$, within the coordinate ranges $0 < x < L_x$ and $-L_y/2 < y < L_y/2$.

Our simulations are initiated from an equilibrium configuration $\mathbf{B}(t=0) = \mathbf{B}_{\text{ini}}$ and $\mathbf{E}(t=0) = \mathbf{E}_{\text{ini}} = 0$ that involves a single Harris-type current layer placed in the middle of the computational domain:

$$B_{\text{ini},x} = -B_0 \tanh(y/\delta), \quad (1)$$

where B_0 is the characteristic value of magnetic field strength, and δ is the Harris layer half-thickness. We include no initial guide field; hence, $B_{\text{ini},z} = 0$. The magnetic field gradient across the Harris layer is supported by the electric current and pressure provided by the drifting population of particles that is characterized by the Maxwell–Jüttner energy distribution with dimensionless temperature $\Theta_d = k_B T_d / (m_e c^2)$, Lorentz-boosted with the drift velocity $\beta_d = v_d/c = 0.3$, and number density

$$n_d(y) = n_{d,0} \cosh^{-2}(y/\delta), \quad (2)$$

where $n_{d,0} = \gamma_d B_0^2 / (8\pi \Theta_d m_e c^2)$, and $\gamma_d = (1 - \beta_d^2)^{-1/2}$ is the drift Lorentz factor. The Harris layer thickness is related to the nominal plasma gyroradius $\rho_0 = \Theta_d m_e c^2 / (e B_0)$ as $\delta = 2\rho_0 / (\gamma_d \beta_d)$ (Kirk & Skjæraasen 2003).

The current layer is immersed in a background plasma with the Maxwell–Jüttner energy distribution with dimensionless temperature $\Theta_b = k_B T_b / (m_e c^2) = \Theta_d \equiv \Theta$, and number density n_b that is determined by the assumed value of the magnetization

²Inflow velocity of the background plasma.

$\sigma_0 = B_0^2 / (4\pi n_b \Theta_b m_e c^2)$. The corresponding initial density contrast can be expressed as $n_{d,0}/n_b = \gamma_d \sigma_0 / 2$.

Our choice of drift velocity means that the current layer is relatively thick and hence stable to the tearing modes. We experimented with higher values $\beta_d \simeq 0.5$, which results in spontaneous formation of slowly evolving plasmoids. In order to speed up the evolution of the current layer, we follow Sironi et al. (2016) in triggering fast magnetic reconnection by placing a narrow gap ($\Delta x = 8\delta$) in the middle of the current layer. Within the trigger gap, the distribution of drifting particles is initialized with temperature reduced by a factor of 10, and with no drift velocity.

The dimensions of our computational domain are up to $N_x \times N_y = 4608 \times 18432$ cells with equal spatial resolution for both dimensions $dx = dy = \rho_0/3$, which results in the physical scales of $L_x \times L_y = (1536 \times 6144)\rho_0$. The temporal resolution is $dt = 0.9 dt_{\text{CFL}}$, where $dt_{\text{CFL}} = [(dx)^{-2} + (dy)^{-2}]^{-1/2}/c$ is the Courant–Friedrichs–Lewy (CFL) time-step. The initial distributions of background and drifting electrons/positrons are represented on average by 64 macroparticles per cell per species.

Our computational domain is open at left/right boundaries, where outgoing particles are removed, and fresh particles are injected at every time-step at a fixed rate calculated to maintain the initial number density of both background and drifting particles. At every time-step, we inject a fixed number of particles along each boundary $dN_{\text{inj}}/d(ct) = (\langle\beta\rangle/4)dN_{\text{ini}}/dx$, where dN_{ini} is the number of initial particles in a single grid column, and $\langle\beta\rangle = \langle|\boldsymbol{\beta}|\rangle = \langle v \rangle / c \simeq 1$ is the mean particle dimensionless velocity module.³ The injected particles are located at fixed distance just within each boundary ($x_0 = \Delta x/100$ in case of left boundary; $x_0 = L_x - \Delta x/100$ in case of right boundary). Their distribution along the y coordinate is proportional to the distribution of initial particles. The injected particles are likewise divided into background and drifting populations. A Lorentz boost is applied to the drifting particles in order to match the current density $J_{z,\text{ini}}$ of the initial Harris layer (otherwise, the initial current layer would evolve strongly from the boundaries inwards).

Within the left/right boundaries, we place the field-absorbing layers of thickness $\Delta_{\text{abs}} = 30 dx$. In the absorbing layers, in addition to the standard time advance of magnetic and electric fields, at every time-step we perform the following operation:

$$\mathbf{B}(x) \rightarrow \mathbf{B}(x) + \lambda(x) [\mathbf{B}_{\text{ini}}(x) - \mathbf{B}(x)], \quad (3)$$

$$\mathbf{E}(x) \rightarrow \mathbf{E}(x) + \lambda(x) [\mathbf{E}_{\text{ini}}(x) - \mathbf{E}(x)], \quad (4)$$

where $\lambda(x) = 0.5(|x - x_{\text{abs}}|/\Delta_{\text{abs}})^3$, and x_{abs} is the position of the absorbing layer inner edge. For the top/bottom boundaries, we apply periodic conditions for the particles and fields, while only the z -component of the electric field is absorbed using the above rule.

³The factor $\langle\beta\rangle/4$ is derived from the rate at which particles of uniform density and isotropic momentum distribution $N(\mathbf{u}) = Nf(u)g(\mu)$ cross the boundary. Here, $f(u)$ is the Maxwell–Jüttner distribution (normalized to unity) of momentum module $u = |\mathbf{u}| = \gamma\beta$ with $\gamma = (1 - \beta^2)^{-1/2} = (1 + u^2)^{1/2}$ the Lorentz factor, and $g(\mu)$ is the uniform distribution of the cosine parameter $\mu = u_x/u = \beta_x/\beta$. For isotropic target particle distribution, $g(\mu) = 1/2$ for $\mu \in [-1, 1]$; hence, $\int_{-1}^1 d\mu g(\mu) = 1$. For injected particles, this distribution is truncated to particles flowing to the domain $-\mu \in (0, 1]$ in case of left boundary, and $\mu \in [-1, 0)$ in case of right boundary. For particles of momentum \mathbf{u} , we find $dN(\mathbf{u})/d(ct) = \beta_x dN(\mathbf{u})/dx$, integrating this over \mathbf{u} , we find $dN/d(ct) = dN/dx \int_0^\infty du f(u) \int_0^1 d\mu \mu g(\mu) = dN/dx \langle\beta\rangle$ (1/4).

We apply the synchrotron radiation reaction to every particle at every time-step,⁴ following the prescription of Cerutti et al. (2013):

$$\frac{d\mathbf{u}}{dt} = -\frac{P_{\text{syn}}\mathbf{u}}{\gamma m_e c^2}, \quad P_{\text{syn}} = \frac{\sigma_T c}{4\pi} [(\gamma \mathbf{E} + \mathbf{u} \times \mathbf{B})^2 - (\mathbf{E} \cdot \mathbf{u})^2], \quad (5)$$

where $\sigma_T = (8\pi/3)r_e^2$ is the Thomson cross-section with $r_e = e^2/m_e c^2$ the classical electron radius, and $\mathbf{u} = \gamma\boldsymbol{\beta}$ is the dimensionless momentum of a particle with dimensionless velocity $\boldsymbol{\beta} = \mathbf{v}/c$ and Lorentz factor $\gamma = (1 - \beta^2)^{-1/2} = (1 + u^2)^{1/2}$. Noting that for $\gamma \gg 1$ we have $u \simeq \gamma$, the radiative cooling rate can be estimated as:

$$\frac{\partial\gamma}{\partial t} = \frac{\mathbf{u}}{\gamma} \cdot \frac{\partial\mathbf{u}}{\partial t} \simeq -\frac{P_{\text{syn}}}{m_e c^2}. \quad (6)$$

In the limit of zero electric field and isotropic particle distribution, equation (5) reduces to $P_{\text{syn}} = (4/3)\sigma_T c u^2 U_{B,0}$, where $U_{B,0} = B_0^2/8\pi$ is the initial background magnetic energy density. Taking into account that for the initial Maxwell–Jüttner distribution we have $\langle\gamma\rangle \simeq 3\Theta$ and $\langle\gamma^2\rangle \simeq 12\Theta^2$, we define the nominal cooling length as (Nalewajko, Yuan & Chruślińska 2018):

$$l_{\text{cool}} = c\tau_{\text{cool}} = \frac{\langle\gamma\rangle}{\langle|\mathbf{d}\gamma/cdt|\rangle} \simeq \frac{\langle\gamma\rangle}{\langle\gamma^2\rangle} \frac{3m_e c^2}{4\sigma_T U_{B,0}} \simeq \frac{(3\pi/2)e}{\sigma_T \Theta^2 B_0} \rho_0. \quad (7)$$

This can be compared with the radiation reaction limit on electron Lorentz factor $\gamma_{\text{rad}} = (3\rho_0/2\Theta r_e)^{1/2}$ that can be achieved locally under crossed electric and magnetic fields of equal strengths $E = B$ (e.g. Cerutti et al. 2014). We find a relation between l_{cool} and γ_{rad} by eliminating B_0 :

$$\frac{\langle\gamma\rangle}{\gamma_{\text{rad}}} = \left(\frac{27}{8} \frac{\rho_0}{l_{\text{cool}}}\right)^{1/2}. \quad (8)$$

The total synchrotron power emitted in all directions per volume element of the initial background plasma is given by:

$$\mathcal{P}_{\text{syn,b,0}} \equiv \frac{dE_{\text{syn}}}{dx dy dt} = 16c\sigma_T n_b \Theta^2 U_{B,0}. \quad (9)$$

We also collect the synchrotron radiation spectra that would be measured by observers placed at the left and right sides of the simulation domain. The total spectrum is calculated as the sum of contributions from all macroparticles present in the domain (see Nalewajko et al. 2018, and references therein).

$$L_{\text{syn}}(v) = \frac{\sqrt{3}e^2}{c} \sum_{e^+e^-} N_{e,1} F(\xi) \Omega_1, \quad (10)$$

where $F(\xi) = \xi \int_\xi^\infty K_{5/3}(x) dx$, $\xi = 4\pi v/3\gamma^2 \Omega_1$, $\Omega_1 = (e/m_e c) |(\mathbf{E} + \mathbf{n} \times \mathbf{B}) \times \mathbf{n}|$, $\mathbf{n} = \mathbf{v}/|\mathbf{v}|$, $N_{e,1}$ is the number of charged particles (either electrons or positrons) represented by a single macroparticle, and $K_{5/3}$ is the modified Bessel function of the second kind. A characteristic synchrotron frequency for monoenergetic electrons of Lorentz factor γ can be derived from the isotropic synchrotron kernel⁵:

$$\nu_{\text{syn}}(\gamma) \simeq (3/2\pi)\tilde{\xi}_0 \gamma^2 \Theta \omega_0 \equiv \left(\frac{\gamma}{\Theta}\right)^2 \nu_{\text{syn0}}. \quad (11)$$

We performed several large simulations for different values of background magnetization σ_0 and initial particle distribution temperature Θ . In Table 1, we report these parameters, as well as the

⁴We apply a restriction such that particles cannot lose more than half of their energy or reverse their momentum over a single time-step.

⁵Defined as $\mathcal{R}(\tilde{\xi}) = \tilde{\xi}^2 \{K_{1/3}(\tilde{\xi})K_{4/3}(\tilde{\xi}) - (3/5)\tilde{\xi}[K_{4/3}^2(\tilde{\xi}) - K_{1/3}^2(\tilde{\xi})]\}$, where $\tilde{\xi} = 2\pi v/3\gamma^2 \Theta \omega_0$ (Crusius & Schlickeiser 1986). Note that $\tilde{\xi} \mathcal{R}(\tilde{\xi}) \propto v F(v)$ peaks at $\tilde{\xi}_0 \simeq 0.575$.

Table 1. Designations and key parameter values for our largest simulations performed in the domain of physical width $L_x = 1536\rho_0$. Common parameters include: the initial background magnetic field strength $B_0 = 1$ G, and the initial dimensionless drift velocity $\beta_d = 0.3$. The nominal cooling length l_{cool} is calculated from equation (7), and the radiation reaction limit ratio $\langle\gamma\rangle/\gamma_{\text{rad}}$ is calculated from equation (8).

Name	σ_0	Θ	l_{cool}/L_x	$\langle\gamma\rangle/\gamma_{\text{rad}}$
s10Tl	10	$2 \cdot 10^5$	55	0.006
s10Tm	10	$5 \cdot 10^5$	8.9	0.016
s10Th	10	$1.25 \cdot 10^6$	1.4	0.039
s50Tm	50	$5 \cdot 10^5$	8.9	0.016

corresponding ratios l_{cool}/L_x and $\langle\gamma\rangle/\gamma_{\text{rad}}$. In our strong-cooling case s10Th, l_{cool} is comparable to L_x , while the initial mean particle energy $\langle\gamma\rangle$ is factor $\simeq 25$ below γ_{rad} .

3 ANALYSIS METHODS

3.1 Plasmoids identification

We describe here an automated procedure that we use for identifying individual plasmoids along the reconnection layer. During the simulations, we frequently save one-dimensional x -profiles of various parameters along the reconnection layer; more precisely, we extract these data from narrow rectangular stripes extending over $0 < x < L_x$ and $|y| < \delta/2$. For each grid cell along the x -axis, we average the data over all grid cells along the y -axis that fit within the stripe. The x -profiles were then Gaussian-smoothed with the standard deviation of 3 dx . An example of such profiles is shown in Fig. 1.

We applied the `scipy.signal.find_peaks` algorithm to identify the maxima of particle number density n (with the minimum prominence parameter of $1.5n_b$), the minima and maxima of magnetic field component B_y (with the minimum prominence of $0.02B_0$), and the minima and maxima of the magnetic vector potential component A_z (with the minimum prominence of $0.22B_0\rho_0$). Next, we searched for all ordered pairs consisting of a B_y minimum followed (to the right) by a B_y maximum. For each such pair, we checked whether between those two points there is exactly one maximum of n and one maximum of A_z . We also require that the distance between the n maximum and the A_z maximum is no more than 4 dx . Only the structures that satisfied all of the above conditions were classified as proper plasmoids. We distinguish two structures within each plasmoid, a *core* delimited by the minimum and maximum peaks of B_y (green stripes in Fig. 1), and a *layer* where A_z exceeds a threshold level equal to the higher of the closest A_z minima located on both sides of the core and excluding the core itself (light-magenta areas in Fig. 1; this is consistent with the definition of plasmoid limits adopted by Sironi et al. 2016). Qualitatively, the plasmoid cores are compact structures of high particle density, while the plasmoid layers are extended structures of relatively low particle density and closed magnetic field lines.

3.2 Local reference frames

We convert certain parameters to their values in the local reference frames. As discussed in Werner et al. (2018), in relativistically hot fluid there are two alternative ways to define a ‘co-moving’ reference frame: (1) zero-current (Eckart) frame \mathcal{O}' of velocity $\beta_1 = \langle\beta\rangle$; and (2) zero-momentum (Landau) frame \mathcal{O}'' of velocity $\beta_2 = \langle\gamma\beta\rangle/\langle\gamma\rangle$. These averages are calculated locally for all particles (electrons and positrons) in a given grid cell as $\langle a \rangle = (\sum_i a_i n_i)/(\sum_i n_i)$, where n_i

are the multiplicities of individual macroparticles such that $\sum_i n_i \equiv n$ is the local particle number density. For example, we calculate the electric field component in the Eckart frame as:

$$E'_z = \Gamma_1 (E_z + \langle\beta_x\rangle B_y - \langle\beta_y\rangle B_x) \quad (12)$$

where $\Gamma_1 = (1 - \langle\beta_x\rangle^2 - \langle\beta_y\rangle^2)^{-1/2}$ is the Eckart bulk Lorentz factor. On the other hand, we calculate the mean particle energy in the Landau frame as $\langle\gamma''\rangle = \langle\gamma\rangle/\Gamma_2$, where $\Gamma_2 = (1 - \beta_{2,x}^2 - \beta_{2,y}^2)^{-1/2}$ is the Landau bulk Lorentz factor.

4 RESULTS

4.1 Initial sequence

Fig. 2 shows the initial evolution of the reconnection layer in our reference simulation s10Tm. Each panel shows a particle number density map and magnetic field lines for a central region of our computational domain (only a 1/64 fraction of its total vertical extent), in which the current layer is contained. A centrally located gap in the current layer expands rapidly sideways towards the left/right boundaries and the initial drifting plasma component is pulled towards the boundaries by the tension of closed magnetic field lines. Magnetic reconnection is triggered in the central low-density region, sustained by a thin current layer that is unstable to tearing modes, which lead to the emergence of plasmoids.

At $ct \simeq L_x$, the swept-up fronts of the initial drifting plasma leave the left/right boundaries. From that moment on, we can describe the simulated reconnection process as steady-state, with newer plasmoids continuously generated around the centre of the layer, and older plasmoids escaping through the left/right boundaries. The upper panels of Fig. 2 demonstrate how our implementation of open boundaries works when large dense structures move across them.

We also find that the initial trigger gap induces a quasi-circular wave that propagates in all directions. The horizontal wave fronts are effectively absorbed by the left/right boundaries, while the vertical wave fronts reach the top/bottom boundaries by $ct \simeq 2L_x$ and are partially absorbed there; some very weak reflections return to the reconnection layer by about $ct \simeq 4L_x$ without a significant effect.

4.2 Evolved reconnection layer

Fig. 3 presents a selected evolved state of our reference simulation s10Tm illustrated with multiple parameters. In this snapshot centred at the reconnection midplane, we observe diverse substructures. The main current layer is observed at $0.34 < x/L_x < 0.49$, characterized by high values of the specific electric current $|j_z|/j_{\text{max}}$ (electric current density j_z close to its maximum value $j_{\text{max}} = cen$) despite low particle number density n , low bulk velocity v_x , and strong electric field E'_z (except for the two minor plasmoids located at $x \simeq 0.39L_x$ and $x \simeq 0.425L_x$).

To the left of the main current layer, behind a medium-sized plasmoid at $x \simeq 0.3L_x$, we find a relativistically fast reconnection outflow (strongly negative v_x for $x < 0.25L_x$; $\langle\gamma\rangle \gg \langle\gamma''\rangle$) due to Lorentz transformation), also characterized by moderate particle density and intrinsic temperature $\langle\gamma''\rangle/\Theta$, specific electric current $|j_z|/j_{\text{max}}$ decreasing systematically with distance, very weak intrinsic electric field E'_z , and weak synchrotron emission. This is a structure that has all characteristics of minijets – regular reconnection outflows of relativistic bulk velocity (Giannios et al. 2009; Nalewajko et al. 2011). We can easily recognize the conical geometry of the outflow region with parallel outflow velocity field (very low values of v_y),

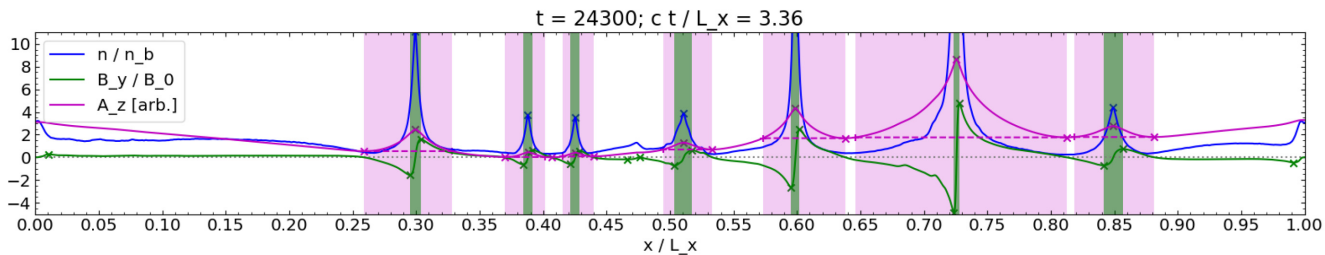


Figure 1. Profiles of particle density (blue line), magnetic field component B_y (green line), and magnetic vector potential component A_z (magenta line) measured along the reconnection layer for a selected moment of simulation $\approx 10T_m$ (cf. Fig. 3). The green vertical stripes mark the horizontal limits of plasmoid cores, and the light magenta areas mark the plasmoid layers.

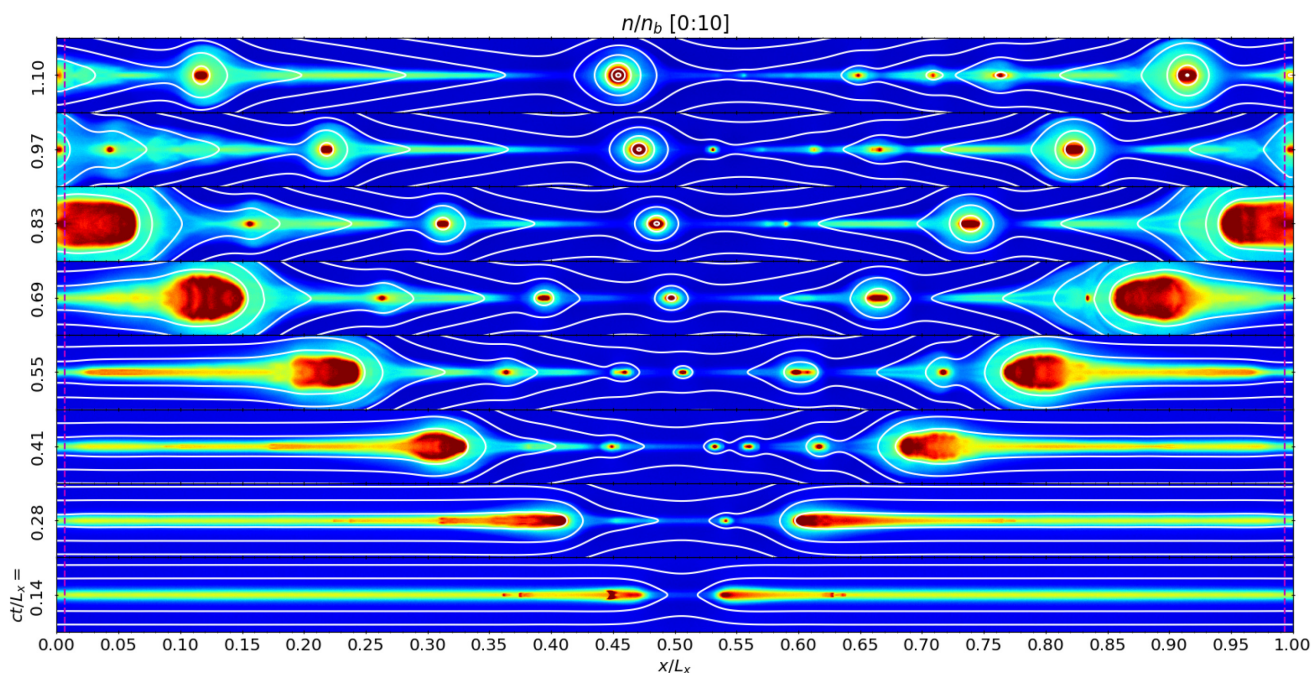


Figure 2. Initial sequence of simulation $\approx 10T_m$, presenting the logarithm of particle number density n/n_b (see the top panel of Fig. 3 for the colour scale) and the magnetic field lines (solid white lines). The dashed magenta lines indicate the limits of the field-absorbing boundary layers.

and oblique magnetic field lines crossing the outflow boundaries, as has been described by an analytical model of relativistic Petschek-type reconnection by Lyubarsky (2005). There is one qualitative difference from that model – the magnetic field lines in the outflow region are not vertical and the magnetic field gradient $\partial B_x / \partial y$ does not vanish in that region and it is supported by the non-zero electric current density j_z . We note that there is a roughly uniform vertical inflow of background plasma into the minijet region with velocity v_y (reconnection rate) of the same order as that of the inflow into the main current layer.

To the right of the main current layer, we find a group of several plasmoids of various sizes, all propagating to the right at different velocities $v_x > 0$. The largest plasmoid can be seen centred at $x \simeq 0.725L_x$; it is clearly slower than its smaller neighbour centred at $x \simeq 0.6L_x$. The smaller plasmoid is in the process of merging with the large one, even though they both propagate in the same direction. This is a natural consequence of the inverse relation between the growth and bulk acceleration of plasmoids that has been first noticed by Sironi et al. (2016).

4.3 Spacetime diagrams

Most of the information on evolution of current layers, and especially on the plasmoids, is contained along the reconnection midplane; this information can be presented very efficiently in the form of spacetime diagrams. Following the practice of Nalewajko et al. (2015), the one-dimensional parameter x -profiles described in Section 3.1 are combined into spacetime diagrams of high time resolution. Fig. 4 shows spacetime diagrams for several parameters for our reference simulation $\approx 10T_m$.

The spacetime diagrams reveal a sustained bifurcating outflow along the x coordinate (regions of negative and positive velocity component β_x) and a variety of plasmoids (indicated by enhanced plasma density and sharp positive gradients of magnetic field component $dB_y/dx > 0$), most of which are generated along the $\beta_x \simeq 0$ line. There are a few large plasmoids that evolve very slowly, their bulk velocities are non-relativistic, acceleration time-scale is long, and hence they spend more than the light-crossing time L_x/c before leaving the simulation domain. On the other hand, there are many small plasmoids that accelerate quickly to relativistic bulk velocities, and they spend

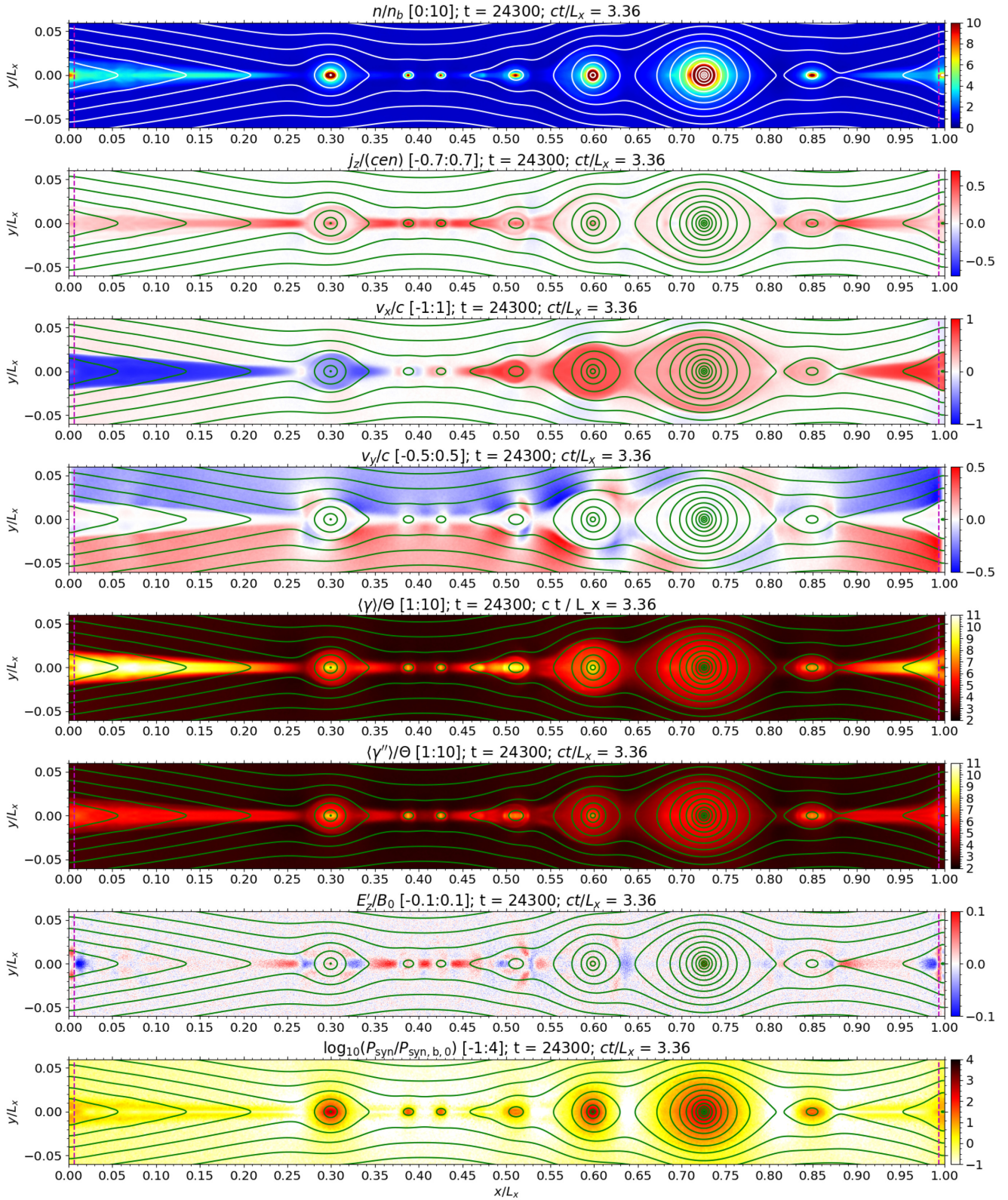


Figure 3. Selected evolved state of simulation $\epsilon 10Tm$ (the same as shown in Fig. 1). From the top, the panels show: (1) particle number density n/n_b in log scale, (2) out-of-plane electric current per particle number density $j_z/(cen)$, (3) Landau velocity component along the current layer v_x/c , (4) Landau velocity component across the current layer v_y/c , (5) mean particle Lorentz factor measured in the simulation frame $\langle \gamma \rangle / \Theta$, (6) mean particle Lorentz factor measured in the Landau co-moving frame $\langle \gamma'' \rangle / \Theta$, (7) out-of-plane electric field component measured in the Eckart co-moving frame E'_z , and (8) total synchrotron power E_{syn} in log scale. The solid white lines show the magnetic field lines, and the dashed magenta lines indicate the limits of the field-absorbing boundary layers.

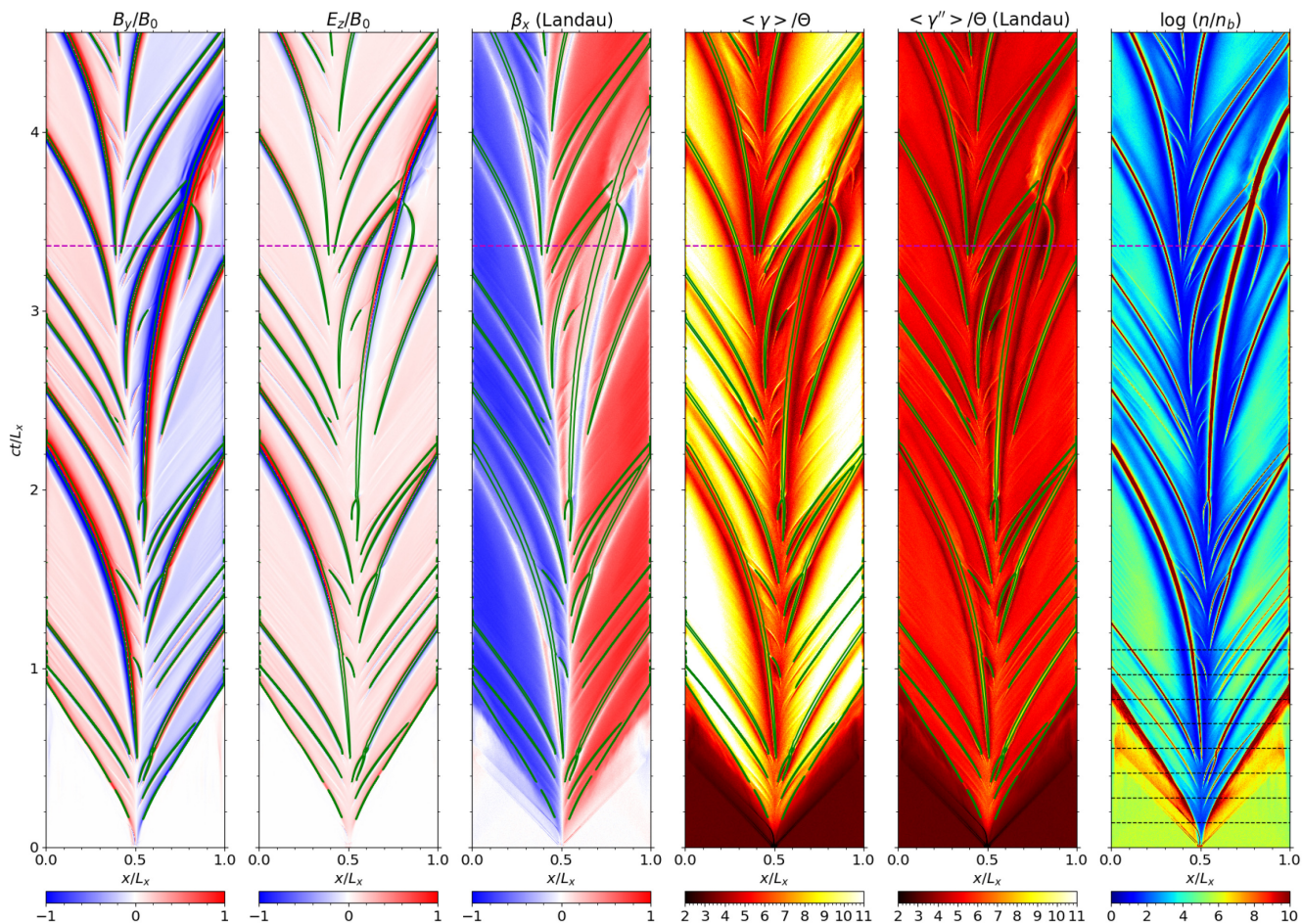


Figure 4. Spacetime diagrams extracted along the reconnection midplane for the simulation $s10Tm$. From left to right we plot: (1) the magnetic field component B_y/B_0 , (2) the electric field component E_z/B_0 , (3) the Landau-type bulk velocity component β_x , (4) logarithm of the cold magnetization parameter $\log(\sigma/\sigma_0)$, (5) mean particle Lorentz factor $\langle \gamma'' \rangle / \Theta$ measured in the Landau frame, and (6) logarithm of the particle number density $\log(n/n_b)$. In the first five panels, we show the particle number density contours $n = 7n_b$ with green solid lines. We indicate the simulation time $ct = 3.36L_x$ corresponding to the simulation state shown in Figs 1 and 3 with the magenta-dashed horizontal lines. The black-dotted horizontal lines in the last panel indicate the initial simulation states shown in Fig. 2.

less than L_x/c in the simulation domain. Small plasmoids may either escape through the boundaries or merge with a larger plasmoid. As the velocity field is generally divergent, plasmoid mergers are relatively rare; typically, they involve plasmoids of different sizes moving in the same direction (tail-on mergers). A large plasmoid can attract nearby small plasmoids and can even reverse their motion, e.g. Fig. 3 shows that at $ct/L_x = 3.36$, a small plasmoid centred at $x \simeq 0.85L_x$ has $\beta_x > 0$; however, the spacetime diagrams reveal that it will merge with the large plasmoid located on its left side by $ct/L_x \simeq 3.6$.

The regions between plasmoids are characterized by roughly uniform electric field component $E_z \simeq 0.1B_0$ and by two-value magnetic field component $B_y \simeq \pm 0.15B_0$ (positive where $\beta_x < 0$ and negative where $\beta_x > 0$). The uniformity of electric field measured in the simulation frame is consistent with the uniform reconnection rate indicated in the β_y panel of Fig. 3. It is remarkable, given the non-uniformity of electric field measured in local Eckart frames E'_z , as shown in another panel of Fig. 3. This indicates a smooth connection between the minijet outflows (where E'_z is close to zero) and the proper magnetic diffusion areas (where E'_z is strong).

High-density regions of the plasmoids – essentially the plasmoid cores – are initially characterized by enhanced temperatures (mean particle energies measured in the local Landau frames reaching

values of $\langle \gamma'' \rangle \simeq 10\Theta$) due to the heating of particles in the reconnection process. Our spacetime diagram of $\langle \gamma'' \rangle / \Theta$ demonstrates that the cores of large plasmoids cool down gradually.

In Fig. 5, we compare the spacetime diagrams of $\langle \gamma'' \rangle / \Theta$ for three simulations with different nominal cooling lengths l_{cool} . In the simulation $s10T1$, in which $l_{cool} > L_x$, we find that plasmoid temperatures are the highest, showing no signs of cooling over the light-crossing time-scale L_x/c . On the other hand, in the simulation $s10Tb$, the plasmoid temperatures are the lowest and they eventually become even lower than for the plasma between the plasmoids.

4.4 Plasma density and temperature distributions

The left-hand panel of Fig. 6 compares the distributions of particle number density n/n_b based on the spacetime diagrams of three simulations with $\sigma_0 = 10$ and with different efficiencies of radiative cooling. The distributions form power-law tails with the slope of ~ -2.3 , independent of the cooling efficiency. However, the highest values of the particle density increase with stronger cooling from $n_{max} \simeq 150n_b$ for the simulation $s10T1$ to $n_{max} \simeq 1500n_b$ for the simulation $s10Tb$. The highest particle densities are realized in the

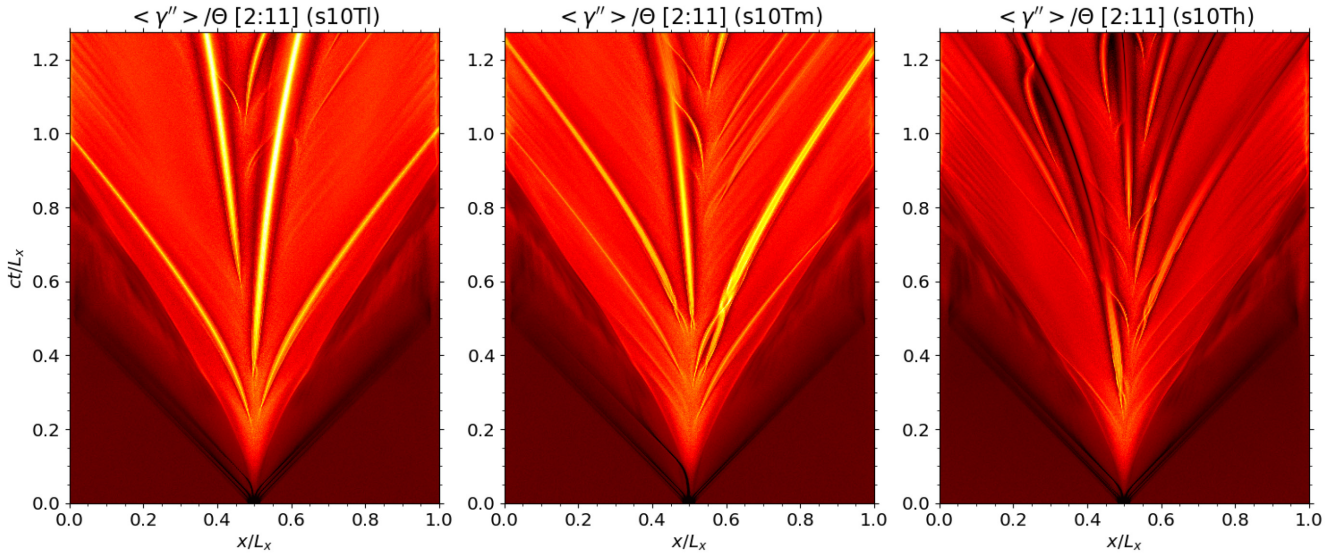


Figure 5. Spacetime diagrams of average particle Lorentz factor $\langle \gamma'' \rangle / \Theta$ measured in the Landau frame compared for three simulations characterized by different radiative cooling efficiencies.

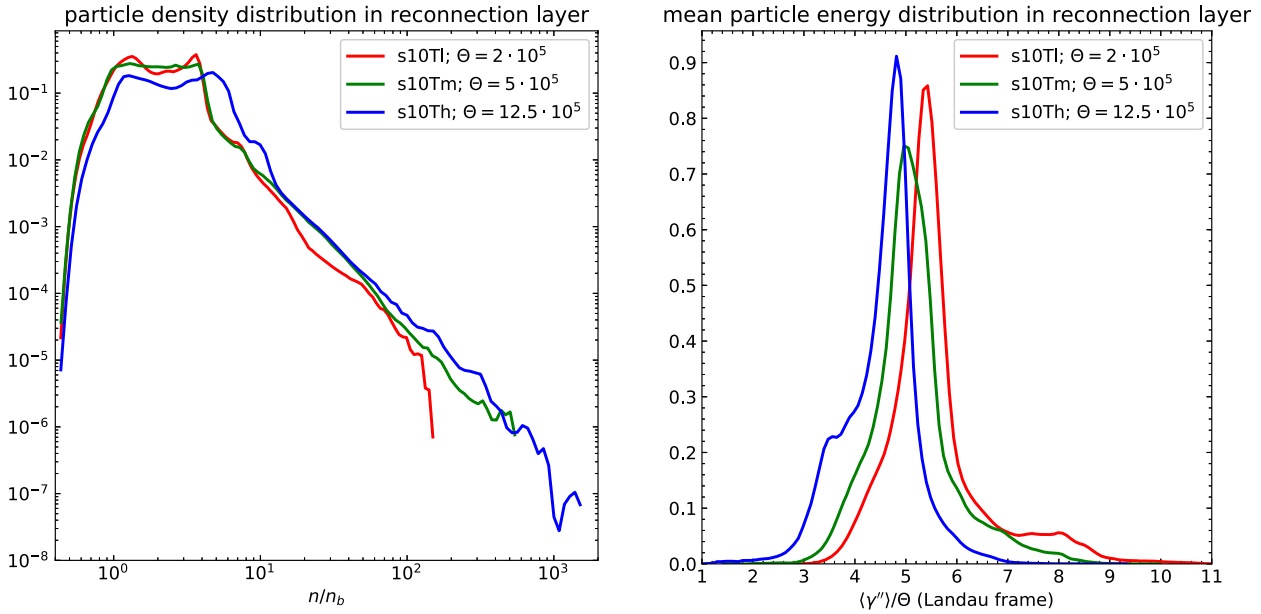


Figure 6. Distributions of particle density n/n_b (left-hand panel) and mean particle energy $\langle \gamma'' \rangle / \Theta$ calculated in the Landau co-moving frame (right-hand panel) extracted from the spacetime diagrams probing narrow regions along the reconnection layers for the three simulations with $\sigma_0 = 10$ that differ by initial gas temperature Θ and hence by the radiative cooling efficiency (higher Θ corresponds to more efficient cooling).

cores of large plasmoids. Strong radiative cooling removes the gas pressure support, allowing the plasmoid cores to contract further.

The right-hand panel of Fig. 6 compares the distributions of mean particle energy $\langle \gamma'' \rangle / \Theta$ measured in the local Landau frames, also extracted from the spacetime diagrams of simulations with $\sigma_0 = 10$. This shows that the distributions are strongly peaked at values that decrease slightly with increasing cooling efficiency from $\langle \gamma'' \rangle_{\text{peak}} \simeq 5.4\Theta$ for the simulation s10Tl to $\langle \gamma'' \rangle_{\text{peak}} \simeq 4.8\Theta$ for the simulation s10Th.

4.5 Individual plasmoids

Figs 7–9 present the histories of individual plasmoids compared for the four simulations listed in Table 1. The plasmoid histories are

compiled from the parameters determined independently for each time-step in automated plasmoid identification algorithm described in Section 3.1. As such, they are subject to some irregularities, in particular, due to shifting positions of the minima of magnetic potential A_z (that define the plasmoid boundaries), especially for large plasmoids merging with the small ones. In order to reduce these irregularities, we chose not to record plasmoid histories in the following circumstances: (1) when there is no gap between two separate plasmoids (i.e. they share the same local A_z minimum) and (2) when the plasmoid layer boundary is less than $100 dx$ from the left/right domain boundary.

We present separately the total plasmoid widths w (dominated by the widths of plasmoid layers) and the widths of their cores w_c , noting that there is no correlation between them. In all simulations,

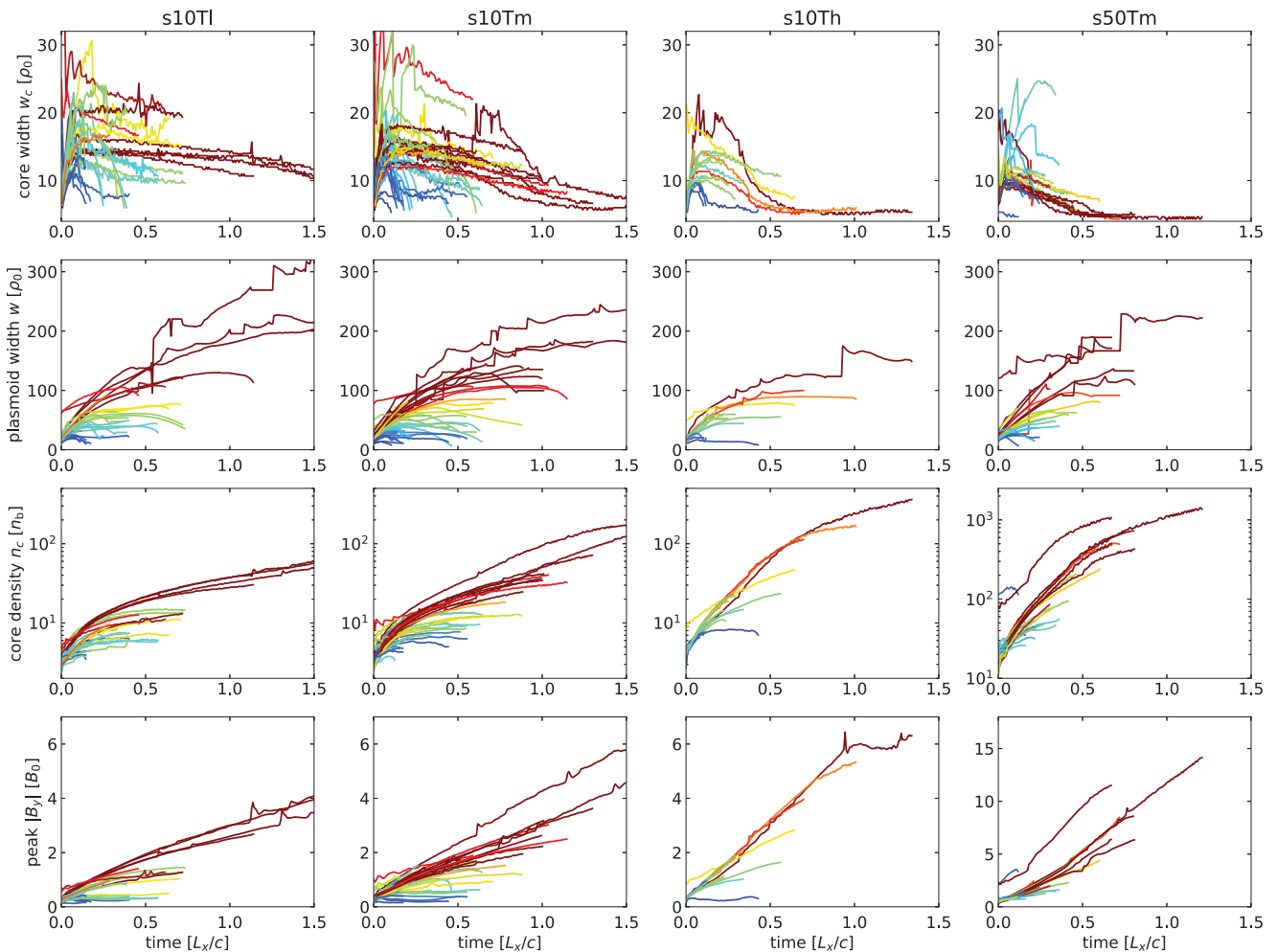


Figure 7. The histories of individual plasmoids compared for the four large simulations. From the top, the rows present: (1) plasmoid core width w_c/ρ_0 ; (2) total plasmoid width w/ρ_0 ; (3) mean core density n_c/n_b ; and (4) peak magnetic field strength $|B_y|/B_0$. For each plasmoid, time is measured relative to its first appearance. The line colour indicates the peak total plasmoid width.

the plasmoid core widths, after a brief formation phase, show a decreasing trend. On the other hand, the total plasmoid widths grow systematically in time for every simulation.

We find that the densities of plasmoid cores n_c grow systematically in time for all simulations. The larger the plasmoid, the denser its core becomes. For simulations with $\sigma_0 = 10$, higher core densities are reached for higher radiative efficiencies. In the case of $\sigma_0 = 50$, the core densities are even higher, roughly in proportion to σ_0 .

The histories of plasmoid core velocities $\beta_{c,x}$ confirm the picture discussed before of small plasmoids being accelerated very rapidly to relativistic velocities and of large plasmoids being accelerated slowly only to mildly relativistic velocities.

The mean particle energies of plasmoid cores, measured in the simulation frame, are somewhat higher for small plasmoids. However, when measured in the Landau frame of the core, they are instead higher for large plasmoids until the radiative cooling effects become significant. The difference is mainly due to relativistic bulk motions of the small plasmoids. In particular, in the simulations $\mathfrak{s}10\text{Tl}$ and $\mathfrak{s}10\text{Tm}$ characterized by weak/moderate cooling, small plasmoids have $\langle\gamma''\rangle_c \simeq 6\Theta$, roughly constant in time, while large plasmoids can reach $\langle\gamma''\rangle_c \simeq 11\Theta$ in the case $\mathfrak{s}10\text{Tl}$. In the simulation $\mathfrak{s}10\text{Th}$ characterized by strong cooling, the intrinsic mean particle energies of the core are reduced down to

$\langle\gamma''\rangle_c \simeq 2\Theta$ by L_x/c . In the simulation $\mathfrak{s}50\text{Tm}$, the cores of large plasmoids are heated up to $\langle\gamma''\rangle_c \simeq 23\Theta$ before cooling down to $\langle\gamma''\rangle_c \lesssim 10\Theta$.

In contrast, the plasmoid layers are characterized by similar and stable intrinsic temperatures $\langle\gamma''\rangle_c \simeq (4 - 6)\Theta$ for all simulations with $\sigma_0 = 10$ (and $\langle\gamma''\rangle_c \sim 15\Theta$ for $\sigma_0 = 50$), showing virtually no signs of radiative cooling.

Most of the plasmoids show their synchrotron emissivity building up in time, both for the core and for the layer. Some of the smaller plasmoids show a very slow decline. The cores of large plasmoids produce significantly more (2–3 orders of magnitude) synchrotron emission per volume element than the cores of small plasmoids and also about 2 orders of magnitude higher emission density than the large plasmoid layers. Our basic finding is that synchrotron emission of the plasmoids is sustained over a long term, irrespective of the cooling efficiency. For the cores of large plasmoids that undergo the most efficient radiative cooling in our high-temperature simulations, it appears that systematically increasing core density, as well as systematically increasing magnetic field strength, is able to offset the reduction in particle mean energy. In the case of $\sigma_0 = 50$, we find a systematic increase of the emission from the cores of large plasmoids to the levels up to $10^7 \mathcal{P}_{\text{syn},b,0}$.

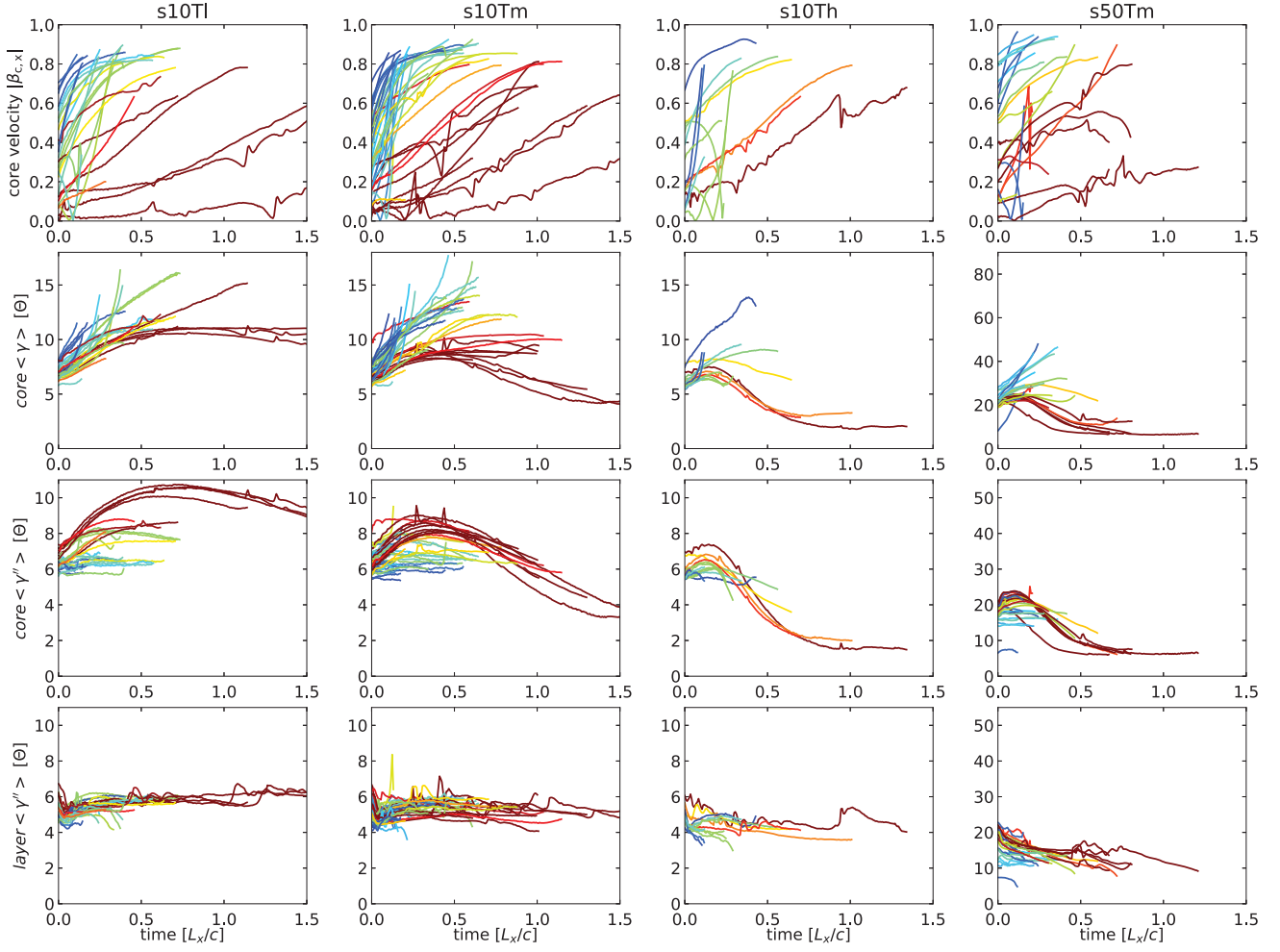


Figure 8. Further histories of individual plasmoids. From the top, the rows present: (1) mean core velocity $|\beta_{c,x}|$; (2) mean particle energy $\langle \gamma \rangle_c / \Theta$ measured in the simulation frame, averaged over the plasmoid core; (3) mean Landau-frame particle energy $\langle \gamma' \rangle_c / \Theta$ of the plasmoid core; and (4) mean Landau-frame particle energy $\langle \gamma' \rangle_l / \Theta$ of the plasmoid layer. See Fig. 7 for more description.

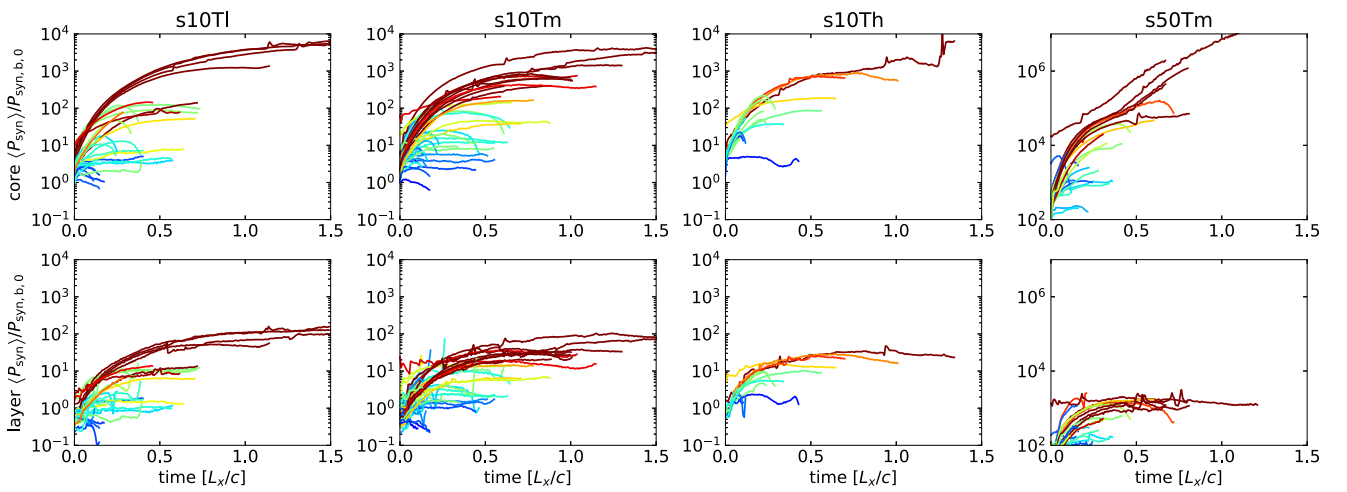


Figure 9. Further histories of individual plasmoids. From the top, the rows present: (1) mean synchrotron emissivity $\langle \mathcal{P}_{\text{syn},c} \rangle / \mathcal{P}_{\text{syn},b,0}$ of the plasmoid core and (2) mean synchrotron emissivity $\langle \mathcal{P}_{\text{syn},l} \rangle / \mathcal{P}_{\text{syn},b,0}$ of the plasmoid layer. See Fig. 7 for more description, and equation (9) for the definition of $\mathcal{P}_{\text{syn},b,0}$.

4.6 Individual particles

Here we describe the behaviour of four selected energetic positrons (denoted as particles #1–#4) for which a detailed history has been recorded. The spacetime tracks of these particles are indicated in Fig. 10. From this, one can see that particles #1 and #2 become trapped in different plasmoids, while particles #3 and #4 become accelerated in the low-density regions between plasmoids.

Fig. 11 presents the detailed acceleration histories of these four particles, all in the same time window. Particle #1 becomes accelerated to Lorentz factor $\gamma \simeq 22\Theta$ in a single episode. The beginning of acceleration episode coincides with the particle becoming trapped in the reconnection midplane ($|y| < 5\rho_0$). We can also see that the acceleration episode coincides with a formation of a new plasmoid that traps the particle also in the x coordinate. The particle experiences mainly the electric field component $E_z \sim 0.1B_0$, and its momentum gain is at first mainly in the z direction, later also in the x direction. After the acceleration episode, the particle oscillates around the plasmoid centre, which results in oscillations of its Lorentz factor γ measured in the simulation frame. However, its Lorentz factor γ' measured in the plasmoid frame shows a slow gradual decline in time, which we attribute to the radiative cooling.

Particle #2 shows a similar behaviour to particle #1; the acceleration episode also coincides with the formation of a new plasmoid. In this case, the acceleration episode is shorter and the energy gain is also lower, with acceleration proceeding in similar electric fields. The radiative cooling is less efficient, and it should be noted that the co-moving perpendicular magnetic field is about twice weaker. At $ct \simeq 2.1L_x$, the plasmoid in which particle #2 is trapped merges into a larger plasmoid on its right side. We see that this results in particle #2 losing most of its energy measured in the simulation frame. It appears that this particle did not experience direct deceleration by strong electric field, instead it just happened to be at its lower energy level in the oscillation cycle at the moment of plasmoids merger. It has also been kicked out from the reconnection midplane, settling briefly at $y \sim 15\rho_0$, trailing behind the merged plasmoid before it exits the right boundary of the domain.

Particle #3 was accelerated in a long acceleration episode under constant electric field $E_z \sim 0.12B_0$ after becoming trapped in the y coordinate to the reconnection midplane. The y and B_x data reveal a typical Speiser orbit with gradually increasing period. The acceleration episode is interrupted at $ct \simeq 2.1L_x$, when the particle begins to interact with a large plasmoid, which forces the particle away from the reconnection midplane. The particle bounces twice off the trailing edge of the plasmoid before it exits the left boundary of the domain. Particle #4 shows another example of Speiser-orbit acceleration in the low-density region of reconnection midplane that is enabled by trapping the particle in the y coordinate.

4.7 Synchrotron emissivity and light curves

Fig. 12 presents the spacetime distribution of the total synchrotron power emitted from the reconnection midplane in all directions for simulation $\mathfrak{s}10\text{Tm}$, and light curves that would be received by two distant observers placed at the opposite sides of the simulation domain, one on the left ($-x$ -axis) and one on the right ($+x$ -axis). While the spacetime diagram of synchrotron power is based on the x -profiles integrated over narrow stripes of $|y| < \delta/2$, the light curves are calculated from a much wider region of $|y| < L_x/2$ to ensure contribution from the whole plasmoids and their broader surroundings.

The synchrotron emission is strongly concentrated along the plasmoid trajectories. As we have noted in Section 4.5, large plasmoids produce significantly more synchrotron emission. The emissivity of the large plasmoid cores exceeds the emissivity of the background plasma by four orders of magnitude.

Light curves received by either observer are completely different, indicating a high level of anisotropy. The most conspicuous features of the light curves are very sharp and bright flares. We can identify the origin of these flares by drawing the corresponding light-cones on the spacetime diagram to the events of small plasmoids approaching the observer with relativistic velocity and merging with a large target plasmoid that is also approaching the observer. Zooming up on these flares, we find their characteristic time-scales of $\tau \sim \rho_0/c$, so they are basically unresolved.⁶ Because of their very short duration, the contribution of these flares to the overall radiation fluence is rather insignificant. The light curves also contain smooth structures characterized by relatively long rise and short decline. These can be attributed to large plasmoids propagating with mildly relativistic velocities, and the sharp declines observed in the light curves coincide with these plasmoids exiting the simulation domain. The contribution of these plasmoids to the light curves is not complete, since their emission is not contained within the simulation boundaries, as we have already noted in Section 4.5.

Comparing the light curves recorded in two frequency bands,⁷ we find that in general the contribution from large plasmoids is higher in the lower frequency band (cyan lines), while the flares produced by small plasmoids are stronger in the higher frequency band (orange lines). Light curves obtained from different simulations are qualitatively very similar, in particular, the level of radiative cooling efficiency does not clearly affect the light-curve characteristics.

4.8 Energy conservation

Because of the use of open boundaries with steady injection of fresh particles, our simulations do not conserve energy globally. In order to evaluate the efficiency of energy transformations, we defined a fixed region \mathcal{R} centred around the reconnection midplane between the left/right absorbing boundary layers, defined by $2\Delta_{\text{abs}} < x < (L_x - 2\Delta_{\text{abs}})$ and $-L_x/4 < y < L_x/4$. In addition to the instantaneous energy contained in \mathcal{R} in the form of magnetic and electric fields, as well as in the particles, we also calculate the cumulative energy emitted by all particles in the synchrotron process and the fluxes of particles and electromagnetic fields (i.e. the Poynting flux) inflowing/outflowing across the \mathcal{R} boundaries.

In Fig. 13, we present the time evolution of different forms of energy contained in the region \mathcal{R} for the simulation $\mathfrak{s}10\text{Tm}$. At the beginning of the simulation, the region \mathcal{R} is dominated by magnetic energy ($\mathcal{E}_{B,0} \simeq 0.6 \mathcal{E}_{\text{tot}}$). The initial ($ct/L_x < 0.6$) energization of particles at the cost of magnetic energy is due to the trigger mechanism. This is followed by the somewhat erratic variation of the particle energy, which reflects systematic heating by magnetic reconnection and episodic escapes of large plasmoids. Over the course of the simulation ($ct/L_x \simeq 4.5$), the magnetic energy of the region \mathcal{R} decreases by $\simeq 40$ per cent, while the particle energy decreases only by about $\simeq 15$ per cent. At the same time, we measure a large net influx of electromagnetic energy (accumulating to $\simeq 1.5 \mathcal{E}_{B,0}$),

⁶Contributions to every light curve are recorded at every simulation time-step at the temporal resolution of dt .

⁷The light curves are presented in the same arbitrary units equivalent to the νF_ν flux density.

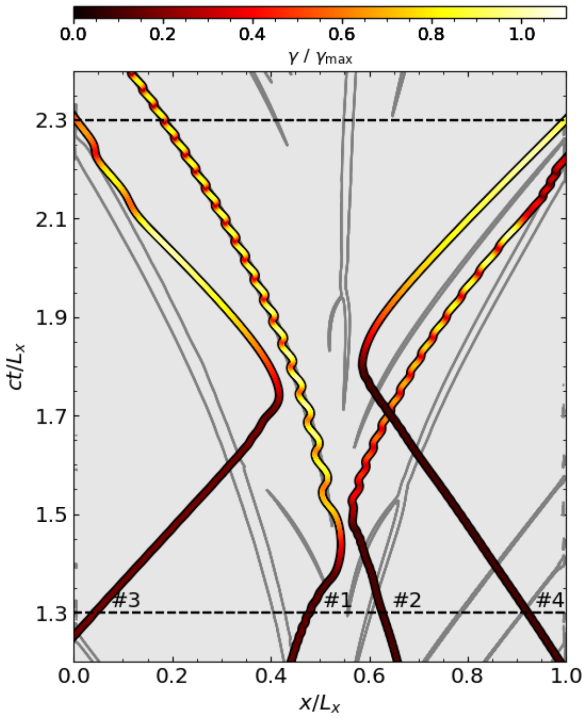


Figure 10. Spacetime diagram of the tracks of selected energetic particles, the acceleration of which is characterized in detail in Fig. 11. The line colour indicates the instantaneous particle energy measured in the simulation frame. Particle density contours $n = 7n_b$ are indicated with grey lines.

mainly through the top/bottom boundaries of the region \mathcal{R} , and even larger net outflow of particle energy, mainly through the left/right boundaries. The net energy outflow (particle minus electromagnetic) through the region boundaries amounts to $\simeq 0.25 \mathcal{E}_{B,0}$ of the initial magnetic energy, which is slightly less than the particle energy lost to the synchrotron radiation ($\simeq 0.3 \mathcal{E}_{B,0}$). Accounting for all these energy components and flows, the total energy in \mathcal{R} is conserved at the ~ 0.1 per cent level.

4.9 Energy distributions of particles and photons

Fig. 14 shows the energy distributions of all particles: electrons and positrons. For each simulation, it is averaged over a period of time that excludes only the initial stage ($ct/L \lesssim 0.85$). In all studied cases, the particle energy distributions established after the initial period show no significant evolution in time. As energetic particles escape across the open left/right boundaries, other particles are energized across the current layer and are subject to radiative energy losses within the plasmoids. The balance between these processes is maintained regardless of the efficiency of radiative cooling. In all studied cases, a small fraction of particles reach energies of $\gamma_{\text{cutoff}} = 4\sigma_0\Theta$ established as a cutoff energy in a previous study of non-radiative Harris-layer reconnection within periodic boundaries (Werner et al. 2016). In the case of $\sigma_0 = 10$, we find only a minor effect of radiative cooling in limiting the high-energy excess for $\Theta \gtrsim 10^6$. In the case of $\sigma_0 = 50$, the high-energy component can be described as a broken power law with a hard slope of $p_1 \simeq 1.5$ extending up to $\gamma \simeq 25\Theta$ and a soft tail of $p_2 \simeq 3.6$ extending up to $\gamma \simeq 150\Theta$. In that case, we also have $\gamma_{\text{cutoff}} \simeq \gamma_{\text{rad}}$.

Fig. 15 shows the spectral energy distributions (SED) νF_ν of the synchrotron emission produced by all particles in all directions,

averaged over the same periods of time as the particle energy distributions presented in Fig. 14. In the case of $\sigma_0 = 10$, the SED are dominated by the contribution from low-energy particles peaking around $\nu \simeq 19\nu_{\text{syn}0}$, with a high-frequency excess extending beyond a characteristic value of $\nu_{\text{cutoff}} \simeq 19\sigma_0^2\nu_{\text{syn}0}$. The level of this high-frequency excess increases with decreasing gas temperature Θ , which means that radiative cooling suppresses the high-frequency radiation component more clearly than it affects the high-energy particle tail. In the case of $\sigma_0 = 50$, the SED is strongly dominated by the contribution from energetic particles with the maximum photon energies consistent with a cutoff at $\nu_{\text{cutoff}} \simeq 19\sigma_0^2\nu_{\text{syn}0}$, which coincides with the radiation reaction limit $\nu_{\text{syn,max}} = (\gamma_{\text{rad}}/\Theta)^2\nu_{\text{syn}0}$. We note that the SED shape around its peak is not described by a broken power law corresponding directly to that indicated in the electron distribution (with slopes $\nu F_\nu \propto \nu^{-s}$; $s = (p - 3)/2$; and characteristic frequencies $\nu_i/\nu_{\text{syn}0} \simeq (\gamma_i/\Theta)^2$). This is because the extent of the electron energy distribution that can be described as a broken power law is too short to result in a broken power-law photon spectrum when folded with the synchrotron kernel.

In order to clarify the connection between the electron energy distribution and synchrotron SED in the case of $\sigma_0 = 50$, we analysed a sample of individually tracked particles. We selected particles over two energy ranges: (1) a medium-energy range $11 < \gamma/\Theta < 22$, corresponding to the hard power-law section of index $p_1 \simeq 1.5$; and (2) a high-energy range $50 < \gamma/\Theta < 150$, corresponding to the soft power-law section of index $p_2 \simeq 3.6$. In Fig. 16, we show the distributions of these particles along coordinate x and over local magnetic field strength B , as well as their contributions to the synchrotron SED, taking into account accurate local electromagnetic fields felt by each particle. These distributions are averaged over multiple simulation time-steps for $ct/L_x > 0.85$. For the medium-energy particles, we find that their distribution along x is fairly uniform, and their distribution over B is broad, with some particles found in strongly amplified magnetic field $B > 10B_0$ characteristic for the plasmoid cores. For the high-energy particles, we find that they are clearly concentrated towards the left/right boundaries, and that they are found almost exclusively in magnetic fields of moderate strength $B < 5B_0$. In addition, we observe that for individual simulation time-steps, the medium-energy particles are clearly concentrated within the plasmoids, while the high-energy particles are diffused over x . The medium-energy particles dominate the synchrotron SED for most frequencies, except the highest values of $\nu > 5 \times 10^4\nu_{\text{syn}0}$. At low frequencies, the relative contribution of the medium-energy particles is $\simeq 60$ times higher than that of the high-energy ones.

5 DISCUSSION

Our results are consistent with the basic picture of steady-state relativistic plasmoid reconnection that has been established since the work of Sironi et al. (2016). The open boundaries allow to evacuate the reconnected plasma and develop unimpeded reconnection outflows that reach relativistic bulk velocities of the order of the background Alfvén velocity. In the centrally positioned active magnetic X-point, plasmoids are generated spontaneously over a wide range of sizes. The smallest discernible plasmoids, with the width of order $\sim 20\rho_0$ (deep blue lines in Figs 7–9), are rapidly accelerated to relativistic speeds and their lifetimes are about $\sim 0.2L_x/c$. The largest plasmoids, with the width of order $\sim (150–200)\rho_0$ (brown lines in Figs 7–9) accelerate slowly, reaching mildly relativistic speeds $\sim c/2$ only after $\sim 1.5L_x/c$. This is a confirmation of the anticorrelation between growth and acceleration of plasmoids identified by Sironi et al. (2016).

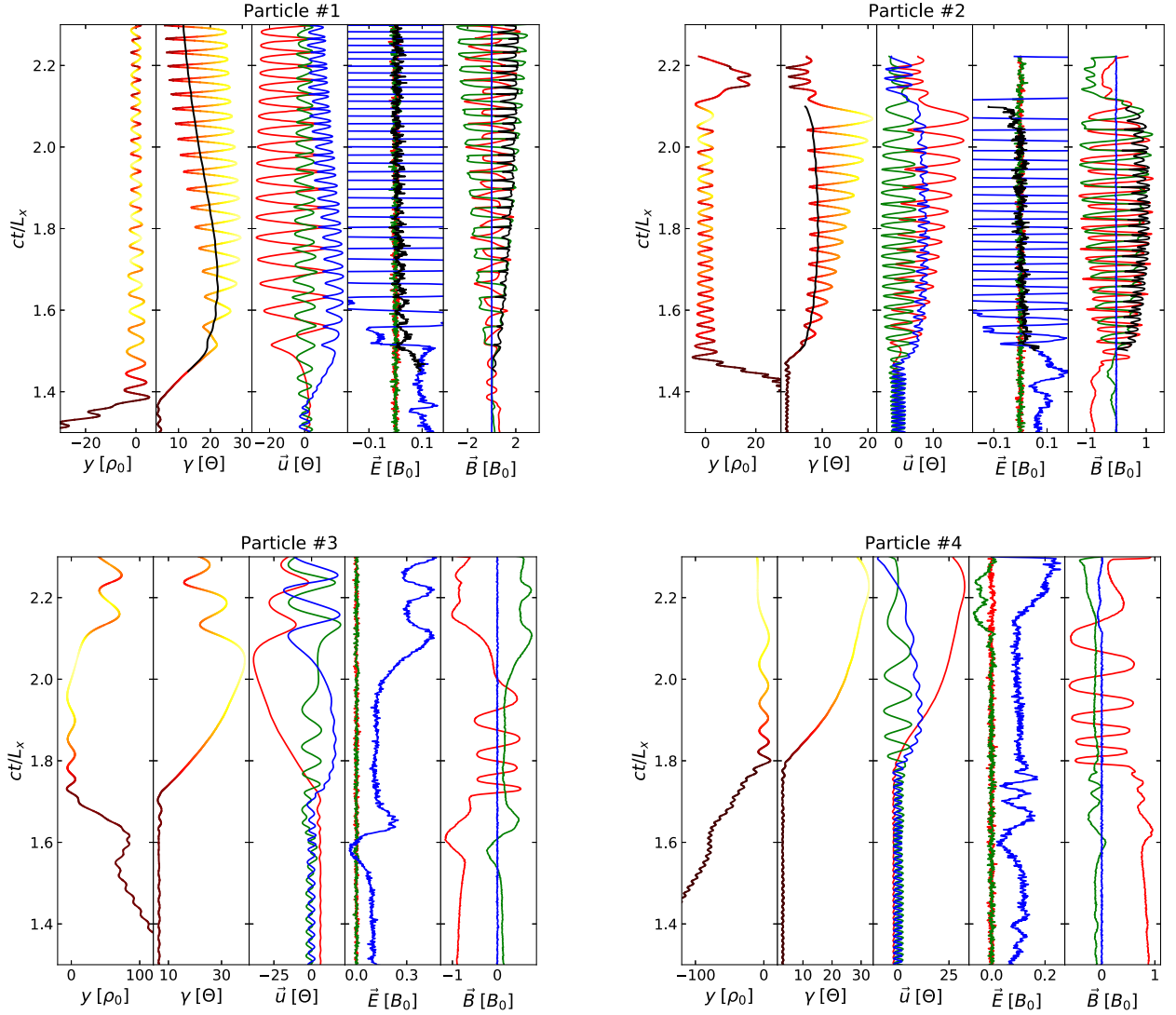


Figure 11. Acceleration histories for selected energetic particles, the x -positions of which are shown in Fig. 10. For each particle, we present detailed information as functions of simulation time on five panels, from the left: (1) the y -position measured from the reconnection midplane, (2) particle Lorentz factor γ (also indicated with a colour scale on panels 1 and 2) normalized to Θ , (3) three components of the particle 4-velocity \mathbf{u} (x – red, y – green, and z – blue) normalized to Θ , (4) three components of the local electric field \mathbf{E} in units of B_0 , and (5) three components of the local magnetic field \mathbf{B} in units of B_0 . For particles #1 and #2, the black lines indicate parameter values (Lorentz factor γ' , electric field E'_\parallel , and magnetic field B'_\perp) measured in the co-moving frame of a plasmoid to which the particle is attached.

An important consequence of the relation between plasmoid sizes and their acceleration length scale is that it is not possible to contain the bulk acceleration of large plasmoids within a domain with open boundaries. We have found that as we increase the size of the simulation domain, given proportionally more simulation time, we obtain ever larger plasmoids that require ever more acceleration time. In other words, we are unable to isolate the bulk acceleration of plasmoids from the domain boundaries and obtain a coasting phase of uniformly Alfvénic reconnection outflows.

A similar problem applies to the production of synchrotron light curves. In our simulations, even for the highest plasma temperatures investigated, we were not able to contain synchrotron emission from the largest plasmoids within the domain boundaries. As we show in Figs 8 and 9, even though in the case of short cooling length $l_{\text{cool}} \ll L_x$, the plasmoid cores indeed undergo efficient radiative cooling within the L_x/c time-scale, the total synchrotron emission of plasmoid cores and layers is not decreasing significantly.

The nominal cooling time-scale cannot be reduced indefinitely by a further increase of the particle distribution temperature. We found that, with unrestricted radiation reaction, already for $\Theta = 1.25 \times 10^6$, the particle densities in the cores of the largest plasmoids increase to the level at which the Debye length eventually becomes unresolved $\lambda_D = (\Theta m_e c^2 / 4\pi n e^2)^{1/2} < dx$, which leads to the development of numerical electrostatic instabilities. Our ad hoc restriction of radiation reaction [see a footnote preceding equation (5)] helps to avoid developing these instabilities. We note that a similar restriction of radiation physics (pair creation) in the plasmoid cores has been applied by Hakobyan et al. (2019).

Christie et al. (2019a) calculated light curves of synchrotron and inverse Compton emission by post-processing the results of non-radiative PIC simulations of relativistic steady-state reconnection of Sironi et al. (2016). Their radiation transfer model is based on several assumptions that can be verified by the results of our radiative PIC simulations. One of their key assumptions is that the intrinsic

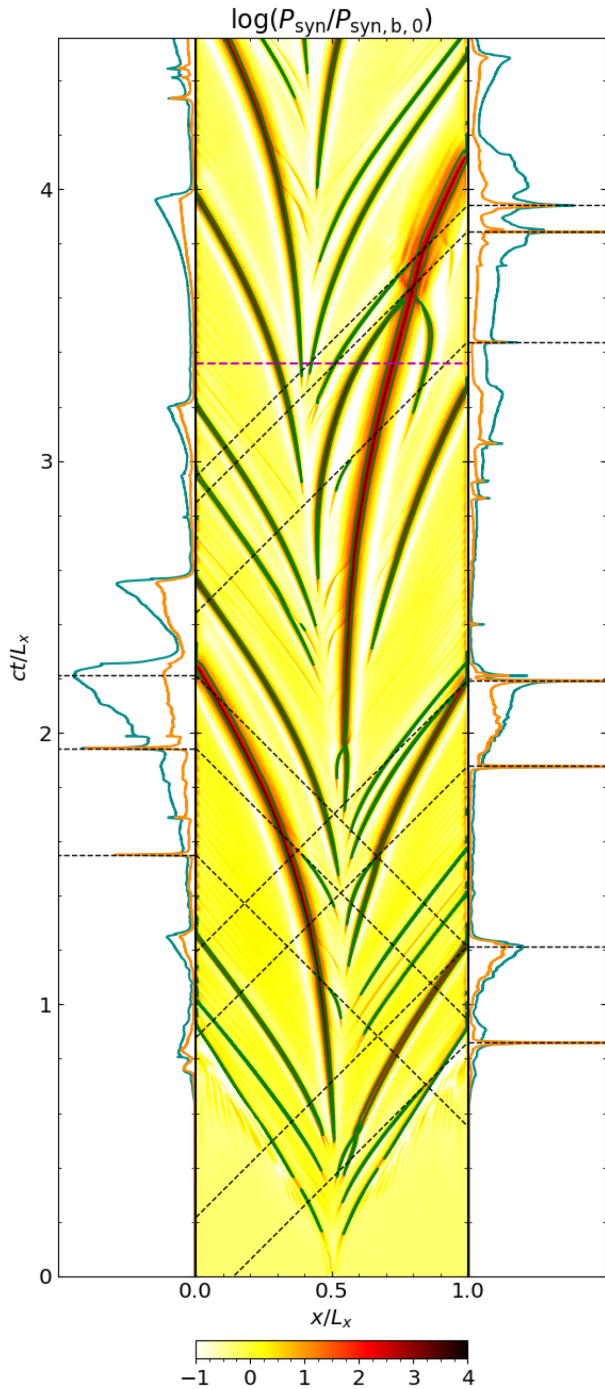


Figure 12. The left-hand and right-hand panels show synchrotron light curves measured by observers placed at left and right sides of the reconnecting layer, respectively. The cyan and orange lines correspond to the two selected frequency bands indicated in Fig. 15. The middle panel shows the spacetime distribution of total synchrotron power normalized to the value $\mathcal{P}_{\text{syn},b,0}$ defined in equation (9). The particle number density contours $n = 7n_b$ are shown with green solid lines. The black dashed lines represent the light-cones corresponding to selected features in either light curve. The magenta dashed line indicates the simulation time $ct = 3.36L_x$ corresponding to the simulation state shown in Figs 1 and 3.

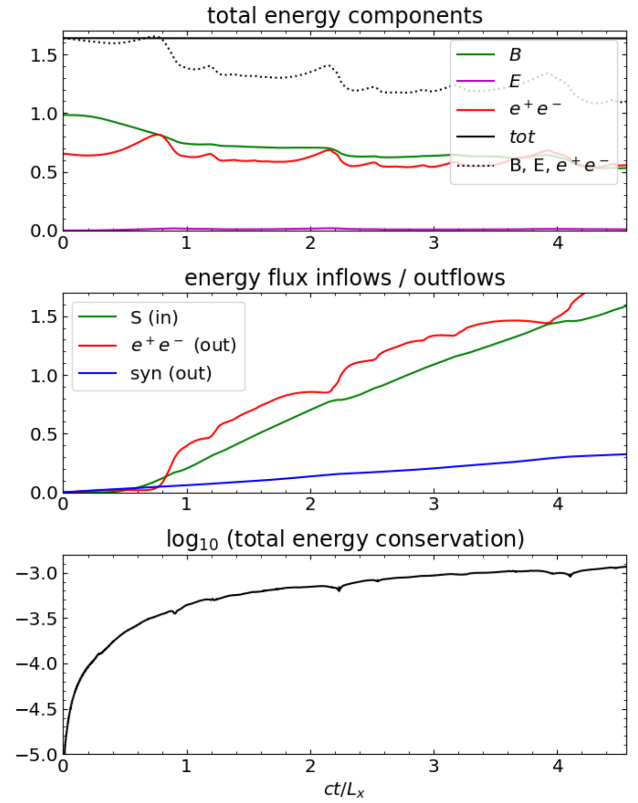


Figure 13. Top panel: mean energy densities, normalized to initial magnetic energy density $U_{B,0}$, calculated for the analysis region \mathcal{R} , defined by $2\Delta_{\text{abs}} < x < L_x - 2\Delta_{\text{abs}}$ and $-L_x/4 < y < L_x/4$, for the simulation $s10Tm$. We plot the contributions from magnetic fields (green), electric fields (magenta), all particles (e^+ and e^- ; red), and total conserved energy including inflows and outflows (black). The black dotted line shows the total instantaneous energy contained in \mathcal{R} , including contributions from the magnetic and electric fields, and all particles. Middle panel: energy flux inflows and outflows: the inflowing Poynting flux (green), outflowing particle energy flux (red), and total synchrotron emission (blue). Bottom panel: conservation of the total energy of region \mathcal{R} , including inflows and outflows.

structure of plasmoids is not important and can be approximated by using their average parameters that in addition are constant in time. Our results suggest that the synchrotron emissivity is strongly concentrated in the central parts of the plasmoids (see the bottom panel of Fig. 3), and that in the radiatively efficient regime, the plasmoid cores undergo significant time evolution with systematic increase of plasmoid core density and peak magnetic field strength (Fig. 7). We suggest that small plasmoids and the cores of large plasmoids are important for understanding the production of rapid radiation flares. Investigation of these structures is also the most challenging from the numerical perspective.

Our study suggests that properly resolving the cores of large plasmoids will be critical for understanding the radiative signatures of plasmoid reconnection. Recent non-radiative PIC simulations of relativistic reconnection demonstrated an important role of large plasmoids in extending the high-energy tail of the particle energy distribution along a power law of slope $\simeq 2$ (Petropoulou & Sironi 2018). However, taking into account radiative cooling, which is expected to be particularly strong in the plasmoid cores, the maximum energy achievable in the plasmoids may be significantly limited.

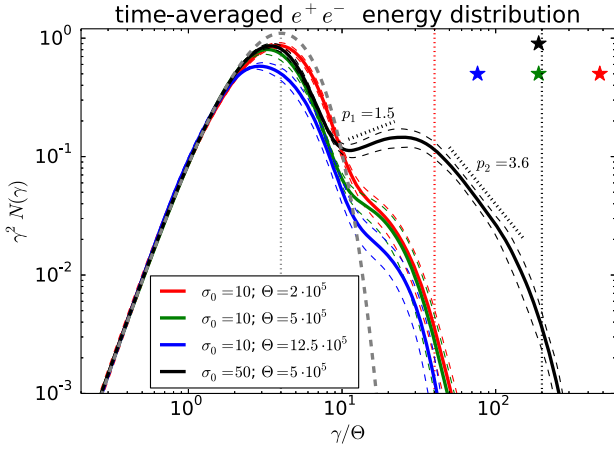


Figure 14. Energy distributions of all particles contained in the simulation domain, compared for the four main simulations (higher Θ corresponds to more efficient cooling). For each simulation, the distribution is averaged over simulation time, excluding the initial stage ($ct/L \lesssim 0.85$), in the space of flux logarithm. The thin dashed lines indicate the corresponding standard deviation values. The thick grey dashed line represents the initial Maxwell–Jüttner distribution for $\Theta \gg 1$. The distributions are presented in arbitrary units and they are normalized to match the low-energy sections. The vertical dotted lines indicate the characteristic values of γ/Θ : 4 (the $\gamma^2 N(\gamma)$ peak for the initial background particles; grey), 4×10 (red), and 4×50 (black). The oblique black dotted lines indicate two power-law slopes p ($N(\gamma) \propto \gamma^{-p}$) along the $\sigma_0 = 50$ distribution. The four stars indicate the values of $\gamma_{\text{rad}}/\Theta$ for each simulation.

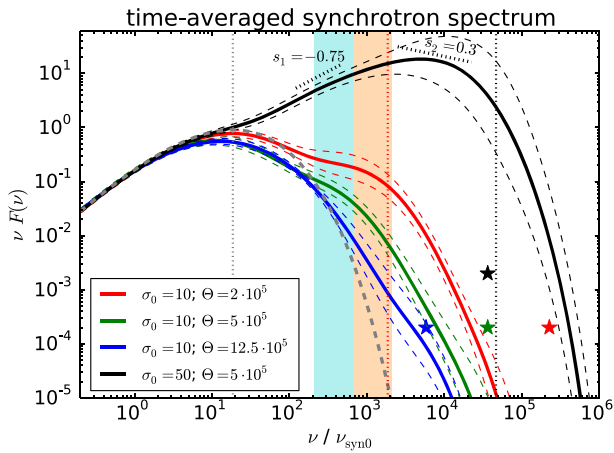


Figure 15. Isotropic spectra of the synchrotron radiation emitted across the simulation domain, compared for the four main simulations. For each simulation, the distribution is averaged over simulation time, excluding the initial stage ($ct/L \lesssim 0.85$), in the space of flux logarithm. The thin dashed lines indicate the corresponding standard deviation values. The thick grey dashed line represents the synchrotron spectrum of the initial Maxwell–Jüttner distribution. The frequencies are normalized to the characteristic synchrotron frequency $\nu_{\text{syn}0}$ defined in equation (11). The distributions are presented in arbitrary units and they are normalized to match the low-frequency sections. The vertical dotted lines indicate the characteristic values of $\nu/\nu_{\text{syn}0}$: 19 (the $\nu F(\nu)$ peak for the initial background particles; grey), 19×10^2 (red), and 19×50^2 (black). The oblique black dotted lines indicate two power-law slopes $s = (3 - p)/2$ ($\nu F(\nu) \propto \nu^{-s}$) that would be expected for the corresponding power laws p_1, p_2 marked in Fig. 14. The four stars indicate the values of MHD synchrotron frequency limit $\nu_{\text{syn, max}}/\nu_{\text{syn}0} = (\gamma_{\text{rad}}/\Theta)^2$ for each simulation. The cyan and orange stripes indicate the frequency bands from which the light curves shown in Fig. 12 were extracted.

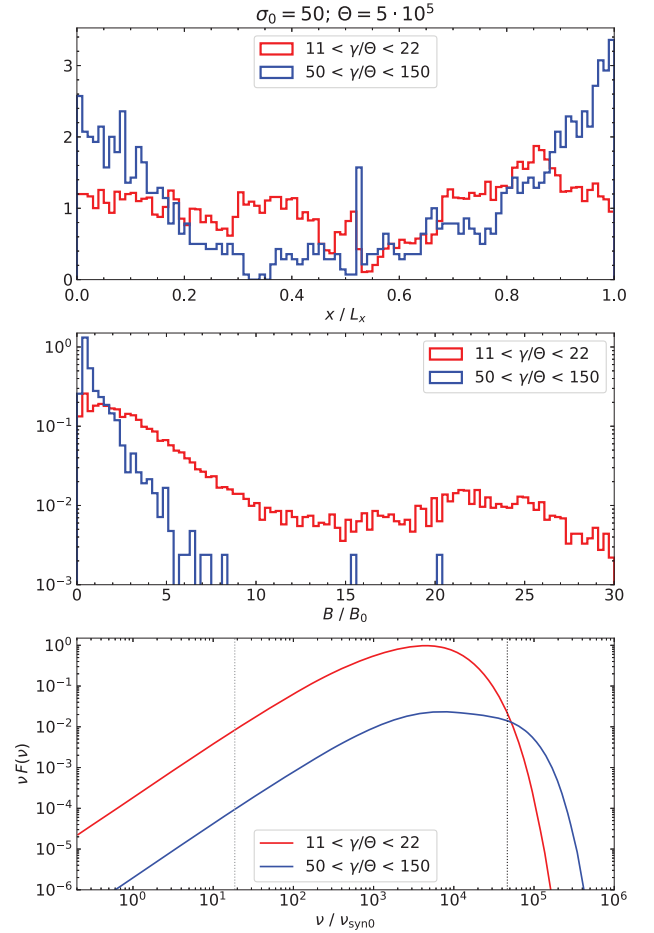


Figure 16. Analysis of individual tracked particles for the simulation $s50\text{Tm}$. Particles are selected over two energy ranges – $11 < \gamma/\Theta < 22$ (red) and $50 < \gamma/\Theta < 150$ (blue) – corresponding to the two power-law sections indicated in Fig. 14. The top panel compares their normalized distributions along coordinate x ; the middle panel compares their normalized distributions over magnetic field strength B ; and the bottom panel compares their contributions to the isotropic synchrotron SED (arbitrary units). The distributions are averaged over multiple simulation time-steps for $ct/L_x > 0.85$. The vertical dotted lines in the bottom panel correspond to those in Fig. 15.

Plasmoid mergers have been suggested previously to be important for particle acceleration in relativistic reconnection, based on the results of relatively modest PIC simulations of reconnection in periodic boundaries (Nalewajko et al. 2015). Subsequent numerical studies emphasized a more fundamental role of magnetic X-points as a crucial first step for particles that eventually achieve the highest energies (Ball, Sironi & Özel 2019; Guo et al. 2019). Here, we would like to point out that even if plasmoid mergers may not dominate particle acceleration in non-radiative reconnection, they are important for the production of transient radiation signals. Even if major head-on collisions of large plasmoids are rare events, tail-on collisions of unequal plasmoids, arguably more frequent events due to the growth–acceleration anticorrelation, can be responsible for most of the sharpest features observed in the resulting light curves. Recent results of Christie et al. (2020) show that large plasmoids can attract many small plasmoids originating on both sides of their trajectory, enhancing the rates of both tail-on and head-on mergers.

Our results also demonstrate the co-existence of plasmoids and minijets in the same reconnection layer. We find minijets persisting in the gaps forming between plasmoids, plasmoids are able to slide along a minijet without causing much disturbance, and a minijet reforms behind a passing plasmoid. The structure of minijets found in our simulations is qualitatively very similar to the analytical model of Lyubarsky (2005). Although the minijets contain some highly energetic particles, their contribution to the observed radiative signatures appears to be very weak. There may be two reasons behind this: (1) the minijets are characterized by much lower particle density than the plasmoids and (2) energetic particles propagating along the minijets show only weak radiative energy losses due to weak perpendicular magnetic field component.⁸

In the high-magnetization case of $\sigma_0 = 50$, we found that the particle energy distribution is maintained in the form of a broken power law with a hard power-law slope $p_1 \simeq 1.5$ breaking around $\gamma \simeq 25\Theta$ into a soft power-law slope $p_2 \simeq 3.6$. The hard power-law slope is consistent with the results of PIC simulations of non-radiative highly relativistic Harris-layer reconnection in periodic boundaries (Guo et al. 2014; Sironi & Spitkovsky 2014; Werner et al. 2016). The soft power-law slope is reminiscent of that seen in the recent PIC simulations of relativistic reconnection with strong inverse-Compton cooling, both in periodic boundaries (Werner, Philippov & Uzdensky 2019) and in the open ones (Sironi & Beloborodov 2019). In the latter work, the electron energy distribution has been decomposed into contributions from particles accelerated at different sites, which suggests that the soft power law arises from a combined action of primary X-points of the main reconnection layer, secondary X-points formed by merging plasmoids, and unstructured outflows (the minijets). This is consistent with our analysis of the distribution of individual tracked particles belonging to the energy range of $50 < \gamma/\Theta < 150$. We found that these particles are strongly concentrated towards the boundaries and are found exclusively outside the plasmoid cores at normal magnetic field strengths $B < 5B_0$. Typical examples of such particles are Particles #3 and #4 presented in Figs 10 and 11. Low relative numbers and diffuse spatial distribution imply that these particles are not important to the overall synchrotron SED (except for the very highest frequencies), nor to the production of rapid radiation flares.

6 CONCLUSIONS

We presented the results of the first kinetic simulations of RMR within open boundaries that enable steady-state plasmoid reconnection and including the synchrotron radiation reaction. We confirm the general picture of steady-state relativistic plasmoid reconnection established by Sironi et al. (2016) and subsequent works. We find that synchrotron emission of plasmoids cannot be contained within open boundaries. The cores of large plasmoids are the main sites of synchrotron emission and their particle densities are significantly enhanced due to radiative pressure losses. Rapid flares of synchrotron radiation can be produced by tail-on mergers between small/fast plasmoids with large/slow targets. The plasmoids are also found to co-exist with the minijets that do not produce a lot of radiation due to their low particle densities. In the high-magnetization case ($\sigma_0 = 50$), the energy distribution of accelerated particles can be described as a broken power law with a hard medium-energy section produced

mainly by particles accelerated in the plasmoids and a soft high-energy tail produced by diffuse particles accelerated in the minijets.

ACKNOWLEDGEMENTS

We thank the reviewer for helpful comments. We acknowledge discussions with Benoît Cerutti, Dimitrios Giannios, and Maria Petropoulou. The original version of the `Zeltron` code was created by Benoît Cerutti and co-developed by Gregory Werner at the University of Colorado Boulder (<http://benoit.cerutti.free.fr/Zeltron/>). These results are based on numerical simulations performed at the supercomputer *Prometheus* located at Cyfronet AGH, Poland (PLGrid grant rcjose18; PI: K. Nalewajko). This work was supported by the Polish National Science Centre grant 2015/18/E/ST9/00580.

DATA AVAILABILITY

The data underlying this article will be shared on reasonable request to the corresponding author.

REFERENCES

- Aharonian F. et al., 2007, *ApJ*, 664, L71
 Aharonian F. et al., 2009, *ApJ*, 696, L150
 Ahnen M. L. et al., 2016, *A&A*, 593, A91
 Albert J. et al., 2007, *ApJ*, 669, 862
 Alves E. P., Zrake J., Fiuza F., 2018, *Phys. Rev. Lett.*, 121, 245101
 Ball D., Sironi L., Özel F., 2019, *ApJ*, 884, 57
 Begelman M. C., 1998, *ApJ*, 493, 291
 Begelman M. C., Fabian A. C., Rees M. J., 2008, *MNRAS*, 384, L19
 Blandford R. D., Znajek R. L., 1977, *MNRAS*, 179, 433
 Böttcher M., Reimer A., Sweeney K., Prakash A., 2013, *ApJ*, 768, 54
 Bromberg O., Singh C. B., Davelaar J., Philippov A. A., 2019, *ApJ*, 884, 39
 Buehler R. et al., 2012, *ApJ*, 749, 26
 Cerutti B., Werner G. R., Uzdensky D. A., Begelman M. C., 2013, *ApJ*, 770, 147
 Cerutti B., Werner G. R., Uzdensky D. A., Begelman M. C., 2014, *ApJ*, 782, 104
 Chiaberge M., Ghisellini G., 1999, *MNRAS*, 306, 551
 Christie I. M., Petropoulou M., Sironi L., Giannios D., 2019, *MNRAS*, 482, 65
 Christie I. M., Petropoulou M., Sironi L., Giannios D., 2020, *MNRAS*, 492, 549
 Crusius A., Schlickeiser R., 1986, *A&A*, 164, L16
 Daughton W., Karimabadi H., 2007, *Phys. Plasmas*, 14, 072303
 Daughton W., Scudder J., Karimabadi H., 2006, *Phys. Plasmas*, 13, 072101
 Fossati G., Maraschi L., Celotti A., Comastri A., Ghisellini G., 1998, *MNRAS*, 299, 433
 Ghisellini G., Righi C., Costamante L., Tavecchio F., 2017, *MNRAS*, 469, 255
 Giannios D., 2013, *MNRAS*, 431, 355
 Giannios D., Spruit H. C., 2006, *A&A*, 450, 887
 Giannios D., Uzdensky D. A., 2019, *MNRAS*, 484, 1378
 Giannios D., Uzdensky D. A., Begelman M. C., 2009, *MNRAS*, 395, L29
 Goyal A. et al., 2017, *ApJ*, 837, 127
 Guo F., Li H., Daughton W., Liu Y.-H., 2014, *PhRvL*, 113, 155005
 Guo F., Li X., Daughton W., Kilian P., Li H., Liu Y.-H., Yan W., Ma D., 2019, *ApJ*, 879, L23
 Hakobyan H., Philippov A., Spitkovsky A., 2019, *ApJ*, 877, 53
 Katarzyński K., Lenain J.-P., Zech A., Boisson C., Sol H., 2008, *MNRAS*, 390, 371
 Kirk J. G., Skjæraasen O., 2003, *ApJ*, 591, 366
 Kirk J. G., Rieger F. M., Mastichiadis A., 1998, *A&A*, 333, 452
 Komissarov S. S., Barkov M. V., Vlahakis N., Königl A., 2007, *MNRAS*, 380, 51
 Levinson A., 2007, *ApJ*, 671, L29

⁸Radiative cooling in the minijets might be stronger if the guide field component B_z were included.

- Li Z.-Y., Chiueh T., Begelman M. C., 1992, *ApJ*, 394, 459
- Loureiro N. F., Schekochihin A. A., Cowley S. C., 2007, *Phys. Plasmas*, 14, 100703
- Lovelace R. V. E., Newman W. I., Romanova M. M., 1997, *ApJ*, 484, 628
- Lyubarsky Y. E., 2005, *MNRAS*, 358, 113
- Lyutikov M., Uzdensky D., 2003, *ApJ*, 589, 893
- Madejski G., Sikora M., 2016, *ARA&A*, 54, 725
- Meyer M., Scargle J. D., Blandford R. D., 2019, *ApJ*, 877, 39
- Morris P. J., Potter W. J., Cotter G., 2019, *MNRAS*, 486, 1548
- Nalewajko K., 2018, *MNRAS*, 481, 4342
- Nalewajko K., Giannios D., Begelman M. C., Uzdensky D. A., Sikora M., 2011, *MNRAS*, 413, 333
- Nalewajko K., Uzdensky D. A., Cerutti B., Werner G. R., Begelman M. C., 2015, *ApJ*, 815, 101
- Nalewajko K., Yuan Y., Chruślińska M., 2018, *JPLPh*, 84, 755840301
- Parker E. N., 1957, *J. Geophys. Res.*, 62, 509
- Petropoulou M., Sironi L., 2018, *MNRAS*, 481, 5687
- Petropoulou M., Giannios D., Sironi L., 2016, *MNRAS*, 462, 3325
- Petropoulou M., Christie I. M., Sironi L., Giannios D., 2018, *MNRAS*, 475, 3797
- Petschek H. E., 1964, *NASA Spec. Publ.*, 50, 425
- Piran T., 2004, *Rev. Mod. Phys.*, 76, 1143
- Schoeffler K. M., Grismayer T., Uzdensky D., Fonseca R. A., Silva L. O., 2019, *ApJ*, 870, 49
- Sikora M., Stawarz Ł., Moderski R., Nalewajko K., Madejski G. M., 2009, *ApJ*, 704, 38
- Sironi L., Beloborodov A. M., 2019, preprint ([arXiv:1908.08138](https://arxiv.org/abs/1908.08138))
- Sironi L., Spitkovsky A., 2014, *ApJ*, 783, L21
- Sironi L., Petropoulou M., Giannios D., 2015, *MNRAS*, 450, 183
- Sironi L., Giannios D., Petropoulou M., 2016, *MNRAS*, 462, 48
- Sweet P. A., 1958, *Electromagn. Phenom. Cosmical Phys.*, p. 123
- Urry C. M., Padovani P., 1995, *PASP*, 107, 803
- Uzdensky D. A., Loureiro N. F., Schekochihin A. A., 2010, *Phys. Rev. Lett.*, 105, 235002
- Werner G. R., Uzdensky D. A., Cerutti B., Nalewajko K., Begelman M. C., 2016, *ApJ*, 816, L8
- Werner G. R., Uzdensky D. A., Begelman M. C., Cerutti B., Nalewajko K., 2018, *MNRAS*, 473, 4840
- Werner G. R., Philippov A. A., Uzdensky D. A., 2019, *MNRAS*, 482, L60
- Zenitani S., Hoshino M., 2001, *ApJ*, 562, L63
- Zweibel E. G., Yamada M., 2009, *ARA&A*, 47, 291

This paper has been typeset from a $\text{\TeX}/\text{\LaTeX}$ file prepared by the author.

Chapter 3

Paper 2: Kinetic simulations of instabilities and particle acceleration in cylindrical magnetized relativistic jets



Kinetic Simulations of Instabilities and Particle Acceleration in Cylindrical Magnetized Relativistic Jets

José Ortuño-Macías¹, Krzysztof Nalewajko¹, Dmitri A. Uzdensky², Mitchell C. Begelman^{3,4}, Gregory R. Werner², Alexander Y. Chen³, and Bhupendra Mishra⁵

¹Nicolaus Copernicus Astronomical Center, Polish Academy of Sciences, Bartycka 18, 00-716 Warsaw, Poland; jortuno@camk.edu.pl, knalew@camk.edu.pl

²Center for Integrated Plasma Studies, Department of Physics, University of Colorado, 390 UCB, Boulder, CO 80309-0390, USA

³JILA, University of Colorado and National Institute of Standards and Technology, 440 UCB, Boulder, CO 80309-0440, USA

⁴Department of Astrophysical and Planetary Sciences, University of Colorado, 391 UCB, Boulder, CO 80309, USA

⁵Los Alamos National Laboratory, Los Alamos, NM 87545, USA

Received 2022 February 9; revised 2022 April 12; accepted 2022 April 25; published 2022 June 3

Abstract

Relativistic magnetized jets, such as those from AGN, GRBs, and XRBs, are susceptible to current- and pressure-driven MHD instabilities that can lead to particle acceleration and nonthermal radiation. Here, we investigate the development of these instabilities through 3D kinetic simulations of cylindrically symmetric equilibria involving toroidal magnetic fields with electron–positron pair plasma. Generalizing recent treatments by Alves et al. and Davelaar et al., we consider a range of initial structures in which the force due to toroidal magnetic field is balanced by a combination of forces due to axial magnetic field and gas pressure. We argue that the particle energy limit identified by Alves et al. is due to the finite duration of the fast magnetic dissipation phase. We find a rather minor role of electric fields parallel to the local magnetic fields in particle acceleration. In all investigated cases, a kink mode arises in the central core region with a growth timescale consistent with the predictions of linearized MHD models. In the case of a gas-pressure-balanced (Z-pinch) profile, we identify a weak local pinch mode well outside the jet core. We argue that pressure-driven modes are important for relativistic jets, in regions where sufficient gas pressure is produced by other dissipation mechanisms.

Unified Astronomy Thesaurus concepts: [High energy astrophysics \(739\)](#); [Jets \(870\)](#)

1. Introduction

Magnetic fields are thought to play a decisive role in many of the most energetic astrophysical phenomena. Compact accreting objects tend to accumulate (or generate locally) magnetic fields and sort them out from the matter (e.g., Narayan et al. 2003). This can produce extreme environments in which the magnetic energy density locally dominates the rest-mass density of matter. Such relativistic magnetizations can be converted to high Lorentz factors, driving relativistic outflows in the form of collimated jets (e.g., Begelman et al. 1984; Li et al. 1992; Begelman & Li 1994; Beskin & Nokhrina 2006; Komissarov et al. 2007; Tchekhovskoy et al. 2009). Luminous nonthermal emission with photon energies extending into the gamma-ray band is a key observational signature of such environments (e.g., Tavani et al. 2011; Abdo et al. 2011; Madejski & Sikora 2016); it is evidence of efficient nonthermal acceleration of particles to ultrarelativistic energies. A likely mechanism for particle acceleration in such environments is relativistic magnetic reconnection (e.g., Michel 1971; Romanova & Lovelace 1992; Lyubarskii 1996; Drenkhahn & Spruit 2002; Kirk 2004; Uzdensky et al. 2011; Sironi et al. 2015; Werner et al. 2016, 2018; Werner & Uzdensky 2021), developing from large gradients or reversals in the magnetic field. Dissipation of magnetic energy depends crucially on the magnetic topology and the stability of the plasma configuration.

Axially symmetric magnetic field configurations may involve ordered poloidal and toroidal components. As they

expand over several orders of magnitude in distance, the poloidal component decays faster than the toroidal component. Even if the configurations are initially dominated by the poloidal component, the toroidal component can in principle become dominant at some point. Toroidal magnetic fields are well-known to be unstable to either current-driven or pressure-driven pinch (sausage) and kink modes (e.g., Kruskal & Schwarzschild 1954; Kadomtsev 1966; Freidberg 1982). These instabilities have been proposed to be the trigger of magnetic dissipation in relativistic jets of active galactic nuclei (AGNs) and gamma-ray bursts (GRBs), and in pulsar wind nebulae (Begelman 1998; Drenkhahn & Spruit 2002; Giannios & Spruit 2006).

Most analytic studies of the stability of relativistic magnetized jets have been performed in cylindrical geometry (e.g., Istomin & Pariev 1994; Begelman 1998; Lyubarskii 1999; Appl et al. 2000; Tomimatsu et al. 2001; Nalewajko & Begelman 2012; Bodo et al. 2013; Das & Begelman 2019; Bodo et al. 2019).⁶ This allows one to introduce a cylindrical coordinate system (r, ϕ, z) , in which all equilibrium parameters depend solely on r . Various assumptions have been adopted on the radial profile of the toroidal magnetic field $B_\phi(r)$, the presence of the axial (poloidal) magnetic field $B_z(r)$, and crucially on the radial force balance, which may involve contributions from the magnetic field, gas pressure, centrifugal force, and radial shear of the axial velocity.

One line of research has been to adopt the force-free (FF) approximation, in which contributions from the gas pressure or inertia are neglected, and the $(\mathbf{j} \times \mathbf{B})/c$ force density due to

⁶ However, the effects of jet collimation can be important (e.g., Narayan et al. 2009).



$B_\phi(r)$ is balanced by that due to $B_z(r)$ (the *screw-pinch* configuration). In the FF limit, it has typically been found that the pinch mode (with azimuthal wavenumber $m = 0$) is stable, and that the dominant unstable mode is the *global* (or *external*, with axial wavelength λ_z comparable to the jet radius R_j) $m = 1$ kink mode (e.g., Istomin & Pariev 1994; Lyubarskii 1999; Appl et al. 2000; Bodo et al. 2013).

Another line of research has been to balance the force due to $B_\phi(r)$ with gas pressure gradients, even without any axial magnetic fields ($B_z = 0$). In this *Z-pinch* configuration, the most unstable modes are *internal* (with short axial wavelengths $\lambda_z \ll R_j$). They can also be *local* (localized at large radii as compared with the wavelength $\lambda_z \ll r$), and can be either pinch or kink modes (as the growth rate depends weakly on m) (Begelman 1998; Nalewajko & Begelman 2012; Das & Begelman 2019).

The stability and nonlinear evolution of relativistic jets have been investigated numerically using 3D relativistic MHD (RMHD) simulations. The simplest approach has been to consider a static, cylindrically symmetric column representing the innermost jet region in its comoving frame. Such simulations have been performed in both the FF limit (Mizuno et al. 2009; Bromberg et al. 2019; Mukherjee et al. 2021; Bodo et al. 2022) and the Z-pinch limit (Mizuno et al. 2011a). These two regimes have been compared in the work of O’Neill et al. (2012), which emphasized a dramatically more disruptive outcome of instability in the Z-pinch case, a result well known in fusion plasma physics (e.g., Freidberg 1982). Further studies in the FF regime considered the effects of radial shear of the axial velocity (Mizuno et al. 2011b, 2014) or rotation about the symmetry axis (Mizuno et al. 2012; Singh et al. 2016).

Global 3D MHD and RMHD simulations resulting in the development of current-driven instabilities have been performed for nonrelativistic and relativistic jets in AGNs (Nakamura & Meier 2004; Moll et al. 2008; McKinney & Blandford 2009; Mignone et al. 2010; Tchekhovskoy & Bromberg 2016), gamma-ray bursts (Bromberg & Tchekhovskoy 2016), and pulsar wind nebulae (Mignone et al. 2013; Porth et al. 2014). These simulations demonstrated consistently that the dominant modes are either pinch or kink.

MHD simulations are able to provide limited information about nonthermal particle acceleration, e.g., in the test particle approximation (e.g., Puzzoni et al. 2021). However, in order to fully account for kinetic effects, the particle-in-cell (PIC) algorithm is the method of choice. Recently, the results of the first 3D kinetic collisionless PIC simulations of static cylindrical columns with relativistically strong toroidal magnetic fields in pair plasmas have been reported. In the work of Alves et al. (2018), a radial profile of toroidal magnetic field with an exponentially decaying outer tail was balanced entirely by gas pressure (the Z-pinch or the screw-pinch with uniform axial field B_z), which resulted in internal unstable modes.⁷ On the other hand, in the work of Davelaar et al. (2020), toroidal magnetic field with a power-law tail (approximately $B_\phi \propto r^{-1}$) was balanced by a nonuniform axial field B_z in the FF screw-pinch configuration with subrelativistically warm plasma, which resulted in external unstable modes.

Alves et al. (2018, 2019) demonstrated nonthermal particle acceleration associated with pressure-driven modes. They

obtained power-law energy distributions $dN/d\gamma \propto \gamma^{-p}$ ⁸ with the index $p \sim 2-3$. These distributions extended to the maximum energy of $\gamma_{\max} \simeq (1.6-1.9)\gamma_{\lim}$, where

$$\gamma_{\lim} \equiv \frac{|q|B_0R_0}{mc^2} \quad (1)$$

is the energy limit⁹ (corresponding to the Hillas criterion; Hillas 1984), referred to as the *confinement energy* (see Appendix A). This limit has been tentatively confirmed by Davelaar et al. (2020), who also found power-law particle energy distributions with $p \sim 3-5$ and maximum energy of $\gamma_{\max} \simeq \gamma_{\lim}/6$.

Both Alves et al. (2018, 2019) and Davelaar et al. (2020) investigated the nature of electric fields accelerating particles in unstable cylindrical jets, using the electric field component $E_{\parallel} = (\mathbf{E} \cdot \mathbf{B})\mathbf{B}/B^2$ parallel to the local magnetic field \mathbf{B} as a proxy for the nonideal electric field component $E_{\text{nonid}} = \mathbf{E} - \mathbf{B} \times \beta_b$, where $\beta_b = v_b/c$ is the bulk velocity v_b in units of c . In the gas-pressure-balanced configurations investigated by Alves et al. (2018, 2019), perpendicular electric fields $E_{\perp} = \mathbf{E} - E_{\parallel}$ dominate particle acceleration. On the other hand, in the $B_z(r)$ -supported FF configurations investigated by Davelaar et al. (2020), it has been argued that both perpendicular and parallel fields contribute to particle acceleration, the latter due to finite-guide-field reconnection.

In this work, we introduce a new radial profile of toroidal magnetic field that approximates a power law, $B_\phi(r) \propto r^{\alpha_{B_\phi}}$, with the toroidal field index $\alpha_{B_\phi} \leq 0$. The force due to $B_\phi(r)$ is balanced initially by combinations of forces due to axial magnetic field and gas pressure, using a single pressure mixing parameter f_{mix} to transition between the FF screw-pinch configuration with no gas pressure gradients ($f_{\text{mix}} = 0$) and the Z-pinch configuration with $B_z = 0$ ($f_{\text{mix}} = 1$). We perform a series of 3D kinetic PIC simulations of relativistic collisionless pair plasmas using this setup on a regular Cartesian grid with periodic boundaries. We investigate the effects of the key parameters f_{mix} and α_{B_ϕ} on the development of instabilities and the resulting particle acceleration.

Section 2 describes the initial configuration used in our simulations. The presentation of our results begins from introducing basic details on our reference simulation in Section 3. Section 4 presents the results at the fluid level focused on the instability modes. In Section 4.1, we compare the strengths and linear growth timescales of the fundamental azimuthal modes in the distributions of the axial electric field component E_z . In Section 4.2, we compare the effective axial wavelengths of the E_z distributions. Section 5 presents the results at the kinetic level, with a focus on the particle acceleration. In Section 5.1, we investigate the maximum energies achieved by particles in our simulations. In Section 5.2, we investigate the role of parallel electric fields in particle acceleration. Section 6 contains a discussion of our results, and Section 7 provides our conclusions.

⁸ Here, $\gamma = (1 - \beta^2)^{-1/2} = \mathcal{E}/mc^2$ is the Lorentz factor of a particle with mass m , energy \mathcal{E} , and dimensionless velocity $\beta = v/c$, with c being the speed of light.

⁹ Here, q is the particle electric charge, and B_0 is roughly the peak value of $B_\phi(r)$ attained at the characteristic radius R_0 .

⁷ A related work by Alves et al. (2019) investigated the same magnetic configuration in nonrelativistic electron-ion plasmas, in some cases including the effect of Coulomb collisions.

2. Initial Configuration

We performed a set of 3D kinetic PIC simulations in electron–positron pair plasma, using a modified version of the public numerical code *Zeltron* (Cerutti et al. 2013).

In our standard collisionless implementation of the PIC method, the electric and magnetic fields \mathbf{E} , \mathbf{B} are represented on a staggered Cartesian Yee grid, and the gas is represented by individual macroparticles, from which a current density field \mathbf{j} is calculated and deposited on the Yee grid using the charge-conserving scheme of Esirkepov (2001). The \mathbf{E} , \mathbf{B} fields are advanced in time by solving directly the Ampère–Maxwell and Maxwell–Faraday equations:

$$\frac{\partial \mathbf{E}}{\partial t} = c \nabla \times \mathbf{B} - 4\pi \mathbf{j}, \quad (2)$$

$$\frac{\partial \mathbf{B}}{\partial t} = -c \nabla \times \mathbf{E}, \quad (3)$$

using a simple leapfrog algorithm (assuring the satisfaction of $\nabla \cdot \mathbf{B} = 0$ with numerical accuracy). The particle positions and momenta are advanced in time in a leapfrog scheme, using the Vay pusher algorithm for advancing the momenta under the local Lorentz force (Vay 2008). Our implementation is nominally of second-order accuracy, although the main source of inaccuracy is the limited number of macroparticles per grid cell.

Our simulations were performed in a cubic domain of physical size L ($-L/2 \leq x, y \leq L/2$; $0 \leq z \leq L$). Introducing a cylindrical coordinate system ($0 \leq r \leq R_{\text{out}}$; $0 \leq \phi < 2\pi$) centered along the $x = y = 0$ axis, one can fit in this domain an axially and translationally symmetric equilibrium with the outer radius $R_{\text{out}} = L/2$. The equilibrium is based on the radial profile of toroidal magnetic field $B_\phi(r)$ in the form of a power law with inner and outer cutoffs (see the upper left panel of Figure 1):

$$B_\phi(r) = B_0 \left(\frac{r}{R_0} \right)^{\alpha_{B\phi}} C(\alpha_{B\phi}, r) C(\alpha_{B\phi}, R_{\text{out}} - r), \quad (4)$$

$$C(\alpha_{B\phi}, r) = \frac{(r/R_0)^{1-\alpha_{B\phi}}}{1 + (r/R_0)^{1-\alpha_{B\phi}}},$$

with a *toroidal field index* $\alpha_{B\phi} \leq 0$ and a *core radius* $R_0 = R_{\text{out}}/10 = L/20$. These profiles peak at radii $R_{\text{peak}}/R_0 \simeq 0.84, 1, 1.55,$ and 5 , for $\alpha_{B\phi} = -1.5, -1, -0.5,$ and 0 , respectively. In order to achieve the most consistent scaling of our results with $\alpha_{B\phi}$, we introduce a characteristic radius $R_{B\phi}$ that is equal to R_{peak} for $\alpha_{B\phi} = -1.5, -1,$ and -0.5 , and equal to $R_{\text{peak}}/2$ for $\alpha_{B\phi} = 0$.

The initial equilibrium is provided by the axial electric current $j_z(r) = (c/4\pi r) d(rB_\phi)/dr$, as well as by a combination of the axial magnetic field $B_z(r)$ and the radial gas pressure $P_{rr}(r)$:

$$\frac{B_\phi}{4\pi r} \frac{d(rB_\phi)}{dr} + \frac{1}{8\pi} \frac{dB_z^2}{dr} + \frac{dP_{rr}}{dr} = 0. \quad (5)$$

We introduce a constant *pressure mixing parameter* $f_{\text{mix}} \in [0; 1]$, which is the fraction of the toroidal magnetic stress that is balanced by the gas pressure (with the remainder balanced

by the axial magnetic pressure):

$$\frac{dP_{rr}}{dr} = -f_{\text{mix}} \frac{B_\phi}{4\pi r} \frac{d(rB_\phi)}{dr}, \quad (6)$$

$$\frac{dB_z^2}{dr} = -(1 - f_{\text{mix}}) \frac{2B_\phi}{r} \frac{d(rB_\phi)}{dr}. \quad (7)$$

The case $f_{\text{mix}} = 0$ means that B_ϕ is balanced entirely by B_z (with uniform gas pressure; the FF screw-pinch), and the case $f_{\text{mix}} = 1$ means that B_ϕ is balanced entirely by the gas pressure ($B_z = 0$; the Z-pinch). For $\alpha_{B\phi} = -1$ and $f_{\text{mix}} < 1$ ($B_z \neq 0$), the magnetic pitch profile $\mathcal{P}(r) = rB_z(r)/B_\phi(r)$ is almost constant at $\mathcal{P}_0 = R_0 \sqrt{1 - f_{\text{mix}}}$ for $r < R_0$, then slightly decreasing with r , and then strongly increasing with r for $r > 4.5 R_0$. In the FF limit $f_{\text{mix}} = 0$, we have $\mathcal{P}_0 = R_0$, and since $L/\mathcal{P}_0 = 20 > 2\pi$, the Kruskal–Shafranov stability criterion is not satisfied, hence this configuration is predicted to be unstable (e.g., Bromberg et al. 2019).

For $f_{\text{mix}} < 1$, we also introduce a toroidal component of electric current density:

$$j_\phi(r) = (1 - f_{\text{mix}}) \frac{c}{4\pi r} \frac{B_\phi}{B_z} \frac{d(rB_\phi)}{dr}. \quad (8)$$

The initial profile of gas pressure $P_{rr}(r)$ determines the initial profile of gas density $n(r) = P_{rr}(r)/\Theta_0 m_e c^2$ for a uniform initial relativistic temperature $\Theta_0 = k_B T_0/m_e c^2$, where m_e is the electron mass, k_B is the Boltzmann constant, and T_0 is the initial temperature in kelvins. In our simulations, we have adopted an ultrarelativistic temperature with $\Theta_0 = 10^4$. In this work, we neglect the effects of radiative cooling, leaving this important topic for a future study.

In the case of nonuniform gas pressure ($f_{\text{mix}} > 0$), the gas density profile is normalized by adding a constant value to obtain the desired *density contrast* $\xi_n \equiv n_{\text{max}}/n_{\text{min}}$ —the ratio of maximum (central) n_{max} to minimum n_{min} density values. Two values have been adopted for the density contrast: a moderate value of $\xi_n = 10$ and a high value of $\xi_n = 100$. The density contrast is particularly important for determining the radial profile of the *hot magnetization* based on the total magnetic field $\sigma_{\text{hot}}(r) = B^2(r)/4\pi w(r)$, where $w(r) \simeq 4\Theta_0 n(r) m_e c^2$ is the relativistic enthalpy density. A higher density contrast results in a lower gas density and higher magnetization outside the central core region (see Figure 1).

The case $f_{\text{mix}} = 0$ requires a uniform gas pressure, and hence a uniform gas density, which corresponds to a density contrast of $\xi_n = 1$. In this case, the gas density is normalized to a value such that the drift velocity profile $\beta_d(r) = \mathbf{j}(r)/\text{cen}(r)$ satisfies the condition that $\max(\beta_d) = 0.5$.¹⁰ For all other cases, we make sure that $\beta_d(r) \leq 0.5$.

The minimum value of gas pressure is given by $P_{\text{min}} = \Theta_0 n_{\text{min}} m_e c^2$. In the cases that involve axial magnetic field ($f_{\text{mix}} < 1$), we also add a small constant to $B_z(r)$, such that it satisfies the relation $\min(B_z^2) = 10^{-3} \max(B_z^2)$.

The key parameters of the initial configuration are thus f_{mix} , $\alpha_{B\phi}$, and ξ_n . Their values for our main simulations are listed in

¹⁰ Note that the axial current density peaks at $r = 0$ at the level of $j_{\text{max}} \simeq cB_0/2\pi R_0$, which implies a lower limit on the particle density $n_{\text{max}} \simeq j_{\text{max}}/ce\beta_d \gtrsim B_0/\pi e R_0$, which in turn implies an upper limit on the magnetization of $\sigma(r) \lesssim (B/B_0)^2 (n/n_{\text{max}})^{-1} (R_0/16\rho_0)$, which depends primarily on the scale separation between ρ_0 and R_0 .

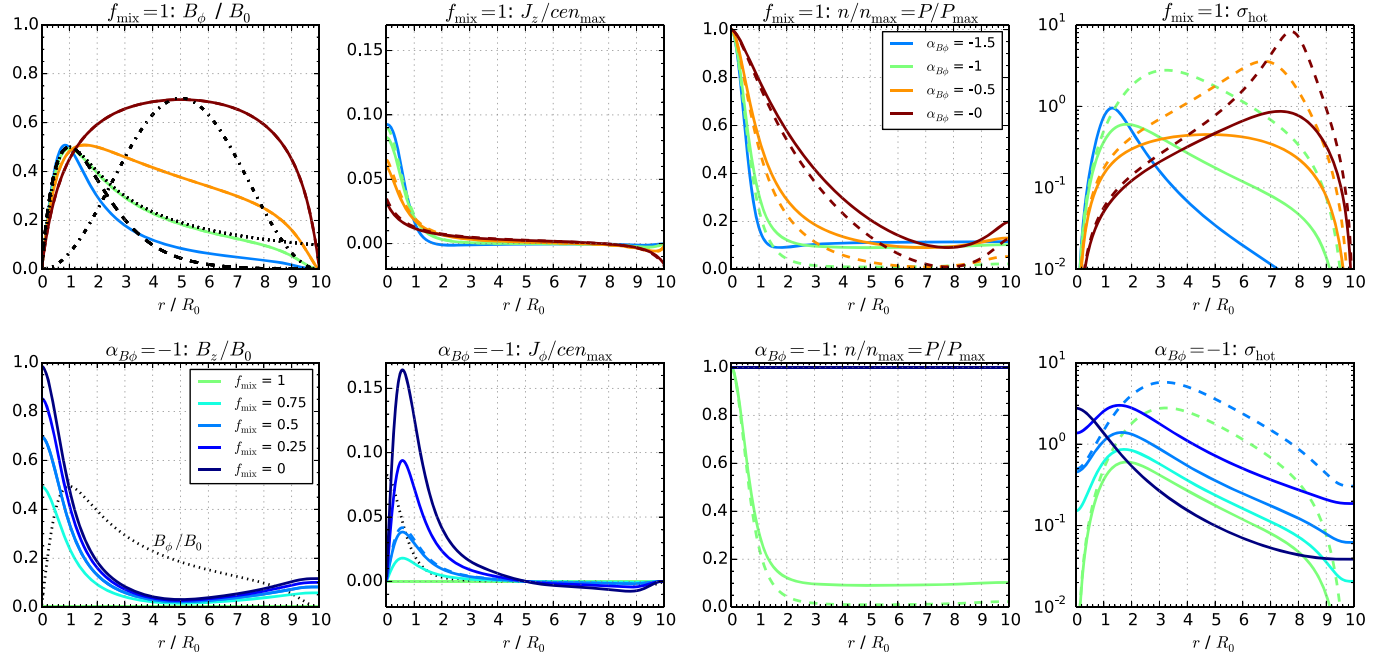


Figure 1. *Upper row of panels:* initial configurations compared for the series of simulations with gas pressure balance ($f_{\text{mix}} = 1$) and different toroidal field indices $\alpha_{B\phi}$ (indicated by line colors defined in the legend). *From left to right:* radial profiles of the initial toroidal magnetic field $B_\phi(r)$ in units of B_0 ; radial profiles of the axial current density $j_\phi(r)$ normalized to cen_{max} ; radial profiles of the gas density $n(r)$ normalized to n_{max} (proportional to the gas pressure $P(r)/P_{\text{max}}$); and radial profiles of the initial hot magnetization $\sigma_{\text{hot}}(r)$. For comparison with the configuration of our simulations, in the upper left panel we also show the “constant pitch” profile simulated by Mizuno et al. (2009), Bromberg et al. (2019), and Davelaar et al. (2020) (dotted black line); the exponentially decaying profile of Alves et al. (2018, 2019) (dashed black line); and the “sinusoidal” profile of O’Neill et al. (2012) (dashed-dotted black line). *Lower row of panels:* initial configurations compared for the series of simulations with the same toroidal field index $\alpha_{B\phi} = -1$ and different pressure-mixing parameters f_{mix} (indicated by line colors defined in the legend). *From left to right:* radial profiles of the initial axial magnetic field $B_z(r)/B_0$ (and the common profile of $B_\phi(r)/B_0$ with the black dotted line); radial profiles of the toroidal current density $j_\phi(r)/cen_{\text{max}}$ (and the common profile of $j_z(r)/cen_{\text{max}}$ with the black dotted line); radial profiles of the gas density $n(r)/n_{\text{max}} = P(r)/P_{\text{max}}$; and radial profiles of the initial hot magnetization $\sigma_{\text{hot}}(r)$ based on the total magnetic field. In both series, the solid color lines correspond to the moderate density ratio of $\xi_n = 10$, and the dashed color lines correspond to the high density ratio of $\xi_n = 100$.

Table 1

List of Performed Simulations with the Key Parameters of the Initial Configurations

Label	f_{mix}	$\alpha_{B\phi}$	ξ_n
f0_alpha-1_xi1	0	-1	1
f025_alpha-1_xi10	0.25	-1	10
f05_alpha-1_xi10	0.5	-1	10
f05_alpha-1_xi100	0.5	-1	100
f075_alpha-1_xi10	0.75	-1	10
f1_alpha-15_xi10	1	-1.5	10
f1_alpha-1_xi10 (ref)	1	-1	10
f1_alpha-1_xi100	1	-1	100
f1_alpha-05_xi10	1	-0.5	10
f1_alpha-05_xi100	1	-0.5	100
f1_alpha0_xi10	1	0	10
f1_alpha0_xi100	1	0	100

Table 1. The initial radial profiles of $B_\phi(r)$, $B_z(r)$, $j_\phi(r)$, $j_z(r)$, $n(r) \propto P(r)$, and $\sigma_{\text{hot}}(r)$ are compared in Figure 1.

Our simulations were performed on a numerical grid size of $N = 1152$, with a numerical resolution $dx = dy = dz = L/N = \rho_0/1.28$, where $\rho_0 = \Theta_0 m_e c^2 / e B_0$ is the nominal particle gyroradius, with e being the positron charge and $R_0/\rho_0 = 45$. The number of particles of both species per grid cell is 16. The actual set of macroparticles in each cell is drawn from Lorentz-boosted Maxwell–Jüttner distributions, the appropriate moments of which are consistent with $n(r)$, $\beta_d(r)$, and Θ_0 . The simulation time step was set as $dt = 0.99 dx / \sqrt{3} c$, according

to the Courant–Friedrichs–Lewy (CFL) condition. Digital filtering was applied at every time step to the current and charge densities deposited on the Yee grid. Periodic boundary conditions were adopted at all faces of the Cartesian domain. The edge regions that would correspond to $r > R_{\text{out}}$ were initialized with $B_\phi = 0$, $\mathbf{j} = 0$ and uniform B_z , n , P .

Our simulations have a typical duration of $\sim 5 L/c$. In some cases, we interrupt them at an earlier time, once the perturbations produced by the instability reach the x , y domain boundaries. This is formally defined by considering whether the root mean square of the axial electric field component $\text{rms}(E_z)$, calculated within an outer cylindrical shell $9 < r/R_0 < 10$ (see Section 4.1), exceeds the level of $2 \times 10^{-3} B_0$. Once that happens during an episode of rapid growth, the simulation is interrupted at the end of that episode.

3. Results: Introducing the Reference Case

We begin the presentation of our results by introducing some basic details on the reference case, which we choose to be the simulation f1_alpha-1_xi10 with toroidal field index $\alpha_{B\phi} = -1$ balanced entirely by gas pressure ($f_{\text{mix}} = 1$), which is the case closest to the configurations investigated by Alves et al. (2018).

Figure 2 presents selected snapshots from the reference simulation. We show 2D (x, z) slices along the $y = 0$ plane (containing the symmetry axis $r = 0$ of the initial configuration) for the out-of-plane magnetic field component B_y (dominated by the toroidal component B_ϕ) and for the axial electric field component E_z , as well as (x, y) slices along the $z = 0$ plane for

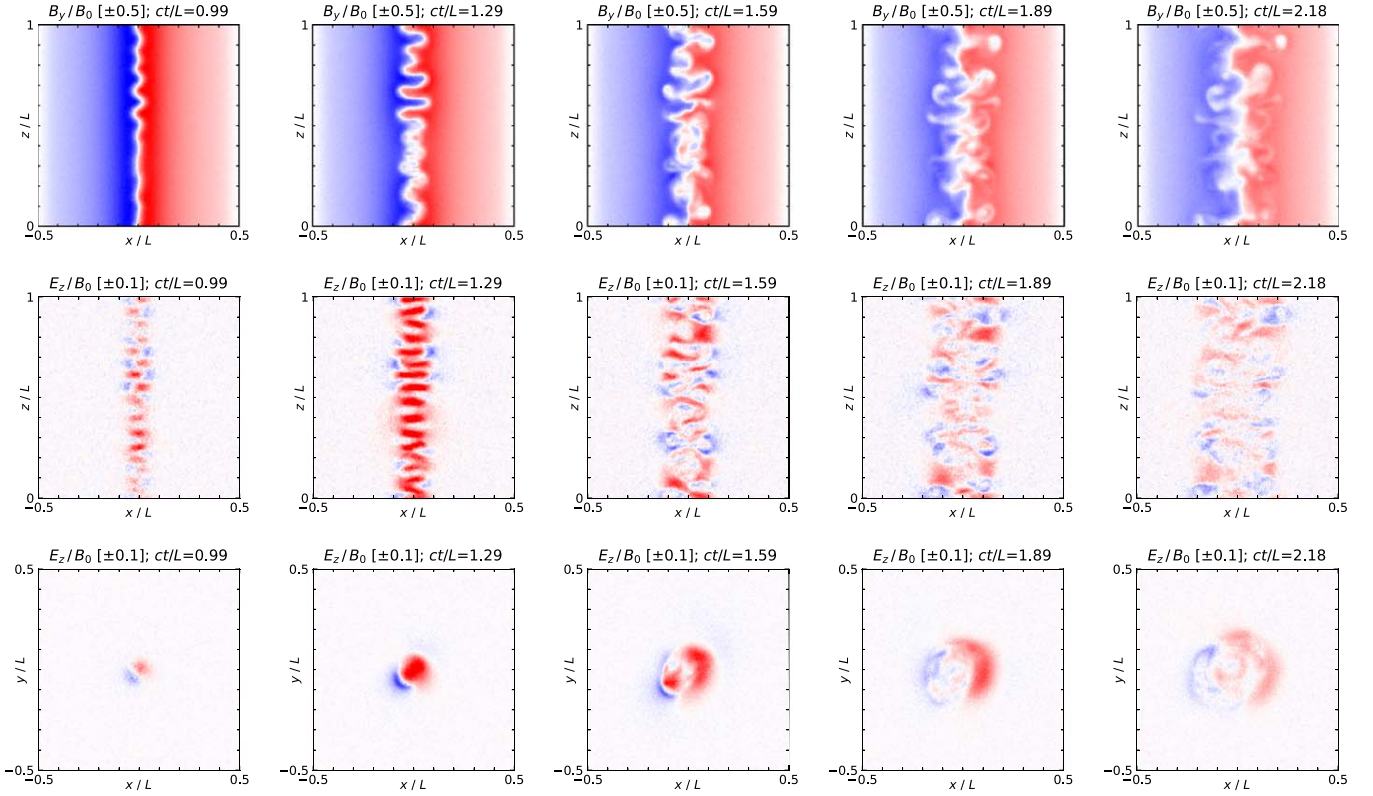


Figure 2. Maps of the magnetic field component B_y (top row of panels) and the electric field component E_z (middle row of panels) in the $y = 0$ plane, as well as the E_z component in the $z = 0$ plane (bottom row of panels), all in units of B_0 (positive values in red, negative in blue), at regular time intervals (from left to right) for the reference simulation fl_α-1_ξ10.

E_z , at five uniformly spaced moments in time. The sequence illustrates the development of unstable modes beginning in the central core region and growing outward. These are characterized by a short wavelength along z ($\lambda_z \simeq 2.7 R_0$, which means $\simeq 7.5$ full wavelengths per L ; see Section 4.2) and varying levels of asymmetry in the (x, y) plane, suggesting the dominance of the $m = 1$ kink mode.¹¹ They break into a nonlinear phase by $t \simeq 1.6 L/c$. The axial electric field appears to be the strongest and largely positive around $t \simeq 1.3 L/c$.

The left panels of Figure 3 present the radial profiles of the mean toroidal magnetic field $\langle B_\phi \rangle(r)$ (averaged over z and ϕ) and the mean axial electric field $\langle E_z \rangle(r)$ for the same five moments in time. At $t \simeq L/c$, the toroidal magnetic field profile is still very similar to the initial one, while a net positive axial electric field builds up along the axis. For $1.0 < ct/L < 1.6$, we observe rapid decay of the toroidal magnetic field within $r < 3R_0$. Note from Figure 2 that, by $ct/L \simeq 1.6$, a turbulent structure of both B_y and E_z develops exactly within these radii ($|x| < 0.15L$). Therefore, we consider this decay of B_ϕ as an irreversible magnetic dissipation. We will refer to this period of time as the *fast magnetic dissipation phase*; its beginning and ending are indicated with thick lines. At the end of the fast magnetic dissipation phase ($t \simeq 1.6 L/c$), $\langle B_\phi \rangle(r)$ peaks at the level of $\simeq 0.28 B_0$ at a radius of $r \simeq 2.7R_0$. Using these numbers, we can estimate the post-dissipation energy limit as $e(0.28B_0)(2.7R_0) \simeq 0.76\gamma_{\text{lim}}$, a rather minor decrease from

¹¹ A further analysis reveals that this mode is circularly polarized, i.e., the phase ϕ_1 is a strong quasi-periodic function of z and a weak function of simulation time.

the initial value. The net axial electric field shoots up to $\simeq 0.07B_0$ in the middle of the fast magnetic dissipation phase and decays to $\simeq 0.02B_0$ by $t \simeq 1.6 L/c$. For $t > 1.6 L/c$, dissipation of toroidal magnetic field is significantly slower and $\langle E_z \rangle(r)$ does not exceed $\simeq 0.01 B_0$.

Figure 4 compares the particle momentum $u = \gamma\beta$ ($u \simeq \gamma$ for $\gamma \gg 1$) distributions dN/du compensated by u^2 for the same five moments in time. The distribution at $t \simeq L/c$ is indistinguishable from the initial Maxwell–Jüttner distribution. The fast magnetic dissipation phase corresponds to a rapid buildup of a high-energy component of the distribution. The high-energy component evolves much more slowly for $t > 1.6 L/c$. The most energetic particles approach the energy limit, which in our simulations amounts to $\gamma_{\text{lim}} = 45\Theta_0$. Based on such momentum distributions, we define the *maximum particle energy* γ_{max} as corresponding to the u_{max} value at which $u^2 dN/du$ equals 10^{-4} of the peak level determined at $t = 0$.

4. Results: Instability Modes

4.1. Pinch versus Kink Modes

Here, we compare the relative strengths of the two fundamental azimuthal instability modes—the $m = 0$ pinch versus the $m = 1$ kink—in both the linear and nonlinear stages. We have analyzed the 3D spatial distributions of the axial electric field component E_z . Using the cylindrical coordinates (r, ϕ, z) centered at the initial symmetry axis, we define a series of cylindrical shells \mathcal{S}_n for $n \in \{1, \dots, 9\}$ delimited by $R_{n-1} < r < R_n$, where $R_n = (n + 1)R_0$, so that $R_9 = R_{\text{out}}$. For the pinch mode, we have also analyzed the central core region $r < R_0$ (the

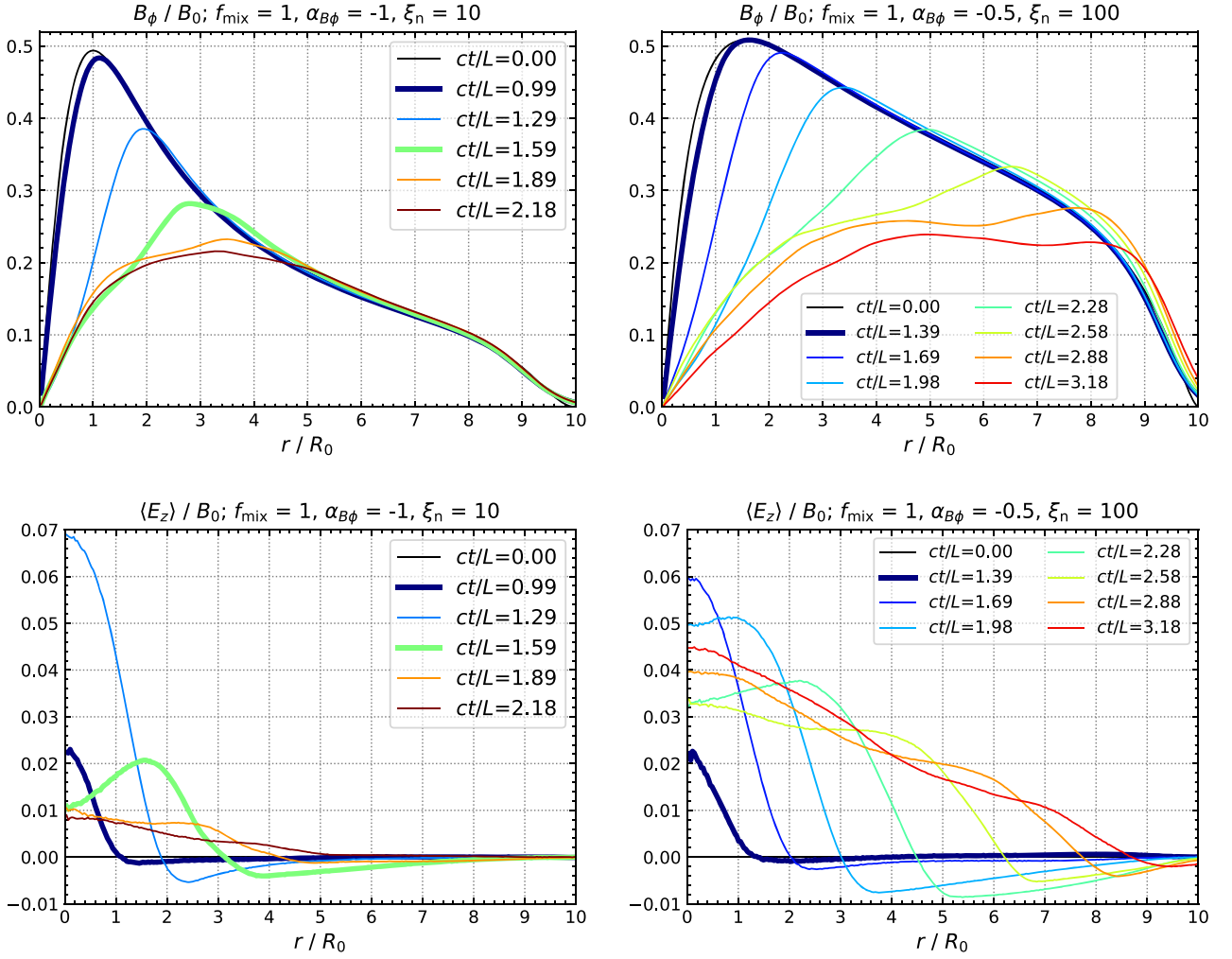


Figure 3. *Top left panel:* radial profiles of the mean toroidal magnetic field $\langle B_\phi \rangle(r)$ (averaged over z and ϕ) for the five moments in time of the reference simulation f1_α-1_ξ10 presented in Figure 2 (and for $t=0$). *Top right panel:* radial profiles of $\langle B_\phi \rangle(r)$ for the simulation f1_α-05_ξ100. *Bottom panels:* radial profiles of the mean axial electric field $\langle E_z \rangle(r)$ (averaged over z and ϕ) normalized to B_0 for the same moments in time of the same simulations as in the respective top panels.

S_0 shell). Within each shell, the values of E_z have been averaged over r . Then, for every value of z , the function $\langle E_z \rangle(\phi, z)$ has been decomposed into a Fourier series $\sum_m E_m(z) \cos[m\phi + \phi_m(z)]$ with real amplitudes $E_m(z)$ and phases $\phi_m(z)$. These amplitudes have been averaged over z and will be presented as functions of simulation time.

Figure 5 presents the spacetime diagrams (r, t) of the amplitudes of the pinch and kink modes for two simulations, including all nine shells $\{S_1, \dots, S_9\}$, and for the pinch mode also the core region S_0 . In the reference case f1_α-1_ξ10 (two left panels in Figure 5), we find a strong pinch mode (with $E_0 \sim 0.1B_0$) highly localized in both radius and time. In the core region, it is found for $1.0 < ct/L < 1.5$, which is during the fast magnetic dissipation phase. It is also found in the first shell S_1 during a slightly later period of $1.3 < ct/L < 1.6$. A slightly weaker kink mode is more extended in both time and radius. In the first shell, it can be seen for $1.1 < ct/L < 1.8$; in the next two shells ($2 < r/R_0 < 4$) it is successively delayed at a rate similar to that for the pinch mode. These modes appear to originate in the central core region and propagate radially outward. At lower amplitude levels of $\sim 10^{-3}B_0$, the pinch mode appears to propagate at a velocity of $\sim 0.4c$, faster than the kink mode ($\sim 0.2c$).

In the case f1_α0_ξ100 (two right panels in Figure 5), both the pinch and the kink modes achieve higher amplitudes of $\sim 0.1B_0$, starting around $t \simeq 2L/c$ and lasting at least until $t \simeq 4.3L/c$, at which point the simulation has been interrupted because the modes reached the outer boundary according to the criterion described in Section 2. Both modes appear to originate in the central core and propagate outward with similar velocities $\sim 0.2c$. Looking at the amplitude levels of $\sim (10^{-2.5} - 10^{-2.0})B_0$ of the pinch mode, we see an excess signal in the S_5, S_6 shells ($5 < r/R_0 < 7$) at $ct/L \simeq 2.5-3$. Such a signal is not seen in the kink mode, and it also is not found (at least that clearly) in our other simulations. We discuss the origin of this radially localized pinch mode in Section 6.

We now focus on the first shell S_1 ($1 < r/R_0 < 2$). Figure 6 compares the time evolutions of the $m=0, 1$, and 2 modes for two series of simulations: $f_{\text{mix}} = 1$ (varying $\alpha_{B\phi}$ and ξ_n) and $\alpha_{B\phi} = -1$ (varying f_{mix} and ξ_n). In the $f_{\text{mix}} = 1$ series (upper panels in Figure 6), the amplitudes of the $m=0$ pinch modes are comparable to the amplitudes of the $m=1$ kink modes, and the $m=2$ modes are only slightly weaker. With the simulation time t scaled by the characteristic radius $R_{B\phi}$, the evolutions of the modes are similar for different values of $\alpha_{B\phi}$. At the same time, the mode evolution is not sensitive

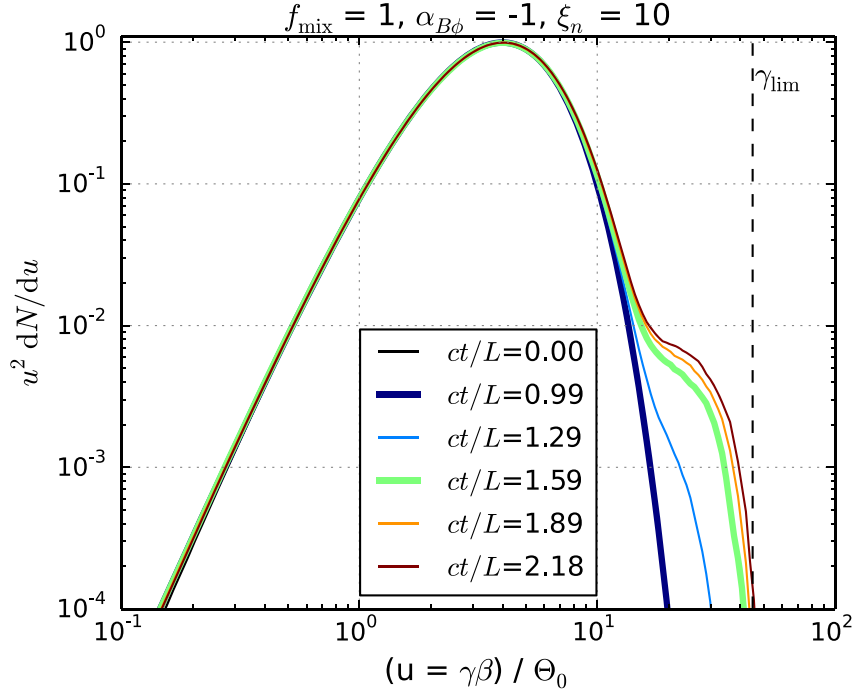


Figure 4. Particle momentum distributions $u^2 dN/du$ (equivalent to energy distributions since $\Theta_0 \gg 1$), combined for both electrons and positrons and normalized to peak at unity, for the five moments in time of the reference simulation fl_α-1_ξ10 presented in Figure 2. The vertical dashed line indicates the *confinement* energy limit $\gamma_{\text{lim}} = 45\Theta_0$.

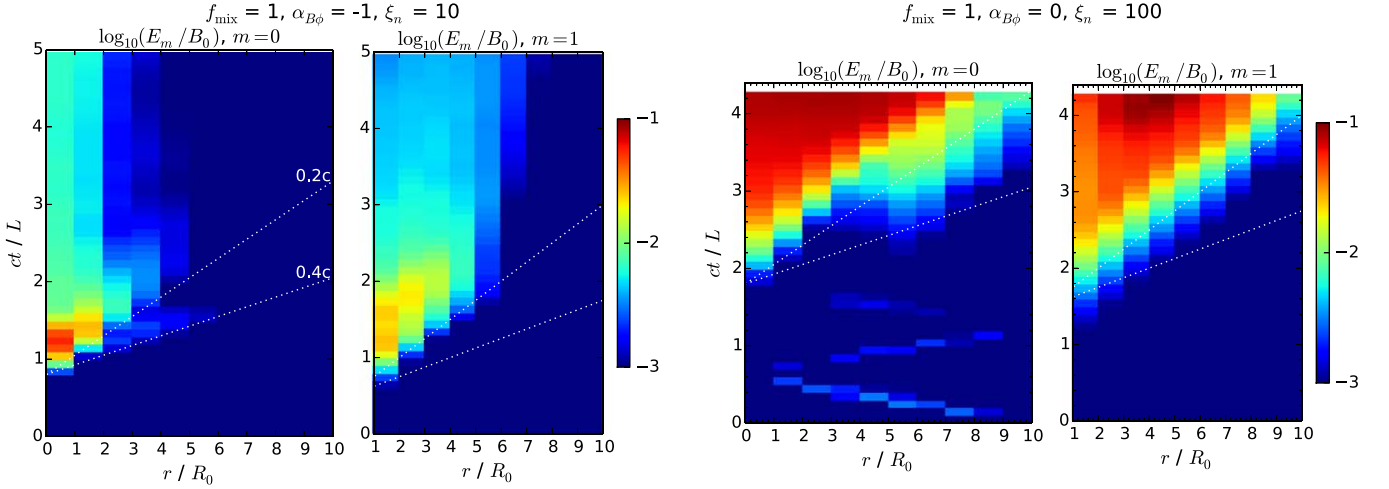


Figure 5. Spacetime diagrams of the amplitudes E_m (averaged over z) of the azimuthal modes m of the $E_z(\phi, z)$ distributions compared for two simulations. The white dotted lines indicate the speed levels of $0.2c$ and $0.4c$. In the case fl_α0_ξ100, the simulation was interrupted at $ct/L \simeq 4.27$ when the perturbations reached the boundary according to the definition described in Section 2.

to the density contrast ξ_n , especially in the linear stage. In all simulations, we find that the kink mode is the first to emerge (roughly when $\langle E_l \rangle$ exceeds the $10^{-3}B_0$ level) followed by the pinch mode and all the higher modes ($m \geq 2$).

In the $\alpha_{B\phi} = -1$ series (lower panels in Figure 6), we observe a systematic weakening of the pinch mode together with a strengthening of the kink mode with decreasing value of f_{mix} (in agreement with the linear analysis of Bodo et al. 2013). The reason for this is that the axial magnetic flux resists radial compression, and hence stabilizes the $m = 0$ pinch mode for $f_{\text{mix}} \rightarrow 0$. For $f_{\text{mix}} < 1$, the evolution of the pinch mode does not even show regular linear stages of exponential growth, while the kink mode shows linear stages extending over

two orders of magnitude in $\langle E_l \rangle$, reaching values up to $0.1B_0$ in the case $f_{\text{mix}} = 0.5$ and $\xi_n = 100$. Higher modes ($m \geq 2$) are once again systematically weaker and delayed.

We have measured the minimum growth timescales $\tau_{\text{min}} = (c\Delta t/R_{B\phi}) \min(1/\Delta \ln \langle E_m \rangle)$ for each mode m in every studied case; their values are compared in Figure 7 (the corresponding segments of the $\langle E_m \rangle(t)$ functions are indicated in Figure 6). One should note that the time resolution for this analysis is limited to $\Delta t \simeq 2R_0/c$, hence any shorter timescales should be considered as upper limits. Nevertheless, our results indicate that the pinch modes are typically the fastest ones ($\tau_{\text{min}} < 2$ for $f_{\text{mix}} = 1$), and the kink modes are typically the slowest ones ($\tau_{\text{min}} > 2$). In general, the value of τ_{min} decreases with

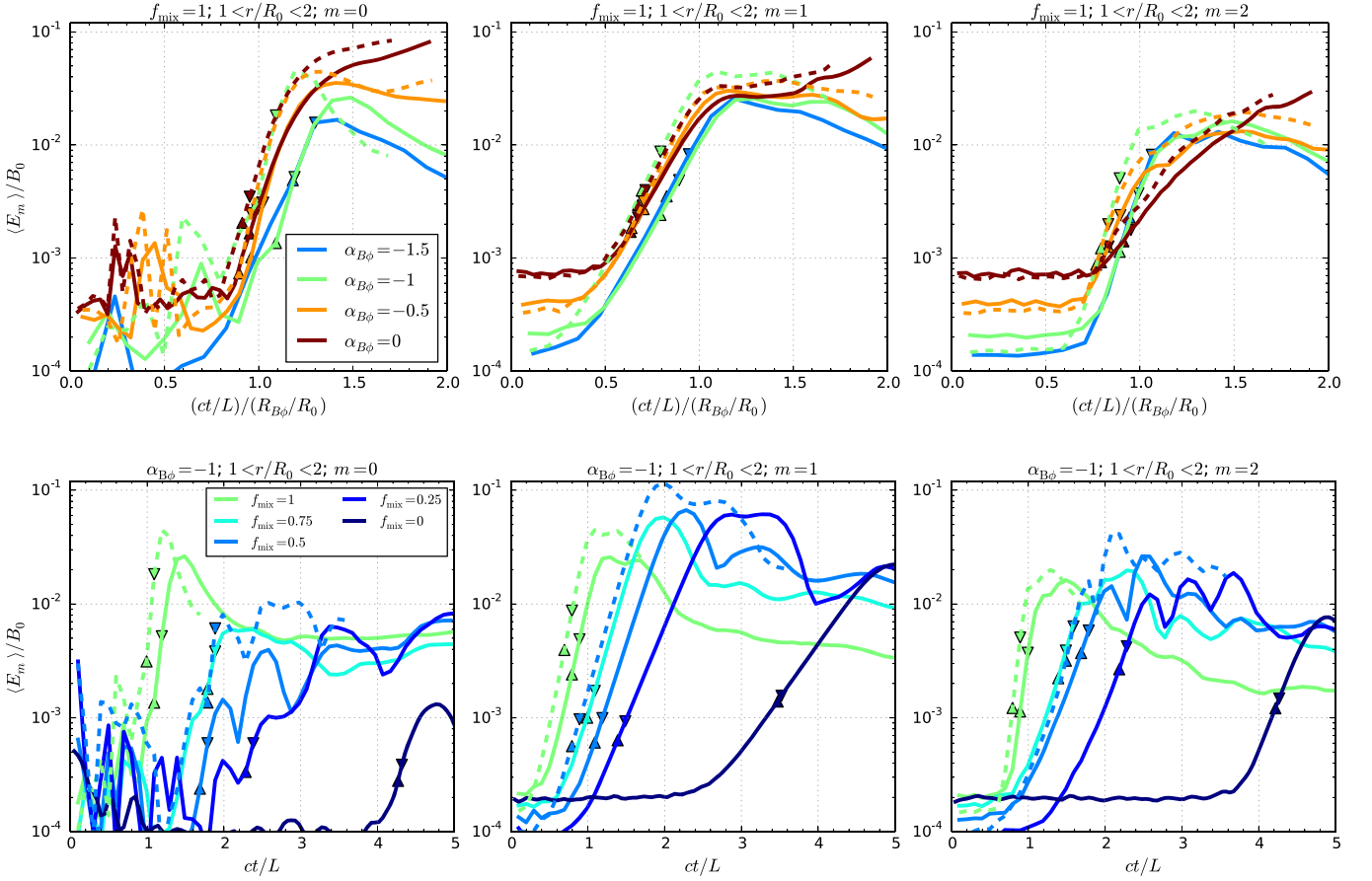


Figure 6. Amplitudes E_m of the azimuthal modes m of the axial electric field E_z extracted from the $1 < r/R_0 < 2$ cylindrical shell, averaged over z and presented as functions of the simulation time t scaled by the characteristic radius $R_{B\phi}$. The upper row of panels compares the simulations with $f_{\text{mix}} = 1$, different values of $\alpha_{B\phi}$ (indicated by the line color), and different values of ξ_n (10: solid lines, 100: dashed lines). The lower row of panels compares the simulations with $\alpha_{B\phi} = -1$, different values of f_{mix} (indicated by the line color), and different values of ξ_n (as before). The left panels show the $m = 0$ pinch mode, the middle panels show the $m = 1$ kink mode, and the right panels show the $m = 2$ mode. The triangles indicate the line segments for which the growth timescale τ of the mode amplitude is minimized.

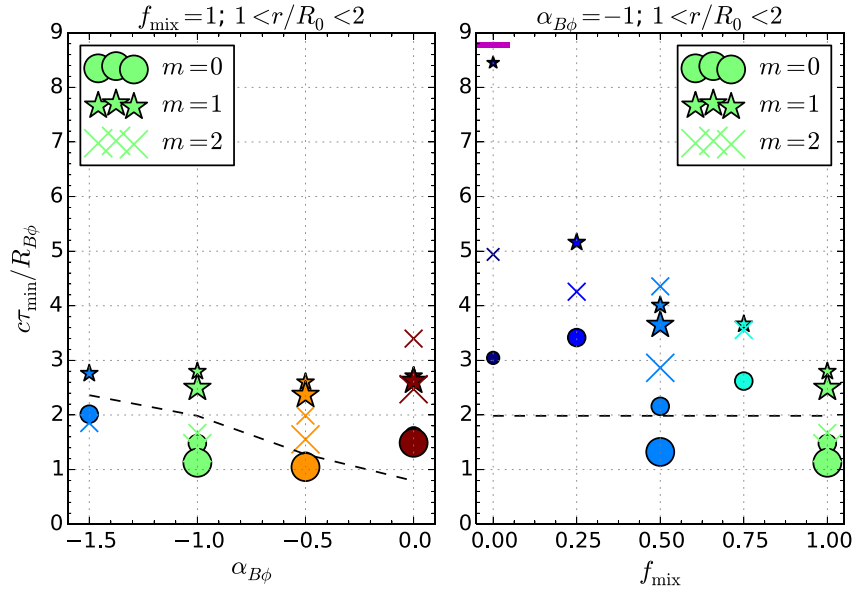


Figure 7. Minimum growth timescales τ_{min} normalized to $R_{B\phi}/c$ evaluated for the amplitudes E_m of the azimuthal modes of E_z presented in Figure 6. The symbol colors correspond to the line colors used in Figure 6. Different symbol types indicate the mode number m . For each symbol type, the smaller symbols correspond to $\xi_n = 10$, and the larger symbols correspond to $\xi_n = 100$ (except for the case $f_{\text{mix}} = 0$, in which $\xi_n = 1$). The short magenta line in the right panel indicates the analytical prediction for the $|m| = 1$ kink mode in the constant-pitch FF configuration (Appl et al. 2000). The black dashed lines mark the time-resolution limit for this analysis.

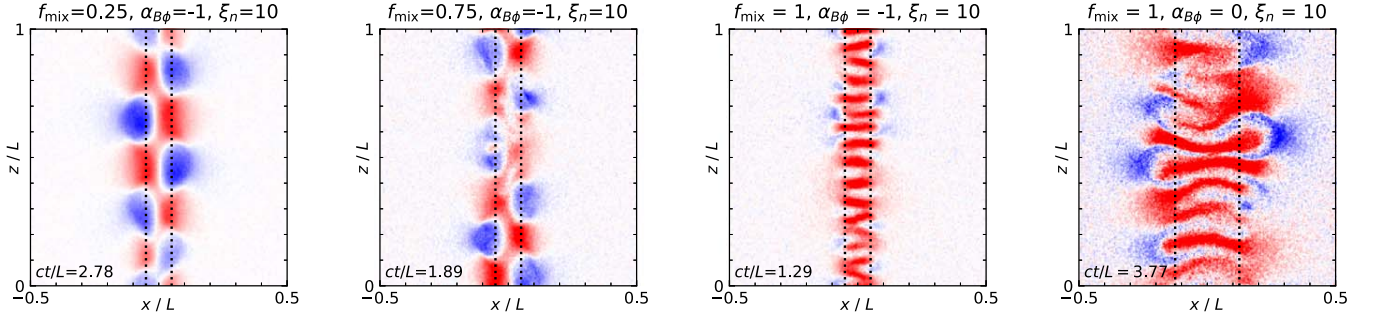


Figure 8. Maps of electric field component E_z in units of B_0 (positive values in red, negative in blue) in the $y = 0$ plane, compared for several simulations at the moments (indicated in the bottom left corners) of peak root-mean-square value of E_z evaluated at $r = R_0$. The vertical dotted lines indicate $r = R_{B\phi}$, which equals R_0 for $\alpha_{B\phi} = -1$ and $2.5R_0$ for $\alpha_{B\phi} = 0$.

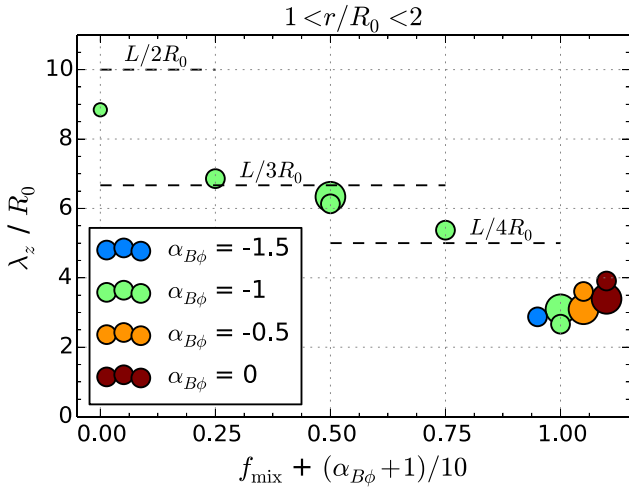


Figure 9. Effective axial wavelength λ_z of the $\langle E_z \rangle(z)$ fluctuations measured within the cylindrical shell region \mathcal{S}_1 ($1 < r/R_0 < 2$) at the moments of peak rms(E_z). The smaller symbols correspond to $\xi_n = 10$, and the larger symbols correspond to $\xi_n = 100$ (except for the case $f_{\text{mix}} = 0$, in which $\xi_n = 1$).

increasing f_{mix} , and its dependence on $\alpha_{B\phi}$ is captured by its explicit scaling with $R_{B\phi}$.

4.2. Effective Axial Wavelength

Figure 8 compares the (x, z) maps in the $y = 0$ plane of the axial electric field component E_z for four selected simulations at the moments when the root-mean-square values of E_z evaluated at the central core radius $r = R_0$ achieve their peaks. In the case f025_α-1_ξ10, we observe a regular structure with the regions of $E_z > 0$ (red) slightly more extended than the regions of $E_z < 0$ (blue), aligned asymmetrically about the central axis (indicating the dominance of the kink mode), with three full wavelengths over $\Delta z = L$. In the case f075_α-1_ξ10, the structure of $E_z(x, z)$ appears to be very similar to the previous case; however, some short-wavelength kink-like fluctuations appear superposed. In the reference case f1_α-1_ξ10 (see Figure 2), we find a very different structure of E_z , in the form of a somewhat irregular stack of $\simeq 16$ short-wavelength patches of positive values, separated by narrow gaps of weak (but still positive) values. This can be compared with the last presented case f1_α0_ξ10, in which the $E_z > 0$ patches are much more extended radially, because in this case the evolution of the instability is longer by a factor $\simeq R_{B\phi}/R_0 = 2.5$.

Using the (r) -averaged profiles of $\langle E_z \rangle(\phi, z)$ extracted from the first cylindrical shell region \mathcal{S}_1 , we calculated the discrete Fourier transform $E_k(\phi) = \sum_j \langle E_z \rangle(\phi, z_j) \exp(-2\pi i k z_j / L)$ over a regular grid $0 \leq z_j < L$, averaged the $E_k(\phi)$ amplitudes over ϕ , then calculated the effective axial wavenumber $\langle k_z \rangle = (\sum_k k E_k^2) / (\sum_k E_k^2)$, and finally obtained the corresponding effective wavelength $\lambda_z = 2\pi / \langle k_z \rangle$. Figure 9 compares the values of λ_z for all our simulations. We find that λ_z is decreasing systematically with increasing f_{mix} . For $f_{\text{mix}} = 0$, we find that $\lambda_z \simeq 8.8R_0 \simeq L/2.25$, which reflects the dominance of two full wavelengths in the E_z structure. For $f_{\text{mix}} \sim 0.25$ – 0.5 , λ_z is consistent with $L/3$. For $f_{\text{mix}} = 0.75$, the effective wavelength is $\lambda_z \simeq 5.4R_0 \simeq L/3.7$, in agreement with a combination of long ($L/3$) current-driven modes characteristic of the FF screw-pinches and short pressure-driven modes characteristic of the Z-pinches (see the second left panel of Figure 8). For $f_{\text{mix}} = 1$, all of our simulations produce consistent values of $\lambda_z \simeq (2.7$ – $3.9)R_0 \simeq (L/7.5$ – $L/5)$, increasing somewhat with increasing $\alpha_{B\phi}$, but not scaling clearly with $R_{B\phi}$. There is little dependence of λ_z on the density ratio parameter ξ_n .

5. Results: Particle Acceleration

5.1. Fast Magnetic Dissipation Phase and Particle Energy Limit

In this subsection, we show that the Z-pinch configurations with steep toroidal field indices ($\alpha_{B\phi} \leq -1$) satisfy the γ_{lim} energy limit, while those with shallow indices ($\alpha_{B\phi} > -1$) exceed that limit. Energetic particles are well-confined within the jet core in either case. For $\alpha_{B\phi} \leq -1$, efficient magnetic dissipation proceeds over a limited period of time, transitioning from a *fast magnetic dissipation phase* to a *slow magnetic dissipation phase* before the perturbations reach the domain boundaries. We will argue that particle energies are limited by the finite time duration of the fast magnetic dissipation phase.

5.1.1. The Reference Case $f_{\text{mix}} = 1$ and $\alpha_{B\phi} = -1$

Figure 10 compares in detail the time evolutions of the toroidal magnetic flux (calculated as $\Psi_{B\phi} \propto \langle |B_y| \rangle$) with averaging over x and z along the $y = 0$ plane), the total magnetic energy \mathcal{E}_B , the mean axial electric field at $r = R_0$, and the maximum particle energy as a fraction of the energy limit, $\gamma_{\text{max}}/\gamma_{\text{lim}}$. The first thing to notice is that the relative decrease of toroidal magnetic flux (the thick green line) is very similar to the relative decrease of total magnetic energy (the thin green line), the main difference being an earlier onset

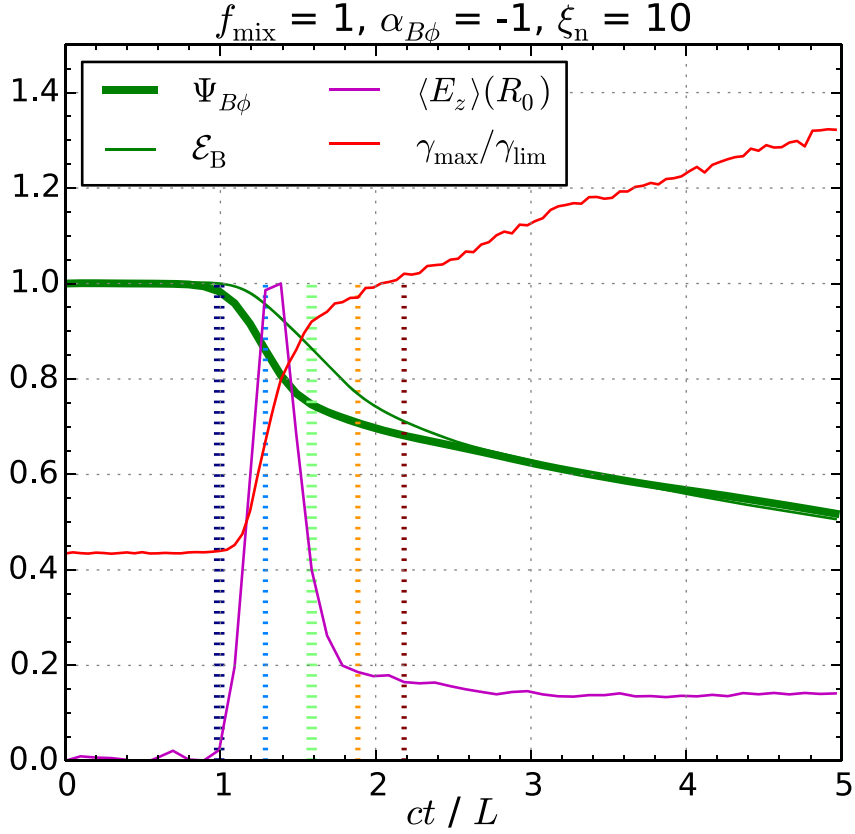


Figure 10. Time evolutions of the toroidal magnetic field B_ϕ and axial electric field E_z for the reference simulation fl $_{\alpha-1}$ $_{\xi 10}$. The thick green line shows the toroidal magnetic flux $\Psi_{B\phi}$ normalized to its initial value; the thin green line shows the total magnetic energy \mathcal{E}_B normalized to its initial value; the red line shows the maximum particle energy γ_{max} normalized to the Lorentz factor limit γ_{lim} ; the magenta line shows the mean axial electric field $\langle E_z \rangle$ (averaged over z and ϕ) evaluated at $r = R_0$ and normalized to its peak value of $E_{z,\text{peak}} = 0.043B_0$; the five vertical thick dotted lines indicate the five moments in time presented in Figure 2–4.

of the toroidal flux dissipation. The toroidal magnetic flux clearly shows two phases of magnetic dissipation—a fast magnetic dissipation phase for $1.0 < ct/L < 1.6$, followed by a slow magnetic dissipation phase (this is consistent with the results of Bodo et al. 2022).

Let us now discuss the evolution of the mean axial electric field $\langle E_z \rangle(R_0)$. The fast magnetic dissipation phase involves a temporary spike of $\langle E_z \rangle(R_0)$, peaking at the level of $\langle E_z \rangle_{\text{peak}} \simeq 0.043B_0$ for $t \sim (1.3\text{--}1.4)L/c$, simultaneous with the most rapid increase of γ_{max} .¹² To illustrate the connection between the electric field strength at $r = R_0$ and evolution of γ_{max} , consider a slightly different time period of $1.2 < ct/L < 1.7$, during which $\langle E_z \rangle(R_0)$ exceeds the level of $0.2\langle E_z \rangle_{\text{peak}}$. During that time period of $\Delta t \simeq 0.5L/c$, γ_{max} increases by $\Delta\gamma_{\text{max}} \simeq 18.8\Theta_0 \simeq 0.42\gamma_{\text{lim}}$. This energy gain corresponds to linear acceleration by the average electric field of $\langle E_{\text{acc}} \rangle/B_0 = (L/\rho_0)^{-1} \Delta(\gamma_{\text{max}}/\Theta_0)/\Delta(ct/L) \simeq 0.042 \simeq \langle E_z \rangle_{\text{peak}}/B_0$. Hence, the electric field strength $\langle E_{\text{acc}} \rangle$ required to explain the acceleration of the most energetic particles during that period is consistent with $\langle E_z \rangle_{\text{peak}}$.¹³ Our analysis of individually tracked particles confirms that the most energetic ones are indeed accelerated within the core region ($r < R_0$), predominantly by the positive axial electric field

during the fast magnetic dissipation phase, as stated by Alves et al. (2018).

The typical energy gain of an energetic particle can be derived directly from the duration Δt of the fast magnetic dissipation phase:

$$\frac{\Delta\gamma}{\gamma_{\text{lim}}} = \frac{1}{2} \left(\frac{L}{20R_0} \right) \left(\frac{c\Delta t}{L/2} \right) \frac{\langle E_{\text{acc}} \rangle}{B_0/20}, \quad (9)$$

where $\langle E_{\text{acc}} \rangle$ is the average electric field component along the particle velocity vector. This means that a relatively short duration $\Delta t \sim L/2c$, in combination with realistic electric field strengths, is sufficient to explain one half of the “confinement” limit (also known as the Hillas limit) on the particle energy gain.

As a representative example, let us consider the acceleration history of an individual energetic particle. The left panels of Figure 11 show the history of an energetic positron (denoted as “pos #107”) from the reference simulation. This positron is energized from $\simeq 0.2\gamma_{\text{lim}}$ to $\simeq 0.6\gamma_{\text{lim}}$ during the fast magnetic dissipation phase. The energy gain of $\Delta\gamma \simeq 0.4\gamma_{\text{lim}}$ over the timescale of $\Delta t \simeq 0.6L/c$ requires an average electric field of $\langle E_{\text{acc}} \rangle \simeq B_0/30$, which is consistent with the axial electric field E_z experienced by the positron. In the top panels of Figure 11, the dashed blue line shows that the acceleration of this particle can be attributed almost exclusively to the action of the axial electric field component E_z . Likewise, it can be demonstrated that the action of the electric field component

¹² The fastest e-folding growth timescale of $\langle E_z \rangle(R_0)$ has been estimated as $\tau_{E_z} \simeq 0.046L/c \simeq 0.9R_0/c$ over the period of $1.0 < ct/L < 1.1$. Hence, the duration of the fast magnetic dissipation phase corresponds to $\simeq 13\tau_{E_z}$.

¹³ One can note that, on one hand, the average axial electric field at R_0 during that time period should be roughly $\simeq 0.6\langle E_z \rangle_{\text{peak}}$; on the other hand, the axial field is somewhat stronger for $r < R_0$.

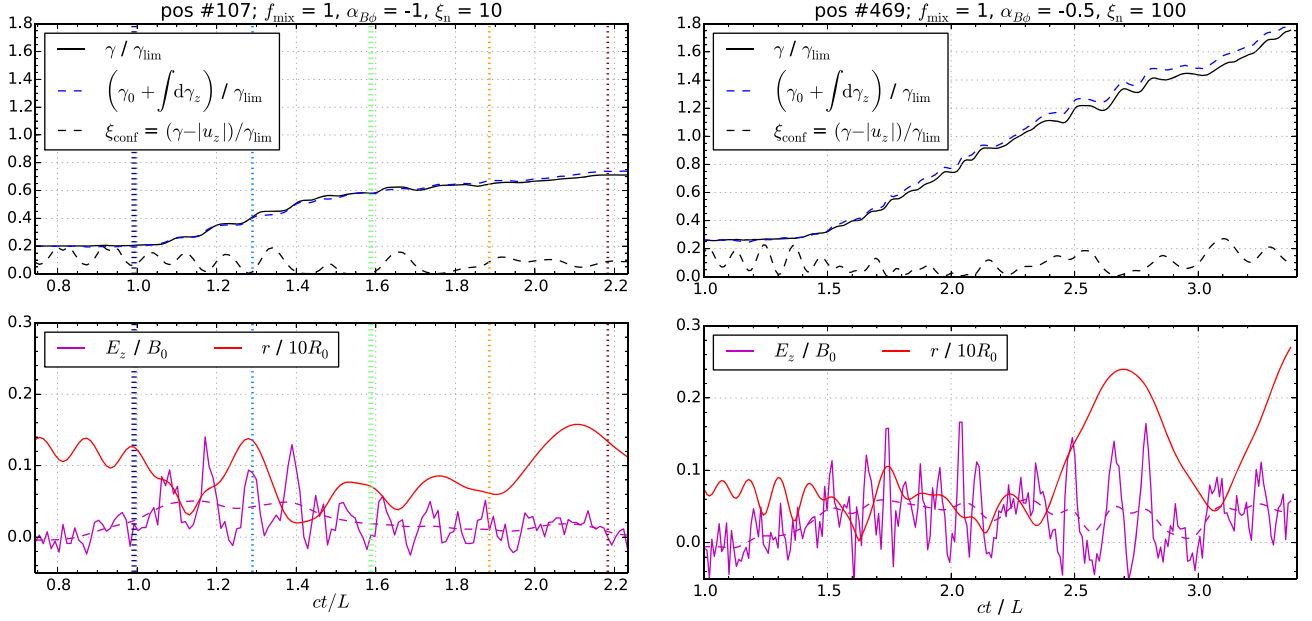


Figure 11. Acceleration histories of single energetic tracked positrons in the reference simulation f1_α-1_ξ10 (left panels) and in the simulation f1_α-05_ξ100 (right panels). In the top panels, the solid black lines show the particle Lorentz factor γ normalized to the energy limit $\gamma_{\text{lim}} = eB_0R_0/(mc^2)$; the dashed black lines show the particle confinement indicator $\xi_{\text{conf}} = (\gamma - |u_z|)/\gamma_{\text{lim}}$ (Appendix A); and the dashed blue lines show what would be the particle Lorentz factor due to the work done by the axial electric field component E_z . In the bottom panels, the solid magenta lines show the local axial electric field component E_z (the dashed magenta lines show its moving average) and the solid red lines show the particle radial coordinate r in units of $10R_0$. The five vertical thick dotted lines in the left panels indicate the five moments in time presented in Figures 2–4.

parallel to the local magnetic field is negligible in this case. During most of the fast magnetic dissipation phase and until $t \simeq 2L/c$, this positron is located within the central core at $r < R_0$. In order to determine whether this positron is confined to the central core by toroidal magnetic field, we calculate the *particle confinement indicator* defined as $\xi_{\text{conf}} = (\gamma - |u_z|)/\gamma_{\text{lim}}$ (see Appendix A). In the present case, we find that $\xi_{\text{conf}} < 0.2$ (other energetic particles in this simulation reached $\xi_{\text{conf}} \simeq 0.3$), which means that this particle is indeed confined (as are the others). The acceleration rate slows down significantly around the end of the fast magnetic dissipation phase at $t \simeq 1.6L/c$. The sole reason for slower acceleration is that the electric fields within the central core become weaker.

We have thus demonstrated in our reference case that the evolution of the toroidal magnetic field includes the fast magnetic dissipation phase, the short duration of which can explain a significant part of the particle energy limit γ_{lim} .

5.1.2. The Effects of $\alpha_{B\phi} > -1$ and $f_{\text{mix}} < 1$

In our other simulations, we have explored the effects of three parameters: the pressure mixing ratio f_{mix} , the toroidal field index $\alpha_{B\phi}$, and the density contrast ξ_n . Figure 12 presents the time evolutions of the maximum particle energy γ_{max} : the left panel compares all $f_{\text{mix}} = 1$ cases (for different $\alpha_{B\phi}$ and ξ_n) and the right panel compares all $\alpha_{B\phi} = -1$ cases (for different f_{mix} and ξ_n). The reference simulation f1_α-1_ξ10 is displayed as the solid green line in each panel. The values of γ_{max} , as well as the simulation time t , have been scaled by the characteristic radius $R_{B\phi}$, which depends on $\alpha_{B\phi}$ (see Section 2). One can see that γ_{max} begins to increase significantly from its initial value after at least $ct/L \gtrsim R_{B\phi}/R_0$. For $f_{\text{mix}} = 1$, it typically shows a single phase of rapid growth to the energy limit γ_{lim} at rates corresponding to acceleration by electric fields $E_{\text{acc}} \sim (0.05\text{--}0.08)B_0$. In cases where γ_{lim} is exceeded, the further

increase of γ_{max} slows down significantly ($E_{\text{acc}} < 0.01B_0$ for $\alpha_{B\phi} = -1.5, -1$ and $\xi_n = 10$). The evolution of γ_{max} is more complex in the $f_{\text{mix}} < 1$ cases; in some of them, the γ_{lim} limit is reached in two stages, with E_{acc} only up to $\sim 0.02B_0$. The results for a high density contrast value of $\xi_n = 100$ suggest that the value of γ_{lim} is also relevant to those cases. Among the $\alpha_{B\phi} > -1$ cases, the rescaled $\gamma_{\text{max}}/(R_{B\phi}/R_0)$ reaches the γ_{lim} limit for $\alpha_{B\phi} = -0.5$, as well as for $\alpha_{B\phi} = 0$ and $\xi_n = 100$, although we cannot say whether it would flatten subsequently if these simulations could be continued. Particle acceleration appears to be faster for higher values of f_{mix} ; this is consistent with the correspondingly shorter instability growth timescales τ_{min} , as shown in Figure 7.

Figure 13 compares the particle momentum distributions between the simulations for $\alpha_{B\phi} = -1$ (hence $R_{B\phi} = R_0$), $\xi_n = 10$ (with one exception of $\xi_n = 100$), and different values of the pressure mixing parameter f_{mix} . This comparison is presented at two simulation times, because these simulations evolve at different rates. At $ct/L \simeq 2.5$, when some $f_{\text{mix}} = 1$ simulations are already in the slow acceleration phase while the $f_{\text{mix}} = 0.25$ case is just at the onset of fast acceleration, the high-energy distribution tails appear fairly regular (γ_{max} increases with increasing f_{mix}), even if they are very weak for $f_{\text{mix}} \leq 0.5$. At $ct/L \simeq 5$, when most simulations are in their final stages, the high-energy tails are clearly present for $f_{\text{mix}} \geq 0.25$ (in the case $f_{\text{mix}} = 0$, particle acceleration begins only after $ct/L = 5$), although they are rather irregular, with bumps instead of power laws. At $ct/L \simeq 5$, the fractions of particles contained in these high-energy tails are roughly $\simeq 1\%$ and they carry $\simeq 2\%$ of the total particle energy. The case of high density contrast $\xi_n = 100$ for $f_{\text{mix}} = 0.5$ at $ct/L \simeq 2.5$ shows significantly higher fractions: $\simeq 5\%$ of particles carrying $\simeq 14\%$ of particle energy.

Figure 14 compares the time evolutions of the toroidal magnetic flux $\Psi_{B\phi}$ (normalized to its initial value) for all

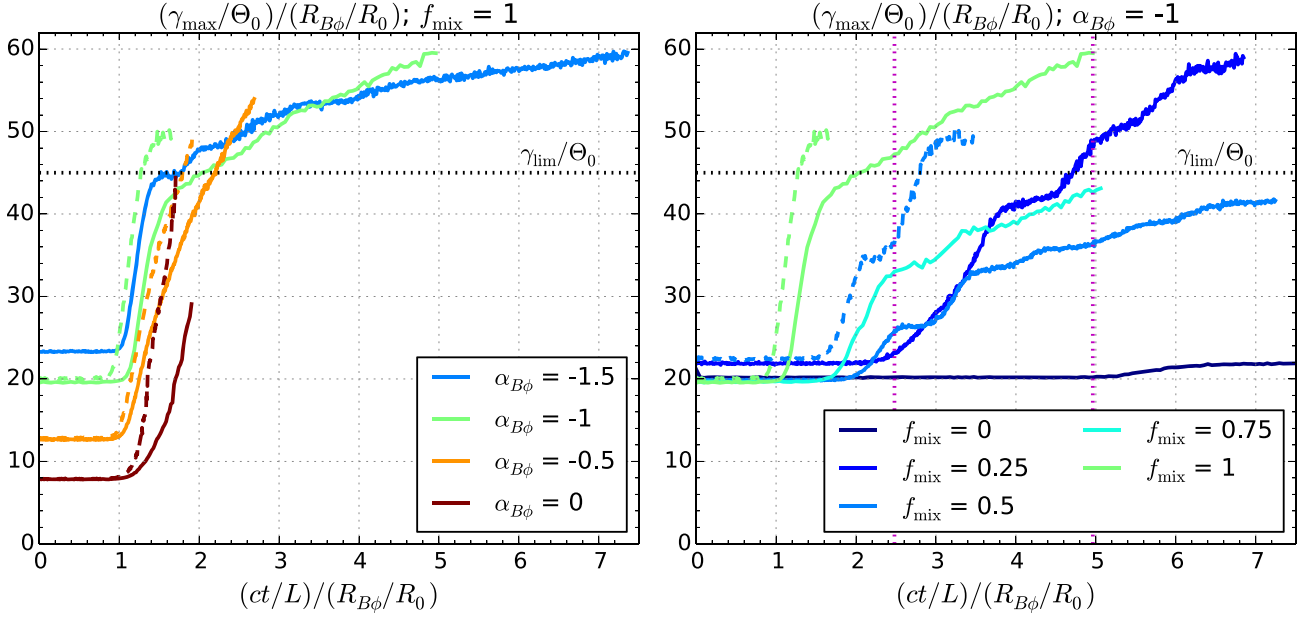


Figure 12. Time evolutions of the maximum particle energy γ_{\max} evaluated at the level of 10^{-4} of the $u^2 dN/du$ particle distributions normalized to peak at unity at $t = 0$. The results are compared for two series of simulations: the left panel shows simulations for $f_{\text{mix}} = 1$ and different values of $\alpha_{B\phi}$, and the right panel shows simulations for $\alpha_{B\phi} = -1$ and different values of f_{mix} . Both γ_{\max} and the simulation time t are scaled by the characteristic radius $R_{B\phi}$, which depends on $\alpha_{B\phi}$. The solid lines indicate the cases of $\xi_n = 10$, and the dashed lines indicate the cases of $\xi_n = 100$. The horizontal dotted black lines indicate the *confinement* energy limit $\gamma_{\text{lim}}/\Theta_0 \equiv R_0/\rho_0 = 45$. The vertical dotted magenta lines in the right panel indicate the times at which particle distributions are compared in Figure 13. The simulations are interrupted at different times, before the perturbations reach the x, y boundaries.

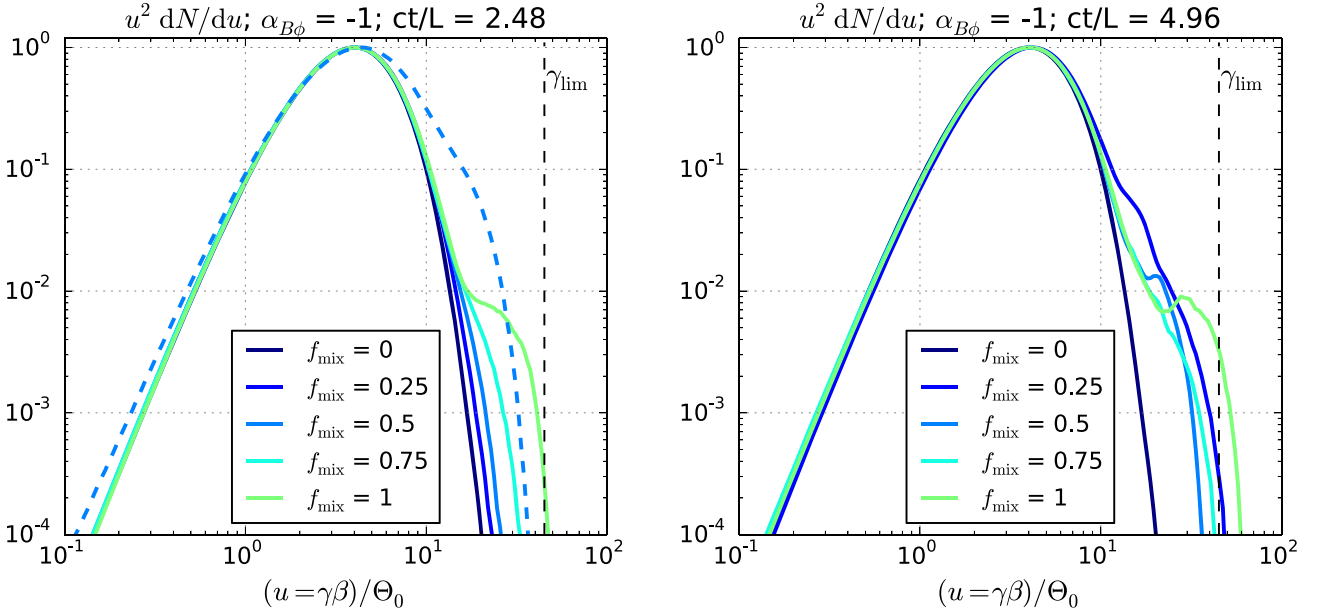


Figure 13. Particle momentum distributions $u^2 dN/du$ (combined for both electrons and positrons and normalized to peak at unity) compared at two moments in time (left/right panel) between simulations for $\alpha_{B\phi} = -1$, and different values of f_{mix} . The solid lines indicate the cases of $\xi_n = 10$, and the dashed lines indicate the cases of $\xi_n = 100$. The vertical black dashed lines indicate the *confinement* energy limit $\gamma_{\text{lim}} = 45\Theta_0$.

simulations. In all cases, we observe an initial period of almost constant $\Psi_{B\phi}$ followed by the onset of the fast magnetic dissipation phase, which in some cases is followed by a transition to a slow magnetic dissipation phase. The simulation time has been scaled by $R_{B\phi}$, such that for $f_{\text{mix}} = 1$ the fast magnetic dissipation phases begin roughly at $t \simeq (L/R_0)R_{B\phi}/c \simeq 20R_{B\phi}/c$. On the other hand, for $\alpha_{B\phi} = -1$, these onsets are delayed for the B_z -balanced cases of $f_{\text{mix}} < 1$. The overall relative decrease of $\Psi_{B\phi}$ is in the range of $\sim(30\text{--}60)\%$.

Transitions from the fast magnetic dissipation phase to the slow magnetic dissipation phase can be seen in most cases of $\alpha_{B\phi} \leq -1$ (although in some B_z -balanced cases the histories of $\Psi_{B\phi}(t)$ are more complicated). Such a transition is not seen in the cases of $\alpha_{B\phi} > -1$ (although there is a hint of that in the case f1_alpha-05_xi10). Comparing Figure 14 with Figure 12, a connection between the evolutions of γ_{\max} and $\Psi_{B\phi}$ can be noticed. Simulations in which $\gamma_{\max} \gg \gamma_{\text{lim}}$ are the same in which the fast magnetic dissipation phase is not

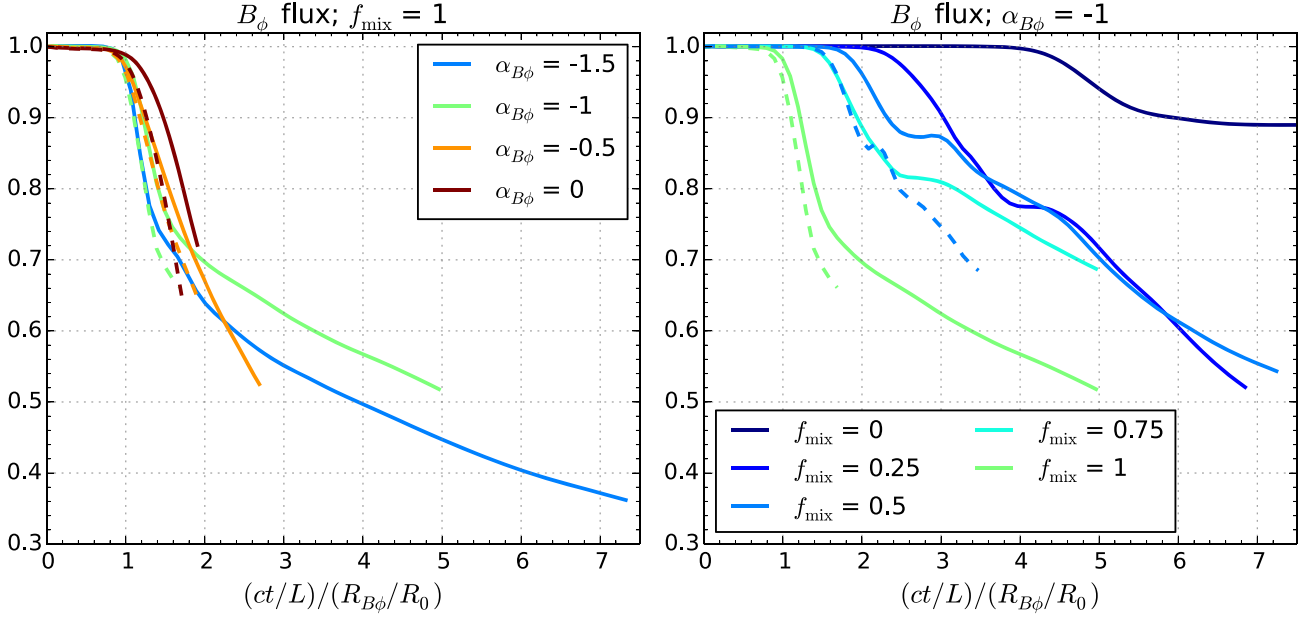


Figure 14. Time evolutions of the toroidal magnetic field flux Ψ_{B_ϕ} , normalized to unity at $t = 0$, compared for two series of simulations, using simulation time t scaled by the characteristic radius R_{B_ϕ} . The line types are the same as in Figure 12.

complete before the perturbations reach the boundaries and the simulation is interrupted. The episodes of rapid increase of γ_{\max} are simultaneous with a rapid decrease of Ψ_{B_ϕ} .

As an example, let us consider in more detail the case $f_{\text{mix}} = 1$, $\alpha_{B_\phi} = -0.5$, and $\xi_n = 100$ ($R_{B_\phi} = 1.55R_0$; the dashed orange lines in the left panels of Figures 12 and 14). In this case, the fast magnetic dissipation phase begins at $t \simeq 1.4L/c$ and lasts until the end of the simulation at $t \simeq 3.4L/c$. During that time, γ_{\max} increases linearly, reaching the level of $\gamma \simeq 90\theta_0 = 2\gamma_{\text{lim}}$. The right panels of Figure 3 show the time evolutions of the radial profiles of $\langle B_\phi \rangle(r)$ and $\langle E_z \rangle(r)$, extending until the simulation ends. The time separations between successive lines are $\Delta t \simeq 0.3L/c$, the same as for the reference simulation. Compared with the reference simulation, efficient dissipation of toroidal magnetic field progresses toward larger radii, essentially until it reaches the outer cutoff region. This corresponds to much more extended radial profiles of the net mean axial electric field $\langle E_z \rangle > 0$. The key difference from the reference case is that the axial electric field does not decay in the central core, settling at the value of $\langle E_z \rangle \sim 0.04B_0$ for $r < R_0$, which is four times higher than in the reference case. This is also reflected in the fact that dissipation of toroidal magnetic field in the central core proceeds to deeper levels. The e-folding growth timescale of $\langle E_z \rangle(R_0)$ has been estimated as $\tau_{E_z} \simeq 0.11L/c \simeq 2.2R_0/c$ over the period of $1.1 < ct/L < 1.7$, about 2.4 times longer than in the reference case. This means that, in this simulation, the fast magnetic dissipation phase lasts for at least $\simeq 18\tau_{E_z}$, which is longer in relation to τ_{E_z} than in the reference case.

Having a radially decreasing net axial electric field is key for efficient dissipation of the average toroidal magnetic field, which is governed by the Maxwell–Faraday equation:

$$\frac{\partial \langle B_\phi \rangle}{c \partial t} = \frac{\partial \langle E_z \rangle}{\partial r} < 0. \quad (10)$$

For example, the steepest radial gradients of the net axial electric field in both presented cases are $\Delta \langle E_z \rangle \simeq -0.04B_0$

over $\Delta r = R_0$, which corresponds to the peak magnetic dissipation rate of $\Delta \langle B_\phi \rangle / B_0 \simeq -0.8c\Delta t / L$. On the other hand, in the final state of the simulation f1_α-05_ξ100, we have $\Delta \langle E_z \rangle \simeq -0.045B_0$ over $\Delta r = 9R_0$, which yields $\Delta \langle B_\phi \rangle / B_0 \simeq -0.1c\Delta t / L$. These dissipation rates are consistent with the results presented in the top panels of Figure 3.

The right panels of Figure 11 show the acceleration history of an energetic positron (denoted as “pos #469”) in the simulation f1_α-05_ξ100. This particle accelerates almost linearly from $\gamma \simeq 0.3\gamma_{\text{lim}}$ at $t = 1.4L/c$ to $\gamma \simeq 1.75\gamma_{\text{lim}}$ at $t = 3.4L/c$, which means an energy gain of $\Delta\gamma \simeq 1.45\gamma_{\text{lim}}$ over the period of $\Delta t = 2L/c$. This acceleration is dominated by action of the axial electric field, which is sustained at the level of $E_z \simeq 0.04B_0$ throughout this time range. For most of the acceleration period (until $t \simeq 2.4L/c$), the particle is located within the central core ($r < R_0$), and its confinement indicator is $\xi_{\text{conf}} < 0.2$ even as it starts oscillating outside the core at later times. This particle is well-confined by the toroidal magnetic fields, and yet it is able to accelerate beyond γ_{lim} . Other energetic particles in this simulation reach $\xi_{\text{conf}} \simeq 0.6$, and yet they do not escape their confinement and keep accelerating.

5.2. Parallel versus Perpendicular Acceleration

We have addressed the problem of comparing the relative importance of parallel and perpendicular electric fields in particle acceleration by analyzing large samples of individually tracked particles, denoted with index i , for which we recorded as functions of simulation time their energy histories $\gamma_i(t)$, as well as the local magnetic and electric field vectors $\mathbf{B}_i(t)$, $\mathbf{E}_i(t)$. Out of these samples, we have selected *energetic particles* defined by two criteria: $\max[\gamma_i(t)] \geq 15\theta_0$ and $\max[\gamma_i(t)] - \min[\gamma_i(t)] \geq 10\theta_0$. Let $d\gamma_i(t) = (q_i/mc)(\boldsymbol{\beta}_i \cdot \mathbf{E}_i)(t) dt$ represent the instantaneous energy change of the i th particle between the times t and $t + dt$, where $q_i = \pm e$ is the particle charge. The corresponding contributions from perpendicular and parallel electric fields are $d\gamma_{i,\perp}(t) = (q_i/mc)(\boldsymbol{\beta}_i \cdot \mathbf{E}_{i,\perp})(t) dt$ and $d\gamma_{i,\parallel}(t) = (q_i/mc)(\boldsymbol{\beta}_i \cdot \mathbf{E}_{i,\parallel})(t) dt$, respectively. The total energy

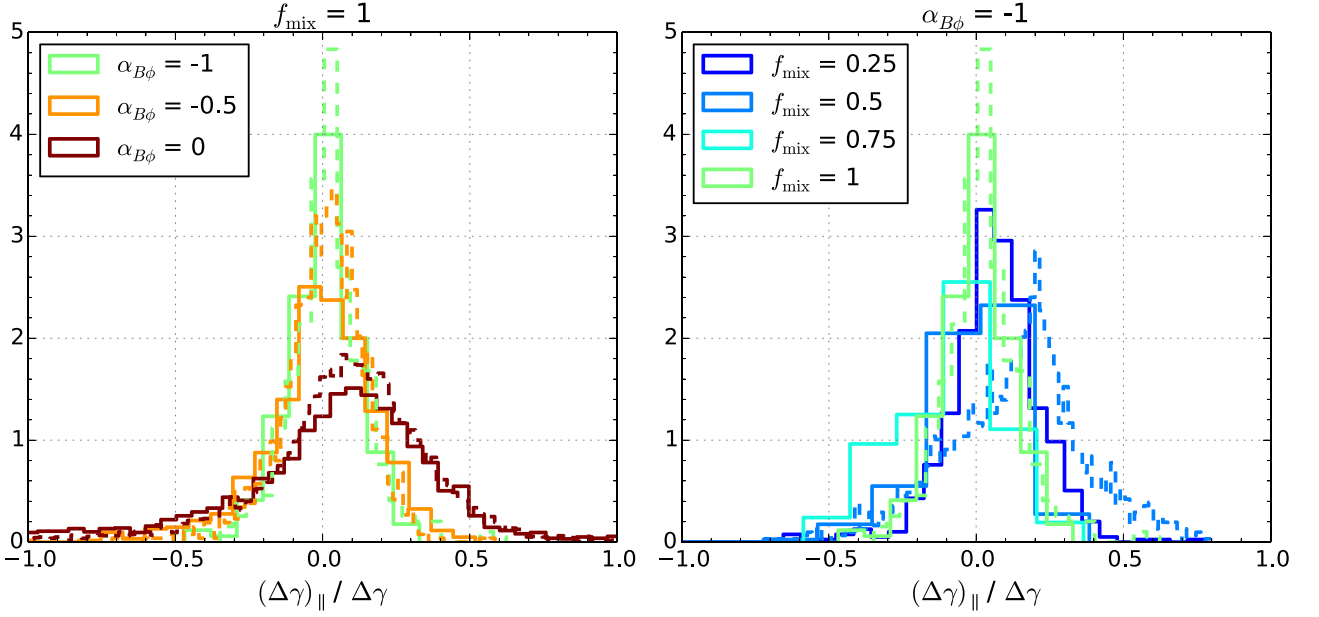


Figure 15. Distributions of the relative contribution $(\Delta\gamma)_{\parallel}$ of the electric field component E_{\parallel} parallel to the local magnetic field to the total energy gain $\Delta\gamma$ for complete samples of energetic particles. The line types are the same as in Figure 12.

gain of the i th particle has been calculated as $\Delta\gamma_i = \int_{t=0}^{t_{\text{peak},i}} d\gamma_i$, interrupting the integration at the moment $t_{\text{peak},i}$ at which the particle energy $\gamma_i(t)$ attains a global peak. The corresponding energy gains due to the perpendicular and parallel electric fields are $\Delta\gamma_{i,\perp} = \int_{t=0}^{t_{\text{peak},i}} d\gamma_{i,\perp}$ and $\Delta\gamma_{i,\parallel} = \int_{t=0}^{t_{\text{peak},i}} d\gamma_{i,\parallel}$, respectively.

Figure 15 compares the distributions of the $\Delta\gamma_{i,\parallel}/\Delta\gamma_i$ ratio for multiple simulations. In most cases, the distributions peak at $\Delta\gamma_{i,\parallel} \simeq 0$, which means that particle acceleration is dominated by perpendicular electric fields. However, in the f05_α-1_ξ100 case, the distribution peaks at $\Delta\gamma_{i,\parallel} \simeq 0.2\Delta\gamma_i$. Additional analysis of this case reveals various and complex histories of individual energetic particles that attain this level of parallel acceleration, an example of which will be presented further in this subsection. In the cases of $f_{\text{mix}} = 1$ and $\alpha_{B\phi} = 0$, the distributions of $\Delta\gamma_{i,\parallel}$ peak at $\simeq 0.1\Delta\gamma_i$. Here, the reason is the relatively long duration of the initial simulation phase when random fluctuations of electric field contribute roughly equally to $\Delta\gamma_{i,\parallel}$ and $\Delta\gamma_{i,\perp}$.

Figure 16 compares the relative contributions of perpendicular electric fields to the energization of particles as a function of simulation time for the cases of $\alpha_{B\phi} = -1$ with different values of f_{mix} and ξ_n . These contributions have been summed over the samples of energetic particles as $S_{\perp}(t) = \sum_i d\gamma_{i,\perp}^2(t)$ and $S_{\parallel}(t) = \sum_i d\gamma_{i,\parallel}^2(t)$ (summing over energy squares greatly reduces the noise), and the relative contribution has been calculated as $s_{\perp}(t) = S_{\perp}(t)/[S_{\perp}(t) + S_{\parallel}(t)]$. Initially, for $t \lesssim L/c$, before the fast magnetic dissipation phase, when particle energy changes are limited to small random fluctuations, we find $s_{\perp} \sim 0.5$. With the onset of the fast magnetic dissipation phase, the relative contribution of perpendicular acceleration increases to $s_{\perp} \sim 0.95$, followed by a slow irregular decrease to the level of $s_{\perp} \sim 0.6-0.8$. As far as we can say, these results are not sensitive to the density ratio ξ_n , but they seem to depend on the pressure mixing parameter f_{mix} in the nonlinear phase. For $4.0 < ct/L < 4.5$, when the $s_{\perp}(t)$ functions for $f_{\text{mix}} < 1$

achieve broad local minima, the highest relative contribution of perpendicular acceleration is $s_{\perp} \simeq 0.8$ for $f_{\text{mix}} = 0.25$, and the lowest is $s_{\perp} \simeq 0.6$ for $f_{\text{mix}} = 0.75$.¹⁴ This dependence appears to be driven by differences in S_{\perp} values (during that time, it is higher by a factor of $\simeq 5$ in the $f_{\text{mix}} = 0.25$ case, compared to the $f_{\text{mix}} = 0.75$ case), rather than by differences in S_{\parallel} values (higher by only $\simeq 50\%$ for the same comparison).

We have searched the sample of energetic particles in the simulation f05_α-1_ξ100 for an illustrative example of significant contribution of parallel electric fields. Figure 17 shows the acceleration history of an energetic positron (denoted as “pos #930” or with subscript “930”), which is characterized by an initial energy of $\gamma_{930,\text{ini}} \simeq 7.1\Theta_0$, and by $ct/L \simeq 3.5$ it reaches a peak energy of $\gamma_{930,\text{peak}} \simeq 25.9\Theta_0$, hence $\Delta\gamma_{930} \simeq 18.8\Theta_0 \simeq 0.42\gamma_{\text{lim}} \simeq 2.6\gamma_{930,\text{ini}}$, of which $\simeq 25\%$ is the contribution from parallel electric fields. Systematic acceleration by parallel electric fields with $\mathbf{E} \cdot \mathbf{B} \sim 0.005B_0^2$ is observed mainly in the period of $2.5 < ct/L < 2.95$.¹⁵ During this time, the total electric field strength at the position of this particle is $|\mathbf{E}| \sim (0.1-0.2)B_0 \sim (0.3-0.5)|\mathbf{B}|$. As it happens, these are not the strongest electric fields that this particle experiences. At $t \simeq 2.4L/c$, the corresponding values are $\mathbf{E} \cdot \mathbf{B} \simeq -0.008B_0^2$ and $|\mathbf{E}| \simeq 0.3B_0 \simeq 0.58|\mathbf{B}|$. At that time, our particle experiences rapid acceleration, but the contribution of parallel electric fields up to that point is not important.

Figure 18 provides a detailed context for the parallel acceleration of positron #930. This particle is located not far from the central axis ($r \simeq 1.5R_0$), within a large patch of positive $\mathbf{E} \cdot \mathbf{B}$. Additional analysis shows that this particle interacts with the same patch for the entire period of parallel acceleration while propagating along a helical trajectory (since the dominant magnetic field components are still B_z and B_{ϕ}). In the (x,y) plane following the particle along the z coordinate,

¹⁴ The case f05_α-1_ξ10 also achieves $s_{\perp} \simeq 0.6$, but only for $ct/L > 6$.

¹⁵ This period of time coincides with the second phase of rapid increase of the maximum particle energy γ_{max} in this simulation, taking it beyond the γ_{lim} limit (see the dashed blue line in the right panel of Figure 12).

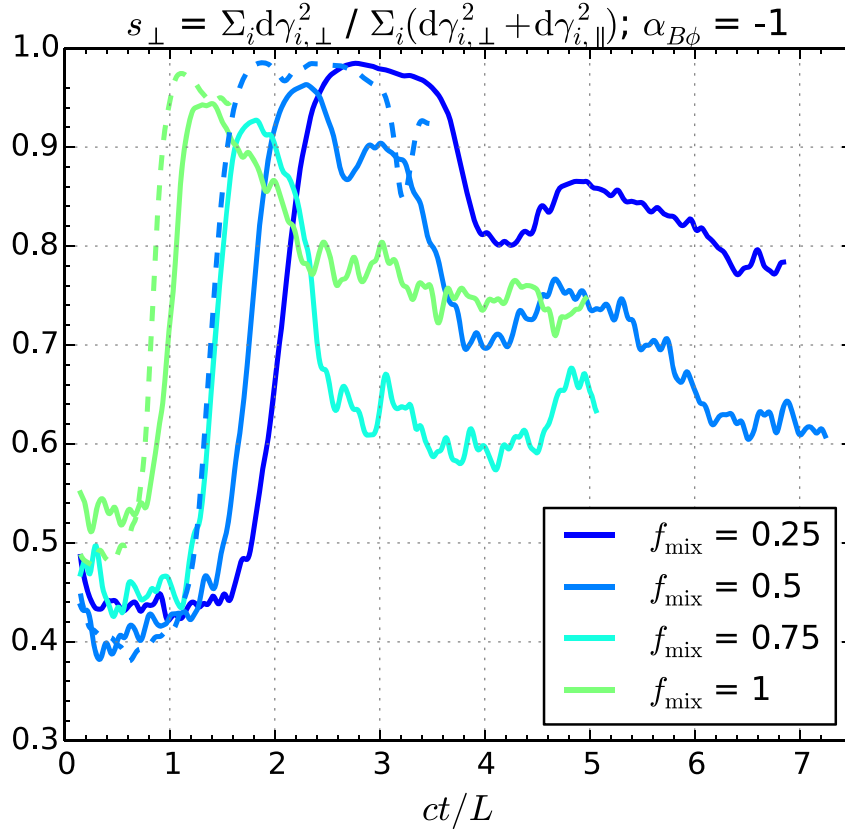


Figure 16. Relative contribution of perpendicular electric fields to the squared energy gains of energetic particles (using the formula shown in the plot title) as a function of simulation time for simulations with $\alpha_{B\phi} = -1$ and different values of f_{mix} (indicated by the line color) and ξ_n (indicated by the line type, same as in Figure 12).

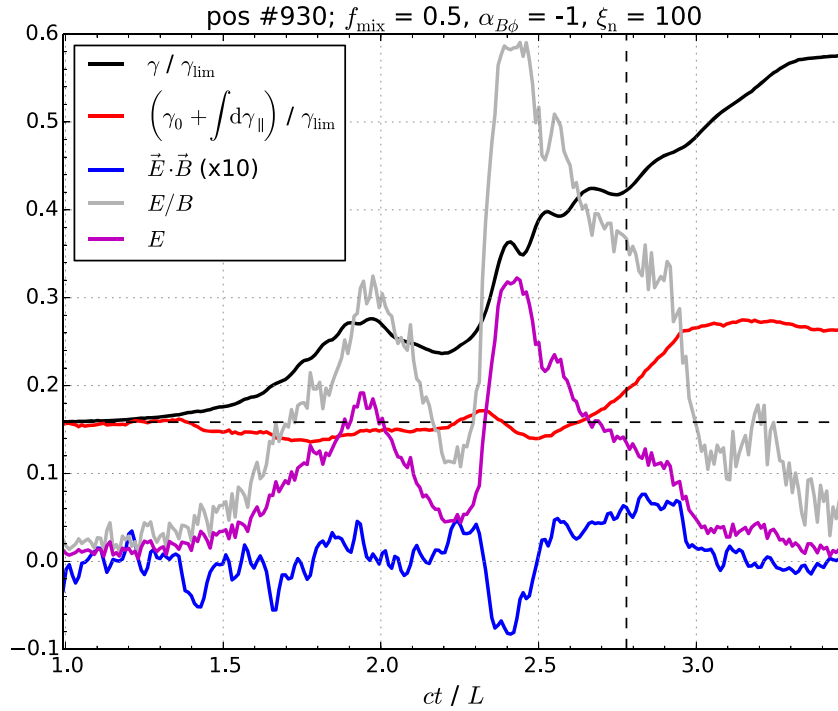


Figure 17. Acceleration history of the energetic positron #930 in the simulation f05_α-1_ξ100 that shows a significant contribution of parallel electric fields to its acceleration, with $\Delta\gamma_{i,\parallel} \simeq 0.25\Delta\gamma_i$. The black solid line shows the particle energy $\gamma_i(t)$, and the red solid line shows the integrated contribution of parallel electric fields $\gamma_i(t=0) + \int d\gamma_{i,\parallel}$, both normalized to γ_{lim} . The magenta, gray, and blue solid lines show the local values of $|\mathbf{E}|$, $|\mathbf{E}|/|\mathbf{B}|$, and $(\mathbf{E} \cdot \mathbf{B}) \times 10$, respectively. The vertical dashed line indicates the moment presented in Figure 18.

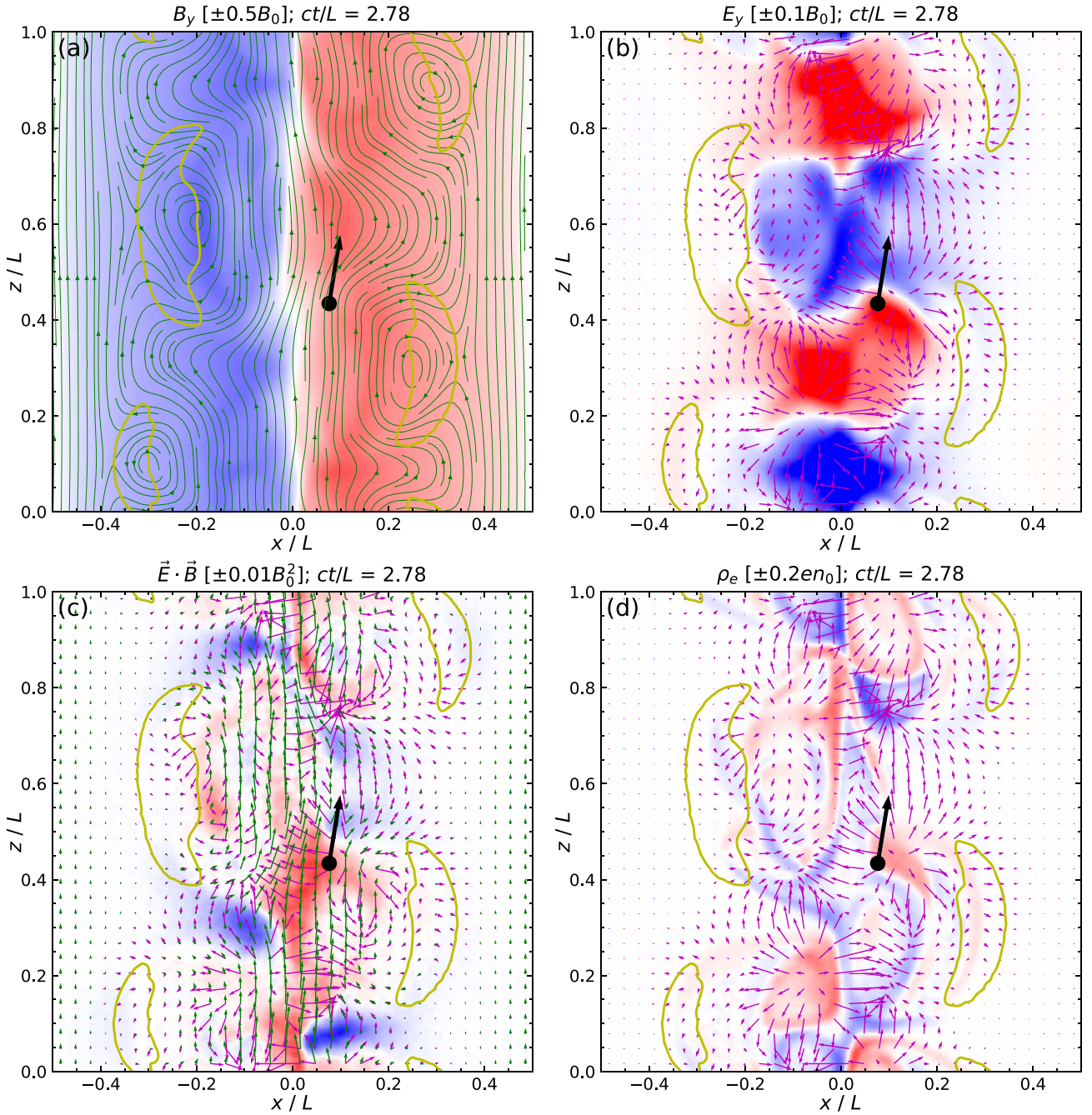


Figure 18. A snapshot from the simulation f05_α-1_ξ100 at the time $t = 2.78 L/c$, when the energetic positron #930 introduced in Figure 17 (marked with the black circles, with the black arrows indicating the in-plane velocity direction) experiences systematic acceleration by electric field parallel to the local magnetic field. Each panel shows an (x, z) map in the $y = 0$ plane, which also contains the energetic positron. The color maps (red is positive, blue is negative) show: (a) out-of-plane magnetic field component B_y , (b) out-of-plane electric field component E_y , (c) $\vec{E} \cdot \vec{B}$, and (d) charge density ρ_e . The magenta vector fields show the in-plane electric field (E_x, E_z), and the green vector field (panel (c)) shows the in-plane magnetic field (B_x, B_z). Panel (a) also includes a streamplot of (B_x, B_z) with solid green lines. The yellow contours indicate where $B_z = 0$.

the patch is seen to rotate around the central axis, and the particle motion appears to be synchronized with this rotation. The origin of that $\vec{E} \cdot \vec{B} > 0$ patch is discussed in Section 6.1.

5.3. Relation to Current Density and Electric Field Structures

We have considered the possible relation between acceleration of energetic particles and their location with respect to structures of current density and electric field. In general, this is

a very complex problem, because it requires characterizing a small sample of individual particles that succeed in achieving high energies by interacting with dynamical 3D electric fields and currents. We are attempting to illustrate this relation with only a few snapshots out of many that we have produced and examined.

Figure 19 presents single snapshots for two simulations (f025_α-1_ξ10 and f1_α-1_ξ100, chosen because they probe different values of f_{mix} and produce relatively large samples

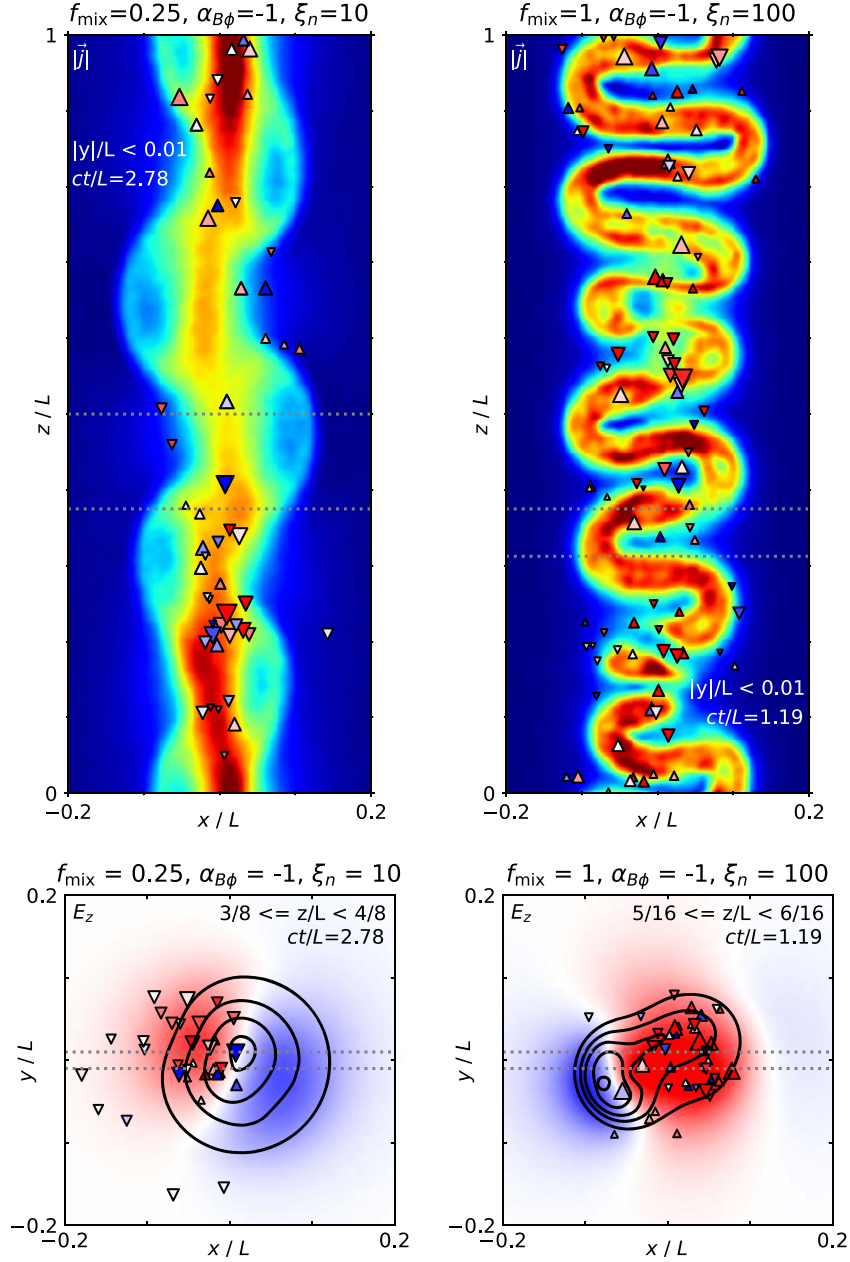


Figure 19. The *upper panels* show (x,z) maps of total current density $|j|$ (arbitrary units; the color scale is the same as in Figure 5) in the $y/L \simeq 0$ plane for the simulations f025_α-1_ξ10 (see the left panel of Figure 8) and f1_α-1_ξ100. The symbols indicate the positions of individual energetic particles: upward-pointing triangle represent the positrons, downward-pointing triangles represent the electrons, the sizes indicate the current particle energy, and the colors indicate the current particle energization rate (red means energy gain, blue means energy loss). The gray dotted lines indicate the range of z used for integrating the (x,y) maps shown below. The *lower panels* show (x,y) maps of axial electric field E_z (red means $E_z > 0$, blue means $E_z < 0$) averaged over the indicated range of z/L . The gray dotted lines indicate the range of y used for integrating the (x,z) maps shown above.

of energetic particles), each illustrated by an (x,z) map (in the $y/L \simeq 0$ plane) of total current density $|j|$, and by an (x,y) map (averaged over a range of z/L) of axial electric field E_z with overlaid contours of $|j|$. In all maps, we indicate the locations, energies, and acceleration rates of individual particles that are present in the probed volume regions and that are going to become energetic (according to the definition given in Section 5.2).

One question that we are attempting to address is whether there are thin current layers that could be sites of magnetic reconnection. We find in general that structures of current

density are not sharp on kinetic scales ($\sim \rho_0$). A particularly complex meandering (x,z) structure of $|j|$ can be seen in the f1_α-1_ξ100 simulation; it results from an initially cylindrical current core being sheared while retaining its initial thickness scale ($\sim R_0$).

Another question is whether the locations of energetic particles are correlated with these current density structures. We do not find any evidence for that. However, the (x,y) maps suggest that energetic particles are preferentially located in regions of $E_z > 0$ while avoiding regions of $E_z < 0$. We know already from Figure 8 that there is no symmetry between

regions of positive and negative E_z . The former ($E_z > 0$) dominate and are better connected, which allows local particles to spend more time in these acceleration zones. We thus find that the locations of particles undergoing successful acceleration are related more strongly to the structures of electric field, rather than current density.

6. Discussion

The first motivation for this project has been to bridge the diverse magnetic pinch configurations investigated recently with 3D kinetic numerical simulations: the Z-pinch case (with the toroidal magnetic fields balanced entirely by the gas pressure) studied by Alves et al. (2018, 2019) and the FF screw-pinch case (with the toroidal magnetic fields balanced entirely by the axial magnetic field) studied by Davelaar et al. (2020). To this end, we introduced the pressure mixing parameter f_{mix} such that $f_{\text{mix}} = 0$ corresponds to the FF screw-pinch limit, and $f_{\text{mix}} = 1$ corresponds to the Z-pinch limit. This allowed us to investigate the effect of f_{mix} for exactly the same radial profiles of toroidal magnetic field $B_\phi(r)$. In the case $f_{\text{mix}} = 0$, we have found particle acceleration to be inefficient, with γ_{max} increasing by only $\simeq 10\%$ (see Figure 12; note that this simulation ran until $t \simeq 15L/c$ without any further increase of γ_{max}). A key difference from the setup of Davelaar et al. (2020) is that they initialized the plasma as relativistically cold with $\Theta_0 = 10^{-2}$, and our plasma is initialized as relativistically hot with $\Theta_0 = 10^4$. In their simulations, particles reach Lorentz factors $\gamma \sim \sigma$ with magnetizations $\sigma \sim 10\text{--}40$. In our case $f_{\text{mix}} = 0$, we have peak magnetization of only $\sigma_{\text{hot}}(r=0) \simeq 2.8$, much less than the initial Maxwell–Jüttner value of $\gamma_{\text{max}}/\Theta_0 \simeq 20$; we think that this is the reason for the inefficient particle acceleration. Nevertheless, we achieve higher initial magnetizations (see the right panels of Figure 1), and hence efficient particle acceleration, in other cases. Already for $f_{\text{mix}} = 0.25$ (and higher), the most energetic particles achieve the Hillas-type energy limit γ_{lim} introduced by Alves et al. (2018).

Our second motivation has been to include a flexible power-law section in the radial profile of toroidal magnetic field $B_\phi(r)$. Both Alves et al. (2018, 2019) and Davelaar et al. (2020) investigated steeply decaying $B_\phi(r)$ profiles beyond the core radius R_0 . In the case of Alves et al. (2018, 2019), it was an exponential tail $B_\phi(r \gg R_0) \propto \exp(-r/R_0)$, and in the case of Davelaar et al. (2020), it was a family of profiles with approximately $\propto r^{-1}$ tails (see the left panel of Figure 1). In the Z-pinch limit ($f_{\text{mix}} = 1$), the analytical predictions of Begelman (1998) and Das & Begelman (2019) are that power-law profiles $B_\phi(r) \propto r^{\alpha_{B\phi}}$ should be locally unstable for $\alpha_{B\phi} > -1$. Such shallow-decay (or even flat) profiles of $B_\phi(r)$ have not been studied before by means of kinetic simulations.¹⁶

Despite the modest numerical scale separation of our simulations, we were able to confirm most of the previous results, especially those of Alves et al. (2018) in the Z-pinch limit—the structure of electric fields in the linear instability phase and the existence of the particle energy limit γ_{lim} . In the case of shallow $B_\phi(r)$ profiles ($\alpha_{B\phi} > -1$), this limit needs to be redefined to $(R_{B\phi}/R_0)\gamma_{\text{lim}}$, introducing a new characteristic radius $R_{B\phi}(\alpha_{B\phi}) > R_0$. In Section 2, we suggested preliminary

values of this radius: $R_{B\phi} \simeq 1.55R_0$ for $\alpha_{B\phi} = -0.5$, and $R_{B\phi} \simeq 2.5R_0$ for $\alpha_{B\phi} = 0$. However, our simulations for $\alpha_{B\phi} > -1$ had to be interrupted early, since the perturbations reached the domain boundaries before the fast magnetic dissipation phase and the associated particle acceleration were complete. Simulating a complete fast magnetic dissipation phase would require, e.g., shifting the outer cutoff to an intermediate radius.

We argue that the particle energy limit γ_{lim} should not be interpreted as resulting directly from particle confinement by toroidal magnetic fields, because we have not found any example of an energetic particle (out of 6×10^5 individually tracked particles per simulation), the acceleration of which would be interrupted by its escape from the inner radii. Efficient particle acceleration coincides with the fast magnetic dissipation phase, which in the cases of $\alpha_{B\phi} \leq -1$ is of well-defined duration, and is also confined to the inner region of $r \lesssim 2R_0$ (see Figures 3 and 5). However, in the cases of $\alpha_{B\phi} > -1$, magnetic dissipation can propagate to larger radii ($r > 2R_0$) and induce widespread and sustained electric fields.

In the most extreme Z-pinch case f1_α0_ξ100, which provides the highest magnetization in the outer regions, we find a weak signature of a local pinch mode at the intermediate radii of $(5\text{--}7)R_0 \simeq R_{\text{out}}/2$ (see Figure 5). This is the first numerical confirmation that the Z-pinch modes identified analytically by Begelman (1998) can be truly local in the sense that $k_z r_c \gg 1$ and $\sigma_r \ll r_c$ (for a mode centered at $r = r_c$ with radial dispersion σ_r ; this was predicted in the linear limit by Das & Begelman 2019). The fact that this mode has been identified in this particular case at these particular radii is consistent with the solutions of the local dispersion relation of Begelman (1998) presented in Figure 20 and described in Appendix B. That weak local mode is eventually dominated by a stronger pinch mode propagating outward from the central core region.

6.1. Parallel versus Perpendicular Acceleration

Particle acceleration by parallel electric fields in strongly magnetized jets with axial magnetic flux has been demonstrated by Davelaar et al. (2020), who attribute these fields to magnetic reconnection. They show examples of magnetic X-points in the (x, z) plane along the outer fronts of perturbation, where the axial magnetic field component is reversed on the perturbation side ($B_z < 0$), interacting with $B_z > 0$ in the unperturbed medium, as well as other magnetic irregularities in the (x, y) plane.

Such X-points can be seen clearly in our simulation f05_α-1_ξ100, where Figure 18(a) shows closed yellow contours in the (x, z) plane, along which $B_z = 0$, meaning that $B_z > 0$ outside (like in the entire domain in the initial configuration) and $B_z < 0$ inside. We also show using the `matplotlib.pyplot.streamplot` tool (which by default does not illustrate the field strength) that the inner (with respect to the central axis) sections of those contours include a magnetic O-point in the (x, z) plane, and the outer sections include a magnetic X-point, as has been shown by Davelaar et al. (2020). These magnetic X-points are potential sites of magnetic reconnection. Since the $B_y \equiv B_\phi$ component is smooth across the X-points (a finite guide field B_g), one would expect the reconnection-induced nonideal out-of-plane electric field to have a component parallel to the local magnetic field. However, Figure 18 shows that E_y is very weak along the outer sections of the $B_z = 0$ contours, and moreover, that $\mathbf{E} \cdot \mathbf{B}$ is also insignificant there, as compared

¹⁶ A “sinusoidal” profile of $B_\phi(r) \propto [1 - \cos(2\pi r/R_{\text{out}})]$ that was investigated with RMHD simulations by O’Neill et al. (2012) is included in the left panel of Figure 1. It has a symmetry similar to that of our case $\alpha_{B\phi} = 0$, but very different asymptotics at $r < R_0$.

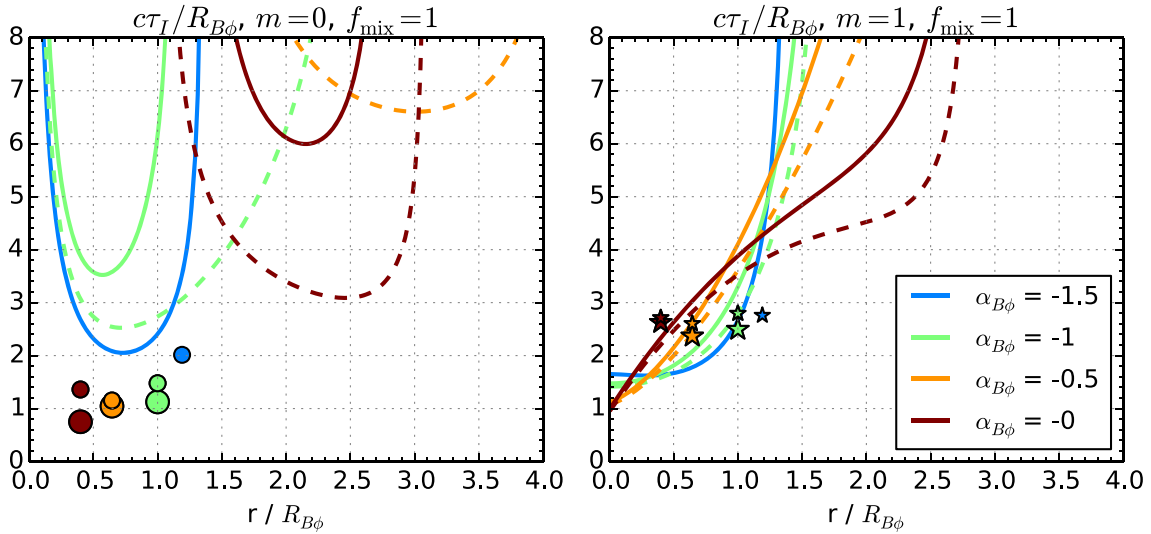


Figure 20. Growth timescales τ_I of the local instability modes for the initial configurations of the $f_{\text{mix}} = 1$ Z-pinch cases calculated according to the dispersion relation of Begelman (1998). The left panel shows the results for the $m = 0$ pinch mode, and the right panel shows the results for the $m = 1$ kink mode. The line colors indicate the value of $\alpha_{B\phi}$. The solid lines correspond to $\xi_n = 10$, and the dashed lines correspond to $\xi_n = 100$. Minimum growth timescales $c\tau_{\text{min}}/R_{B\phi}$ measured at the $1 < r/R_0 < 2$ shell region of our simulations are indicated at $r = R_0$ using the same symbols as in Figure 7 (the smaller symbols correspond to $\xi_n = 10$ and the larger ones to $\xi_n = 100$).

with the inner regions. We have also checked the total nonideal electric field $\mathbf{E}_{\text{nonid}}$ and the current density \mathbf{j} , finding that they are all very weak at the magnetic X-points. We therefore conclude that these magnetic X-points are not sites of active magnetic reconnection. Note that the relative strength of the reconnecting field component is $|B_z| \sim 0.2|B_\phi|$ inside the $B_z = 0$ contours, which corresponds to a very strong guide field of $B_g \sim 5|B_z|$, sufficient to suppress magnetic reconnection and particle acceleration (e.g., Dahlin et al. 2016; Werner & Uzdensky 2017, 2021).

Let us also discuss the origin of the positive $\mathbf{E} \cdot \mathbf{B}$ region that accelerates positron #930 in the nonlinear stage of simulation f05_α-1_ξ100, presented in Figure 18 and described in Section 4.2. Additional analysis reveals that nonzero $\mathbf{E} \cdot \mathbf{B}$ first appears during the saturation of the linear instability stage around $t \simeq 1.8L/c$, with positive $\mathbf{E} \cdot \mathbf{B}$ aligned with the deformed column of strong electric current, and with negative $\mathbf{E} \cdot \mathbf{B}$ outside that column. In this simulation, we also observe a second generation of the linear central instability, starting at $t \simeq 2.3L/c$, which is evidenced in the history of the energetic positron #930 (Figure 17) as a major increase of the total electric field following that moment. This second instability also generates the inner structures of charge density (within $-0.15 < x/L < 0.15$) that can be seen in the lower right panel of Figure 18. We conjecture that the centrally located patch of positive $\mathbf{E} \cdot \mathbf{B}$ seen for $2.5 < ct/L < 2.95$ results from the nonlinear saturation of the second-generation instability. The energetic positron #930 experiences the most efficient parallel acceleration because it happens to interact with that patch for as long as possible.

6.2. Instability Growth Timescales

In the FF case $f_{\text{mix}} = 0$, the measured minimum instability timescales τ_{min} reported in the right panel of Figure 7 can be compared with the analytical predictions of Appl et al. (2000). In the case of constant magnetic pitch $\mathcal{P}_0 = R_0$, the shortest growth timescale is theoretically predicted for the $|m| = 1$ kink mode: $c\tau/R_0 \simeq 7.52/\beta_A \simeq 8.78$, where $\beta_A \simeq 0.857$ is the

Alfvén velocity at $r = 0$ in our $f_{\text{mix}} = 0$ configuration. This is very close to our measurement of $c\tau/R_0 \simeq 8.45$.¹⁷ However, we also measure shorter timescales for the $m = 0$ and $m = 2$ modes in this case, which is inconsistent with the analytical predictions, according to which the pinch mode should be stable and the $m = 2$ mode should have a longer growth timescale (and a wavelength that would hardly fit in our domain). This suggests that the measured $m = 0$ and $m = 2$ modes are not linear, but instead they are secondary modes triggered nonlinearly by the linear kink mode. This interpretation is supported by the fact that the onsets of the $m = 0$ and $m = 2$ modes are delayed with respect to the onset of the kink mode, and this is actually evident in most other cases reported in Figure 6.

In the Z-pinch cases of $f_{\text{mix}} = 1$, the measured values of τ_{min} can be compared with the solutions of the local dispersion relation of Begelman (1998), reported in Figure 20 and described in Appendix B. Although the analytical solutions can be very steep functions of r , a fairly close agreement is found for the $m = 1$ kink mode between the measured values extracted from the $1 < r/R_0 < 2$ shell and the theoretical solutions evaluated at $r = R_0$. For the $m = 0$ pinch mode, the measured values are shorter than the theoretical solutions even for $\alpha_{B\phi} \leq -1$. This again suggests that only the kink mode measured in our simulations is linear.

6.3. Astrophysical Implications

The potential for development of instabilities due to toroidal magnetic field has been an important question in the theoretical picture of magnetized astrophysical jets.

The toroidal component of ordered magnetic fields is an essential ingredient of relativistic jets. As the jets are rooted in rotating structures (e.g., spinning black holes), toroidal fields are generated by azimuthal shearing of poloidal fields. These provide the magnetic pressure that accelerates the jet, and they

¹⁷ The corresponding analytical wavelength is $\simeq 8.43R_0$, very close to our effective wavelength of $\lambda_z \simeq 8.8R_0$ reported in Section 4.2.

carry the outgoing Poynting flux (e.g., Davis & Tchekhovskoy 2020). Toroidal fields provide a tension force that, in principle, would allow the jet to be collimated (pinched)¹⁸ and to maintain a structure of radially decreasing (away from the jet axis) total pressure and energy density (e.g., Begelman et al. 1984). In the lateral jet expansion, toroidal fields decay more slowly than poloidal fields, hence the pinching effect of toroidal fields can be expected to increase with distance along the jet (e.g., Bogovalov & Tsinganos 1999).

The relative importance of current-driven and pressure-driven modes in astrophysical jets depends crucially on the strength, lateral distribution, and evolution along the jet of the poloidal magnetic field. Davelaar et al. (2020) argued that FF configurations with significant poloidal fields are naturally expected in the relativistic jets emerging from the bulk-acceleration and collimation zone, protected from external modes by the lack of causal contact across the jet (Bromberg & Tchekhovskoy 2016; Tchekhovskoy & Bromberg 2016). Causality would be regained due to recollimation once the external pressure becomes important, and that would make FF jets unstable, at first to the current-driven modes.

It should be noted, however, that whether causality is lost in a relativistic jet depends on the scaling of external pressure P_{ext} with distance z along the jet. Porth & Komissarov (2015) showed that causality is lost only when $P_{\text{ext}}(z)$ is steeper than z^{-2} , and even in such cases the jet core can be pinched by toroidal magnetic field, triggering an internal instability.

In order for the Z-pinches to operate in jets, sufficient gas pressure needs to build up, presumably due to other heating mechanisms, e.g., internal shocks (e.g., Spada et al. 2001; Pjanka & Stone 2018), recollimation shocks (e.g., Bromberg & Levinson 2009; Nalewajko & Sikora 2009), magnetic reconnection due to global field reversals (e.g., Lovelace et al. 1997; Nalewajko et al. 2011; Giannios & Uzdensky 2019), or nonlinear saturation of the current-driven modes, in effect boosting their dissipation efficiency. Gas pressure can also be reduced by radiative cooling, especially in the jets hosted by powerful quasars and GRBs, or due to adiabatic expansion. This suggests that Z-pinches can only operate in the vicinity of gas pressure sources.

At any distance z along the jet, the strength of toroidal magnetic field must peak at some radius $R_{B\phi}$, which is intermediate when compared with the jet radius: $0 < R_{B\phi}(z) < R_j(z)$. Our study shows that the $R_{B\phi}(z)$ function is of considerable interest, because it largely determines the minimum growth timescale τ_{min} of the instabilities (see Figure 7). Let us then consider qualitatively the development of an initially FF jet—as it expands, internal pinching is expected to reduce the $R_{B\phi}/R_j$ ratio. In the FF jet core, the instability growth timescale is roughly $\tau(z) \sim 9R_{B\phi}(z)/c$; it would evolve much slower than the jet crossing timescale $R_j(z)/c$. It is then quite likely that this first instability will be able to evolve nonlinearly and to saturate. At this point, a fraction of the inner toroidal field will be dissipated, tending to increase $R_{B\phi}$, most likely in a fashion similar to the results shown in Figure 3 for two Z-pinch cases. Another effect of the first instability is generation of gas pressure, effectively increasing f_{mix} , so that the jet core is no longer FF. If the gas pressure is significant compared with the axial magnetic

pressure, it would reduce the instability growth timescale noticeably (Figure 7 shows that, for $f_{\text{mix}} = 0.25$, the growth timescale of the kink mode is already reduced by $\sim 40\%$ compared with the FF limit $f_{\text{mix}} = 0$). The overall outcome of this scenario depends on the relative importance of: (1) pinching of the jet core by outer toroidal fields, (2) dissipation of the inner toroidal fields, and (3) production of gas pressure. This problem should be addressed by future numerical simulations of initially FF jets with a significantly larger separation of scales L/R_0 .

We have also demonstrated numerically the presence of a weak pinch mode localized at intermediate radii in the case $f_{\text{mix}} = 1$ and $\alpha_{B\phi} = 0$, as predicted by Begelman (1998) and Das & Begelman (2019). Such local modes can operate in the outer jet regions even when their cores are relatively stable. In particular, flat $B_\phi(r)$ profiles, decreasing with r more slowly than r^{-1} ($\alpha_{B\phi} > -1$), would be susceptible to these modes. Such flat $B_\phi(r)$ profiles may develop in relativistic jets at large distances, as was found in global 3D RMHD simulations by Bromberg & Tchekhovskoy (2016).¹⁹

7. Conclusions

We have presented the results of 3D kinetic numerical simulations of cylindrical static jets with toroidal magnetic fields in relativistic pair plasma. Our simulations were initiated from configurations based on power-law profiles of $B_\phi(r) \propto r^{\alpha_{B\phi}}$, with the toroidal field index $-1.5 \leq \alpha_{B\phi} \leq 0$, modified by inner and outer cutoffs. The toroidal field was balanced by a combination of axial magnetic field $B_z(r)$ and gas pressure $P(r)$, whose relative importance was parameterized by the pressure mixing parameter $0 \leq f_{\text{mix}} \leq 1$, such that $f_{\text{mix}} = 0$ corresponds to the force-free screw-pinch case with uniform gas pressure, and $f_{\text{mix}} = 1$ corresponds to the Z-pinch case with $B_z(r) = 0$. The initial hot magnetizations were up to $\sigma_{\text{hot}} \simeq 8$ locally.

We found that all investigated cases were unstable, with the $m = 1$ kink mode being either dominant (for $f_{\text{mix}} < 1$) or comparable to the $m = 0$ pinch mode (for $f_{\text{mix}} = 1$). The minimum linear growth timescale τ_{min} for the kink mode in E_z , as well as the effective axial wavelength λ_z , were found to decrease systematically with increasing f_{mix} . In the case $f_{\text{mix}} = 1$ and $\alpha_{B\phi} = 0$, we have found a weak $m = 0$ pinch mode localized at intermediate radial distances, consistent with the local dispersion relation of Begelman (1998).

These instabilities are associated with dissipation of toroidal magnetic flux $\Psi_{B\phi}$, which typically proceeds in two phases: a fast magnetic dissipation phase followed by a slow one. The fast magnetic dissipation phase drives efficient particle acceleration. For shallow toroidal field profiles ($\alpha_{B\phi} \geq -0.5$), magnetic dissipation proceeds more slowly, and the fast magnetic dissipation phase is typically not complete before the perturbations reach the outer boundaries.

Particle acceleration is dominated by electric fields perpendicular to the local magnetic fields. Acceleration by parallel electric fields is possible in the central core region ($r < R_0$) in the presence of axial magnetic fields ($f_{\text{mix}} < 1$); however, strong guide fields suppress the efficiency of magnetic reconnection in the outer regions. While current density $|j|$ forms complex volumetric structures, we have not identified

¹⁸ Although, in the acceleration stage of relativistic jets, collimation by external pressure is more important in determining the final jet opening angle (Tchekhovskoy et al. 2010; Komissarov et al. 2010).

¹⁹ However, it appears that instability is suppressed in that case by a strong poloidal field (Das & Begelman 2019).

kinetically sharp current layers. For steep toroidal field profiles ($\alpha_{B\phi} \leq -1$), the most energetic particles reach the confinement energy limit $\gamma_{\text{lim}} = eB_0R_0/mc^2$. On the other hand, for shallow toroidal field profiles ($\alpha_{B\phi} \geq -0.5$), the most energetic particles approach a rescaled energy limit of $(R_{B\phi}/R_0)\gamma_{\text{lim}}$, where $R_{B\phi}$ is related to the peak radius of the initial $B_\phi(r)$ function ($R_{B\phi} = R_0$ for $\alpha_{B\phi} = -1$).

We have thus confirmed most of the results of previous kinetic simulations in the Z-pinch limit (Alves et al. 2018) and in the FF screw-pinch limit (Davelaar et al. 2020). These previous studies represent two special cases among many possible internal jet configurations. In contrast, our work is more general, as we have demonstrated how these previous results can be bridged by investigating the cases of mixed pressure balance. Thanks to the capabilities of the `Zeltron` code (Cerutti et al. 2013), this investigation can be extended to include the effect of radiative cooling due to synchrotron and inverse Compton processes on particle acceleration (Nalewajko et al. 2018; Werner et al. 2019; Zhdankin et al. 2020), and to calculate the radiative output including multiwavelength light curves and linear polarization (Yuan et al. 2016). This could potentially identify a unique signature of these instabilities in the vast observational data on blazars (e.g., Madejski & Sikora 2016), a subclass of AGNs dominated by nonthermal emission from relativistic jets.

These results are based on numerical simulations performed at the supercomputer `Prometheus` located at the Academic Computer Centre ‘‘Cyfronet’’ of the AGH University of Science and Technology in Krakow, Poland (PLGrid grants `pic19`, `plgpic20`, `plgpic21`, `ehtsim`); and at the computing cluster `Chuck` located at the Nicolaus Copernicus Astronomical Center of the Polish Academy of Sciences in Warsaw, Poland. This work was supported by the Polish National Science Centre grants 2015/18/E/ST9/00580 and 2021/41/B/ST9/04306, and by the U.S. National Science Foundation grants AST 1903335 and AST 1806084. B.M. acknowledges support from DOE through the LDRD program at LANL and from the NASA Astrophysics Theory Program.

Appendix A

Particle Confinement by Toroidal Magnetic Field

Consider a radial profile of toroidal magnetic field $B_\phi(r)$ in the form given by Equation (4), but without an outer cutoff. In the absence of electric fields, a relativistic particle of mass m , charge $q = \pm e$, constant Lorentz factor $\gamma \gg 1$, dimensionless velocity $\boldsymbol{\beta} = \mathbf{v}/c = [\beta_r, \beta_\phi, \beta_z]$ (parameterized as $\beta_r \simeq \sin \theta$, $\beta_\phi = 0$, $\beta_z \simeq \cos \theta \equiv \mu$), and momentum $\mathbf{p} = \gamma\boldsymbol{\beta}mc$ would propagate under the Lorentz force $d\mathbf{p}/dt = q(\boldsymbol{\beta} \times \mathbf{B}) = qB_\phi(r)[- \cos \theta, 0, \sin \theta]$. Noting that $d\mathbf{p}/dt = \gamma mc(d\boldsymbol{\beta}/dt) = \gamma mc^2\beta_r(d\boldsymbol{\beta}/dr) = \gamma mc^2\beta_r[\cos$ and $d\mu/dr = -\sin \theta(d\theta/dr)$, the particle trajectory can be described by the equation

$$\frac{d\mu}{d(r/R_0)} = \pm \left(\frac{\gamma}{\gamma_{\text{lim}}} \right)^{-1} \frac{B_\phi(r)}{B_0}, \quad (\text{A1})$$

where $\gamma_{\text{lim}} = eB_0R_0/(mc^2)$. For $\alpha_{B\phi} = -1$, this equation can be solved analytically, yielding

$$\mu(r) = \mu_0 \pm \frac{1}{2} \left(\frac{\gamma}{\gamma_{\text{lim}}} \right)^{-1} \ln \left[1 + \left(\frac{r}{R_0} \right)^2 \right], \quad (\text{A2})$$

where $\mu_0 = \mu(r=0)$. In the specific case $q = +e$ (a positron), the maximum radius r_{max} is given by $\mu(r_{\text{max}}) = 1$. If we adopt a confinement criterion $r_{\text{max}} < r_{\text{conf}}$, this can be expressed as

$$\gamma - u_{z,0} < \frac{\gamma_{\text{lim}}}{2} \ln \left[1 + \left(\frac{r_{\text{conf}}}{R_0} \right)^2 \right], \quad (\text{A3})$$

where $u_{z,0} \simeq \gamma\mu_0$ is the axial four-velocity component at $r=0$. This criterion simplifies to $\gamma - u_{z,0} < \gamma_{\text{lim}}$ for $r_{\text{conf}} \simeq 2.53R_0$, which is a reasonable threshold. Note that γ_{lim} is relevant as the confinement energy limit only for particles with $u_{z,0} \simeq 0$, i.e., crossing the symmetry axis at the right angle. Particles propagating along the axis can reach energies beyond γ_{lim} without escaping. For analysis of acceleration histories of individual particles, we introduce the *particle confinement indicator* defined as $\xi_{\text{conf}} = (\gamma - |u_z|)/\gamma_{\text{lim}}$, so that a particle is considered confined if $\xi_{\text{conf}} < 1$.

Appendix B

Linear Growth Timescales in the Z-pinch Cases

Instability growth timescales in the $f_{\text{mix}} = 1$ Z-pinch cases can be calculated analytically using the local dispersion relation expressed by Eq. (3.32) of Begelman (1998) in the limit of $B_z = 0$ and $l \ll k$ (negligible radial wavenumber). The dispersion relation is solved for the initial equilibria used in our simulations as a function of radius r . Figure 20 presents the resulting exponential growth timescales $\tau_1 = 1/\omega_1$ for the $m=0$ pinch and $m=1$ kink modes scaled by the characteristic radius $R_{B\phi}$. Higher azimuthal modes are found to be stable in all considered cases. All configurations are unstable to the kink mode with the shortest growth timescales ($c\tau_1/R_{B\phi} \sim 1.0\text{--}1.6$) found within $r < R_{B\phi}$. For $\alpha_{B\phi} > -1$, the unstable region extends toward intermediate radii, up to $r \simeq 2.5R_{B\phi}$ for the case `f1_alpha_0_xi100`, but with significantly longer growth timescales. The solutions are more diverse for the pinch mode—the central core region is found to be unstable only for $\alpha_{B\phi} \leq -1$, and for $\alpha_{B\phi} > -1$ a distinct instability region is located at intermediate radii. In the case `f1_alpha_0_xi100`, the pinch mode shows a growth timescale of $c\tau_1/R_{B\phi} \simeq 3$ at $r = 2.5R_{B\phi}$, which is shorter than the local growth timescale for the kink mode, but longer than that for the kink mode at the central core.

ORCID iDs

José Ortuño-Macías  <https://orcid.org/0000-0002-9463-3137>
 Krzysztof Nalewajko  <https://orcid.org/0000-0002-2019-9438>

Dmitri A. Uzdensky  <https://orcid.org/0000-0001-8792-6698>

Mitchell C. Begelman  <https://orcid.org/0000-0003-0936-8488>

Gregory R. Werner  <https://orcid.org/0000-0001-9039-9032>

Alexander Y. Chen  <https://orcid.org/0000-0002-4738-1168>

Bhupendra Mishra  <https://orcid.org/0000-0003-0271-3429>

References

- Abdo, A. A., Ackermann, M., Ajello, M., et al. 2011, *Sci*, **331**, 739
- Alves, E. P., Zrake, J., & Fiuza, F. 2018, *PhRvL*, **121**, 245101
- Alves, E. P., Zrake, J., & Fiuza, F. 2019, *PhPI*, **26**, 072105
- Appl, S., Lery, T., & Baty, H. 2000, *A&A*, **355**, 818
- Begelman, M. C. 1998, *ApJ*, **493**, 291
- Begelman, M. C., Blandford, R. D., & Rees, M. J. 1984, *RvMP*, **56**, 255
- Begelman, M. C., & Li, Z.-Y. 1994, *ApJ*, **426**, 269
- Beskin, V. S., & Nokhrina, E. E. 2006, *MNRAS*, **367**, 375
- Bodo, G., Mamatsashvili, G., Rossi, P., et al. 2013, *MNRAS*, **434**, 3030
- Bodo, G., Mamatsashvili, G., Rossi, P., et al. 2019, *MNRAS*, **485**, 2909
- Bodo, G., Mamatsashvili, G., Rossi, P., et al. 2022, *MNRAS*, **510**, 2391
- Bogovalov, S., & Tsinganos, K. 1999, *MNRAS*, **305**, 211
- Bromberg, O., & Levinson, A. 2009, *ApJ*, **699**, 1274
- Bromberg, O., Singh, C. B., Davelaar, J., et al. 2019, *ApJ*, **884**, 39
- Bromberg, O., & Tchekhovskoy, A. 2016, *MNRAS*, **456**, 1739
- Cerutti, B., Werner, G. R., Uzdensky, D. A., & Begelman, M. C. 2013, *ApJ*, **770**, 147
- Dahlin, J. T., Drake, J. F., & Swisdak, M. 2016, *PhPI*, **23**, 120704
- Das, U., & Begelman, M. C. 2019, *MNRAS*, **482**, 2107
- Davelaar, J., Philippov, A. A., Bromberg, O., et al. 2020, *ApJL*, **896**, L31
- Davis, S. W., & Tchekhovskoy, A. 2020, *ARA&A*, **58**, 407
- Drenkhahn, G., & Spruit, H. C. 2002, *A&A*, **391**, 1141
- Esirkepov, T. Z. 2001, *CoPhC*, **135**, 144
- Freidberg, J. P. 1982, *RvMP*, **54**, 801
- Giannios, D., & Spruit, H. C. 2006, *A&A*, **450**, 887
- Giannios, D., & Uzdensky, D. A. 2019, *MNRAS*, **484**, 1378
- Hillas, A. M. 1984, *ARA&A*, **22**, 425
- Istomin, Y. N., & Pariev, V. I. 1994, *MNRAS*, **267**, 629
- Kadomtsev, B. B. 1966, *RvPP*, **2**, 153
- Kirk, J. G. 2004, *PhRvL*, **92**, 181101
- Komissarov, S. S., Barkov, M. V., Vlahakis, N., et al. 2007, *MNRAS*, **380**, 51
- Komissarov, S. S., Vlahakis, N., & Königl, A. 2010, *MNRAS*, **407**, 17
- Kruskal, M., & Schwarzschild, M. 1954, *RSPSA*, **223**, 348
- Li, Z.-Y., Chiueh, T., & Begelman, M. C. 1992, *ApJ*, **394**, 459
- Lovelace, R. V. E., Newman, W. I., & Romanova, M. M. 1997, *ApJ*, **484**, 628
- Lyubarskii, Y. E. 1996, *A&A*, **311**, 172
- Lyubarskii, Y. E. 1999, *MNRAS*, **308**, 1006
- Madejski, G. M., & Sikora, M. 2016, *ARA&A*, **54**, 725
- McKinney, J. C., & Blandford, R. D. 2009, *MNRAS*, **394**, L126
- Michel, F. C. 1971, *CoASP*, **3**, 80
- Mignone, A., Rossi, P., Bodo, G., et al. 2010, *MNRAS*, **402**, 7
- Mignone, A., Striani, E., Tavani, M., et al. 2013, *MNRAS*, **436**, 1102
- Mizuno, Y., Hardee, P. E., & Nishikawa, K.-I. 2011b, *ApJ*, **734**, 19
- Mizuno, Y., Hardee, P. E., & Nishikawa, K.-I. 2014, *ApJ*, **784**, 167
- Mizuno, Y., Lyubarsky, Y., Nishikawa, K.-I., et al. 2012, *ApJ*, **757**, 16
- Mizuno, Y., Lyubarsky, Y., Nishikawa, K.-I., & Hardee, P. E. 2009, *ApJ*, **700**, 684
- Mizuno, Y., Lyubarsky, Y., Nishikawa, K.-I., & Hardee, P. E. 2011a, *ApJ*, **728**, 90
- Moll, R., Spruit, H. C., & Obergaulinger, M. 2008, *A&A*, **492**, 621
- Mukherjee, D., Bodo, G., Rossi, P., et al. 2021, *MNRAS*, **505**, 2267
- Nakamura, M., & Meier, D. L. 2004, *ApJ*, **617**, 123
- Nalewajko, K., & Begelman, M. C. 2012, *MNRAS*, **427**, 2480
- Nalewajko, K., Giannios, D., Begelman, M. C., et al. 2011, *MNRAS*, **413**, 333
- Nalewajko, K., & Sikora, M. 2009, *MNRAS*, **392**, 1205
- Nalewajko, K., Yuan, Y., & Chruślińska, M. 2018, *JPIPh*, **84**, 755840301
- Narayan, R., Igumenshchev, I. V., & Abramowicz, M. A. 2003, *PASJ*, **55**, L69
- Narayan, R., Li, J., & Tchekhovskoy, A. 2009, *ApJ*, **697**, 1681
- O'Neill, S. M., Beckwith, K., & Begelman, M. C. 2012, *MNRAS*, **422**, 1436
- Pjanka, P., & Stone, J. M. 2018, *MNRAS*, **477**, 2376
- Porth, O., & Komissarov, S. S. 2015, *MNRAS*, **452**, 1089
- Porth, O., Komissarov, S. S., & Keppens, R. 2014, *MNRAS*, **438**, 278
- Puzzoni, E., Mignone, A., & Bodo, G. 2021, *MNRAS*, **508**, 2771
- Romanova, M. M., & Lovelace, R. V. E. 1992, *A&A*, **262**, 26
- Singh, C. B., Mizuno, Y., & de Gouveia Dal Pino, E. M. 2016, *ApJ*, **824**, 48
- Sironi, L., Petropoulou, M., & Giannios, D. 2015, *MNRAS*, **450**, 183
- Spada, M., Ghisellini, G., Lazzati, D., & Celotti, A. 2001, *MNRAS*, **325**, 1559
- Tavani, M., Bulgarelli, A., Vittorini, V., et al. 2011, *Sci*, **331**, 736
- Tchekhovskoy, A., & Bromberg, O. 2016, *MNRAS*, **461**, L46
- Tchekhovskoy, A., McKinney, J. C., & Narayan, R. 2009, *ApJ*, **699**, 1789
- Tchekhovskoy, A., Narayan, R., & McKinney, J. C. 2010, *NewA*, **15**, 749
- Tomimatsu, A., Matsuoka, T., & Takahashi, M. 2001, *PhRvD*, **64**, 123003
- Uzdensky, D. A., Cerutti, B., & Begelman, M. C. 2011, *ApJL*, **737**, L40
- Vay, J.-L. 2008, *PhPI*, **15**, 056701
- Werner, G. R., Philippov, A. A., & Uzdensky, D. A. 2019, *MNRAS*, **482**, L60
- Werner, G. R., & Uzdensky, D. A. 2017, *ApJL*, **843**, L27
- Werner, G. R., & Uzdensky, D. A. 2021, *JPIPh*, **87**, 905870613
- Werner, G. R., Uzdensky, D. A., Begelman, M. C., et al. 2018, *MNRAS*, **473**, 4840
- Werner, G. R., Uzdensky, D. A., Cerutti, B., et al. 2016, *ApJL*, **816**, L8
- Yuan, Y., Nalewajko, K., Zrake, J., et al. 2016, *ApJ*, **828**, 92
- Zhdankin, V., Uzdensky, D. A., Werner, G. R., et al. 2020, *MNRAS*, **493**, 603

Bibliography

- A. A. Abdo et al. Fermi Observations of TeV-Selected Active Galactic Nuclei. *ApJ*, 707(2):1310–1333, Dec. 2009. doi: 10.1088/0004-637X/707/2/1310.
- F. Acero et al. Fermi Large Area Telescope Third Source Catalog. *ApJs*, 218(2):23, June 2015. doi: 10.1088/0067-0049/218/2/23.
- F. Aharonian et al. An Exceptional Very High Energy Gamma-Ray Flare of PKS 2155-304. *ApJL*, 664(2):L71–L74, Aug. 2007. doi: 10.1086/520635.
- M. L. Ahnen et al. Long-term multi-wavelength variability and correlation study of Markarian 421 from 2007 to 2009. *A&A*, 593:A91, Sept. 2016. doi: 10.1051/0004-6361/201628447.
- E. P. Alves, J. Zrake, and F. Fiuza. Efficient Nonthermal Particle Acceleration by the Kink Instability in Relativistic Jets. *Phys. Rev. Lett.*, 121(24):245101, Dec. 2018. doi: 10.1103/PhysRevLett.121.245101.
- J. R. P. Angel and H. S. Stockman. Optical and infrared polarization of active extragalactic objects. *Annual Review of Astronomy and Astrophysics*, 18:321–361, Jan. 1980. doi: 10.1146/annurev.aa.18.090180.001541.
- E. Angelakis et al. RoboPol: the optical polarization of gamma-ray-loud and gamma-ray-quiet blazars. *MNRAS*, 463(3):3365–3380, Dec. 2016. doi: 10.1093/mnras/stw2217.
- S. Appl, T. Lery, and H. Baty. Current-driven instabilities in astrophysical jets. Linear analysis. *A&A*, 355:818–828, Mar. 2000.
- K. Asada, M. Nakamura, A. Doi, H. Nagai, and M. Inoue. Discovery of Sub- to Superluminal Motions in the M87 Jet: An Implication of Acceleration from Sub-relativistic to Relativistic Speeds. *ApJL*, 781(1):L2, Jan. 2014. doi: 10.1088/2041-8205/781/1/L2.
- G. Bateman. *MHD instabilities*. 1978.
- V. Beckmann and C. Shrader. The AGN phenomenon: open issues. In *Proceedings of “An INTEGRAL view of the high-energy sky (the first 10 years)” - 9th INTEGRAL Workshop and celebration of the 10th anniversary of the launch (INTEGRAL 2012). 15-19 October 2012. Bibliotheque Nationale de France*, page 69, Jan. 2012.
- M. C. Begelman. Instability of Toroidal Magnetic Field in Jets and Plerions. *ApJ*, 493(1):291–300, Jan. 1998. doi: 10.1086/305119.

- M. C. Begelman and Z.-Y. Li. Asymptotic Domination of Cold Relativistic MHD Winds by Kinetic Energy Flux. *ApJ*, 426:269, May 1994. doi: 10.1086/174061.
- M. C. Begelman, R. D. Blandford, and M. J. Rees. Theory of extragalactic radio sources. *Reviews of Modern Physics*, 56(2):255–351, Apr. 1984. doi: 10.1103/RevModPhys.56.255.
- M. C. Begelman, A. C. Fabian, and M. J. Rees. Implications of very rapid TeV variability in blazars. *MNRAS*, 384(1):L19–L23, Feb. 2008. doi: 10.1111/j.1745-3933.2007.00413.x.
- I. B. Bernstein, E. A. Frieman, M. D. Kruskal, and R. M. Kulsrud. An Energy Principle for Hydro-magnetic Stability Problems. *Proceedings of the Royal Society of London Series A*, 244(1236):17–40, Feb. 1958. doi: 10.1098/rspa.1958.0023.
- C. K. Birdsall and A. B. Langdon. *Plasma Physics via Computer Simulation*. 1991.
- J. A. Biretta, W. B. Sparks, and F. Macchetto. Hubble Space Telescope Observations of Superluminal Motion in the M87 Jet. *ApJ*, 520(2):621–626, Aug. 1999. doi: 10.1086/307499.
- R. Blandford and D. Eichler. Particle acceleration at astrophysical shocks: A theory of cosmic ray origin. *Physics Reports*, 154(1):1–75, Oct. 1987. doi: 10.1016/0370-1573(87)90134-7.
- R. Blandford, D. Meier, and A. Readhead. Relativistic Jets from Active Galactic Nuclei. *Annual Review of Astronomy and Astrophysics*, 57:467–509, Aug. 2019. doi: 10.1146/annurev-astro-081817-051948.
- R. D. Blandford and D. G. Payne. Hydromagnetic flows from accretion disks and the production of radio jets. *MNRAS*, 199:883–903, June 1982. doi: 10.1093/mnras/199.4.883.
- R. D. Blandford and R. L. Znajek. Electromagnetic extraction of energy from Kerr black holes. *MNRAS*, 179:433–456, May 1977. doi: 10.1093/mnras/179.3.433.
- M. Błażejowski, M. Sikora, R. Moderski, and G. M. Madejski. Comptonization of Infrared Radiation from Hot Dust by Relativistic Jets in Quasars. *ApJ*, 545(1):107–116, Dec. 2000. doi: 10.1086/317791.
- G. R. Blumenthal and R. J. Gould. Bremsstrahlung, Synchrotron Radiation, and Compton Scattering of High-Energy Electrons Traversing Dilute Gases. *Reviews of Modern Physics*, 42(2):237–271, Jan. 1970. doi: 10.1103/RevModPhys.42.237.
- J. P. Boris. Relativistic plasma simulation-optimization of a hybrid code. *In Proc. Fourth Conf. Num. Sim. Plasmas*, pages 3–67, 1970.
- O. Bromberg, C. B. Singh, J. Davelaar, and A. A. Philippov. Kink Instability: Evolution and Energy Dissipation in Relativistic Force-free Nonrotating Jets. *ApJ*, 884(1):39, Oct. 2019. doi: 10.3847/1538-4357/ab3fa5.
- R. Buehler et al. Gamma-Ray Activity in the Crab Nebula: The Exceptional Flare of 2011 April. *ApJ*, 749(1):26, Apr. 2012. doi: 10.1088/0004-637X/749/1/26.
- B. Cerutti and G. Werner. The zeltron code project, 2013. URL <https://ipag.osug.fr/~ceruttbe/Zeltron/index.html>.

- B. Cerutti, G. R. Werner, D. A. Uzdensky, and M. C. Begelman. Simulations of Particle Acceleration beyond the Classical Synchrotron Burnoff Limit in Magnetic Reconnection: An Explanation of the Crab Flares. *ApJ*, 770(2):147, June 2013. doi: 10.1088/0004-637X/770/2/147.
- B. Cerutti, G. R. Werner, D. A. Uzdensky, and M. C. Begelman. Three-dimensional Relativistic Pair Plasma Reconnection with Radiative Feedback in the Crab Nebula. *ApJ*, 782(2):104, Feb. 2014. doi: 10.1088/0004-637X/782/2/104.
- C. C. Cheung, D. E. Harris, and Ł. Stawarz. Superluminal Radio Features in the M87 Jet and the Site of Flaring TeV Gamma-Ray Emission. *ApJL*, 663(2):L65–L68, July 2007. doi: 10.1086/520510.
- I. M. Christie, M. Petropoulou, L. Sironi, and D. Giannios. Radiative signatures of plasmoid-dominated reconnection in blazar jets. *MNRAS*, 482(1):65–82, Jan. 2019. doi: 10.1093/mnras/sty2636.
- L. Comisso and L. Sironi. Particle Acceleration in Relativistic Plasma Turbulence. *Phys. Rev. Lett.*, 121(25):255101, Dec. 2018. doi: 10.1103/PhysRevLett.121.255101.
- R. Courant, K. Friedrichs, and H. Lewy. Über die partiellen Differenzgleichungen der mathematischen Physik. *Mathematische Annalen*, 100:32–74, Jan. 1928. doi: 10.1007/BF01448839.
- T. J. L. Courvoisier. *High Energy Astrophysics*. 2013. doi: 10.1007/978-3-642-30970-0.
- J. Davelaar, A. A. Philippov, O. Bromberg, and C. B. Singh. Particle Acceleration in Kink-unstable Jets. *ApJL*, 896(2):L31, June 2020. doi: 10.3847/2041-8213/ab95a2.
- O. C. de Jager, A. K. Harding, P. F. Michelson, H. I. Nel, P. L. Nolan, P. Sreekumar, and D. J. Thompson. Gamma-Ray Observations of the Crab Nebula: A Study of the Synchro-Compton Spectrum. *ApJ*, 457:253, Jan. 1996. doi: 10.1086/176726.
- W. H. de Vries, R. H. Becker, and R. L. White. Double-Lobed Radio Quasars from the Sloan Digital Sky Survey. *The Astronomical Journal*, 131(2):666–679, Feb. 2006. doi: 10.1086/499303.
- L. Di Gesu, F. Tavecchio, I. Donnarumma, A. Marscher, M. Pesce-Rollins, and M. Landoni. Testing particle acceleration models for BL LAC jets with the Imaging X-ray Polarimetry Explorer. *arXiv e-prints*, art. arXiv:2201.09597, Jan. 2022.
- J. F. Drake, M. Swisdak, H. Che, and M. A. Shay. Electron acceleration from contracting magnetic islands during reconnection. *Nature*, 443(7111):553–556, Oct. 2006. doi: 10.1038/nature05116.
- L. O. Drury. REVIEW ARTICLE: An introduction to the theory of diffusive shock acceleration of energetic particles in tenuous plasmas. *Reports on Progress in Physics*, 46(8):973–1027, Aug. 1983. doi: 10.1088/0034-4885/46/8/002.
- T. Z. Esirkepov. Exact charge conservation scheme for Particle-in-Cell simulation with an arbitrary form-factor. *Computer Physics Communications*, 135(2):144–153, Apr. 2001. doi: 10.1016/S0010-4655(00)00228-9.
- B. L. Fanaroff and J. M. Riley. The morphology of extragalactic radio sources of high and low luminosity. *MNRAS*, 167:31P–36P, May 1974. doi: 10.1093/mnras/167.1.31P.

- E. Fermi. On the Origin of the Cosmic Radiation. *Physical Review*, 75(8):1169–1174, Apr. 1949. doi: 10.1103/PhysRev.75.1169.
- A. Ferrari, E. Trussoni, and L. Zaninetti. Magnetohydrodynamic instabilities and electron acceleration in extended extragalactic radio sources. *A&A*, 79(1-2):190–196, Oct. 1979.
- D. C. Gabuzda, É. Murray, and P. Cronin. Helical magnetic fields associated with the relativistic jets of four BL Lac objects. *MNRAS*, 351(9):L89–L93, July 2004. doi: 10.1111/j.1365-2966.2004.08037.x.
- G. Ghisellini and F. Tavecchio. Canonical high-power blazars. *MNRAS*, 397(2):985–1002, Aug. 2009. doi: 10.1111/j.1365-2966.2009.15007.x.
- G. Ghisellini, C. Righi, L. Costamante, and F. Tavecchio. The Fermi blazar sequence. *MNRAS*, 469(1):255–266, July 2017. doi: 10.1093/mnras/stx806.
- D. Giannios. Reconnection-driven plasmoids in blazars: fast flares on a slow envelope. *MNRAS*, 431(1):355–363, May 2013. doi: 10.1093/mnras/stt167.
- D. Giannios and H. C. Spruit. The role of kink instability in Poynting-flux dominated jets. *A&A*, 450(3):887–898, May 2006. doi: 10.1051/0004-6361:20054107.
- D. Giannios and D. A. Uzdensky. GRB and blazar jets shining through their stripes. *MNRAS*, 484(1):1378–1389, Mar. 2019. doi: 10.1093/mnras/stz082.
- D. Giannios, D. A. Uzdensky, and M. C. Begelman. Fast TeV variability in blazars: jets in a jet. *MNRAS*, 395(1):L29–L33, May 2009. doi: 10.1111/j.1745-3933.2009.00635.x.
- F. Guo, H. Li, W. Daughton, and Y.-H. Liu. Formation of Hard Power Laws in the Energetic Particle Spectra Resulting from Relativistic Magnetic Reconnection. *Phys. Rev. Lett.*, 113(15):155005, Oct. 2014. doi: 10.1103/PhysRevLett.113.155005.
- F. Guo et al. Efficient Production of High-energy Nonthermal Particles during Magnetic Reconnection in a Magnetically Dominated Ion-Electron Plasma. *ApJL*, 818(1):L9, Feb. 2016. doi: 10.3847/2041-8205/818/1/L9.
- H. Hakobyan, A. Philippov, and A. Spitkovsky. Effects of Synchrotron Cooling and Pair Production on Collisionless Relativistic Reconnection. *ApJ*, 877(1):53, May 2019. doi: 10.3847/1538-4357/ab191b.
- E. G. Harris. On a plasma sheath separating regions of oppositely directed magnetic field. *Il Nuovo Cimento*, 23(1):115–121, Jan. 1962. doi: 10.1007/BF02733547.
- M. Hayashida et al. The Structure and Emission Model of the Relativistic Jet in the Quasar 3C 279 Inferred from Radio to High-energy γ -Ray Observations in 2008-2010. *ApJ*, 754(2):114, Aug. 2012. doi: 10.1088/0004-637X/754/2/114.
- D. N. Hosking and L. Sironi. A First-principle Model for Polarization Swings during Reconnection-powered Flares. *ApJL*, 900(2):L23, Sept. 2020. doi: 10.3847/2041-8213/abafa6.

- T. Hovatta, M. L. Lister, M. F. Aller, H. D. Aller, D. C. Homan, Y. Y. Kovalev, A. B. Pushkarev, and T. Savolainen. MOJAVE: Monitoring of Jets in Active Galactic Nuclei with VLBA Experiments. VIII. Faraday Rotation in Parsec-scale AGN Jets. *The Astronomical Journal*, 144(4):105, Oct. 2012. doi: 10.1088/0004-6256/144/4/105.
- J. D. Jackson. *Classical Electrodynamics, 3rd Edition*. 1998.
- L. H. S. Kadowaki, E. M. de Gouveia Dal Pino, T. E. Medina-Torrejón, Y. Mizuno, and P. Kushwaha. Fast Magnetic Reconnection Structures in Poynting Flux-dominated Jets. *ApJ*, 912(2):109, May 2021. doi: 10.3847/1538-4357/abee7a.
- K. I. Kellermann, J. J. Condon, A. E. Kimball, R. A. Perley, and Ž. Ivezić. Radio-loud and Radio-quiet QSOs. *ApJ*, 831(2):168, Nov. 2016. doi: 10.3847/0004-637X/831/2/168.
- J. Y. Kim, T. P. Krichbaum, A. P. Marscher, S. G. Jorstad, I. Agudo, C. Thum, J. A. Hodgson, N. R. MacDonald, E. Ros, R. S. Lu, M. Bremer, P. de Vicente, M. Lindqvist, S. Trippe, and J. A. Zensus. Spatially resolved origin of millimeter-wave linear polarization in the nuclear region of 3C 84. *A&A*, 622:A196, Feb. 2019. doi: 10.1051/0004-6361/201832920.
- J. G. Kirk and O. Skjæraasen. Dissipation in Poynting-Flux-dominated Flows: The σ -Problem of the Crab Pulsar Wind. *ApJ*, 591(1):366–379, July 2003. doi: 10.1086/375215.
- J. G. Kirk, F. M. Rieger, and A. Mastichiadis. Particle acceleration and synchrotron emission in blazar jets. *A&A*, 333:452–458, May 1998.
- Y. Y. Kovalev, A. B. Pushkarev, E. E. Nokhrina, A. V. Plavin, V. S. Beskin, A. V. Chernoglazov, M. L. Lister, and T. Savolainen. A transition from parabolic to conical shape as a common effect in nearby AGN jets. *MNRAS*, 495(4):3576–3591, July 2020. doi: 10.1093/mnras/staa1121.
- M. Kruskal and J. L. Tuck. The Instability of a Pinched Fluid with a Longitudinal Magnetic Field. *Proceedings of the Royal Society of London Series A*, 245(1241):222–237, June 1958. doi: 10.1098/rspa.1958.0079.
- R. M. Kulsrud. *Plasma physics for astrophysics*. 2005.
- J. P. Leahy and A. G. Williams. The bridges of classical double radio sources. *MNRAS*, 210:929–951, Oct. 1984. doi: 10.1093/mnras/210.4.929.
- A. Levinson. On the Origin of Rapid Flares in TeV Blazars. *ApJL*, 671(1):L29–L32, Dec. 2007. doi: 10.1086/524708.
- M. A. Liberman, J. S. De Groot, A. Toor, and R. B. Spielman. *Stability of Z-Pinch Plasmas*, pages 96–132. Springer New York, New York, NY, 1999. ISBN 978-1-4612-1424-3. doi: 10.1007/978-1-4612-1424-3_4. URL https://doi.org/10.1007/978-1-4612-1424-3_4.
- M. L. Lister, M. F. Aller, H. D. Aller, D. C. Homan, K. I. Kellermann, Y. Y. Kovalev, A. B. Pushkarev, J. L. Richards, E. Ros, and T. Savolainen. MOJAVE: XIII. Parsec-scale AGN Jet Kinematics Analysis Based on 19 years of VLBA Observations at 15 GHz. *The Astronomical Journal*, 152(1):12, July 2016. doi: 10.3847/0004-6256/152/1/12.

- Y.-H. Liu, P. Cassak, X. Li, M. Hesse, S.-C. Lin, and K. Genestreti. First-principles theory of the rate of magnetic reconnection in magnetospheric and solar plasmas. *Communications Physics*, 5(1):97, Dec. 2022. doi: 10.1038/s42005-022-00854-x.
- N. F. Loureiro, A. A. Schekochihin, and S. C. Cowley. Instability of current sheets and formation of plasmoid chains. *Physics of Plasmas*, 14(10):100703–100703, Oct. 2007. doi: 10.1063/1.2783986.
- N. F. Loureiro, R. Samtaney, A. A. Schekochihin, and D. A. Uzdensky. Magnetic reconnection and stochastic plasmoid chains in high-Lundquist-number plasmas. *Physics of Plasmas*, 19(4):042303–042303, Apr. 2012. doi: 10.1063/1.3703318.
- Y. E. Lyubarsky. On the relativistic magnetic reconnection. *MNRAS*, 358(1):113–119, Mar. 2005. doi: 10.1111/j.1365-2966.2005.08767.x.
- G. G. Madejski and M. Sikora. Gamma-Ray Observations of Active Galactic Nuclei. *Annual Review of Astronomy and Astrophysics*, 54:725–760, Sept. 2016. doi: 10.1146/annurev-astro-081913-040044.
- L. Maraschi, G. Ghisellini, and A. Celotti. A Jet Model for the Gamma-Ray-emitting Blazar 3C 279. *ApJL*, 397:L5, Sept. 1992. doi: 10.1086/186531.
- I. Martí-Vidal, S. Muller, W. Vlemmings, C. Horellou, and S. Aalto. A strong magnetic field in the jet base of a supermassive black hole. *Science*, 348(6232):311–314, Apr. 2015. doi: 10.1126/science.aaa1784.
- Y. Mizuno, P. E. Hardee, and K.-I. Nishikawa. Three-dimensional Relativistic Magnetohydrodynamic Simulations of Current-driven Instability with a Sub-Alfvénic Jet: Temporal Properties. *ApJ*, 734(1):19, June 2011. doi: 10.1088/0004-637X/734/1/19.
- Y. Mizuno, Y. Lyubarsky, K.-I. Nishikawa, and P. E. Hardee. Three-dimensional Relativistic Magnetohydrodynamic Simulations of Current-driven Instability. III. Rotating Relativistic Jets. *ApJ*, 757(1):16, Sept. 2012. doi: 10.1088/0004-637X/757/1/16.
- P. J. Morris, W. J. Potter, and G. Cotter. The feasibility of magnetic reconnection powered blazar flares from synchrotron self-Compton emission. *MNRAS*, 486(2):1548–1562, June 2019. doi: 10.1093/mnras/stz920.
- K. Nalewajko, D. Giannios, M. C. Begelman, D. A. Uzdensky, and M. Sikora. Radiative properties of reconnection-powered minijets in blazars. *MNRAS*, 413(1):333–346, May 2011. doi: 10.1111/j.1365-2966.2010.18140.x.
- K. Nalewajko, D. A. Uzdensky, B. Cerutti, G. R. Werner, and M. C. Begelman. On the Distribution of Particle Acceleration Sites in Plasmoid-dominated Relativistic Magnetic Reconnection. *ApJ*, 815(2):101, Dec. 2015. doi: 10.1088/0004-637X/815/2/101.
- K. Nalewajko, Y. Yuan, and M. Chruślińska. Kinetic simulations of relativistic magnetic reconnection with synchrotron and inverse Compton cooling. *Journal of Plasma Physics*, 84(3):755840301, June 2018. doi: 10.1017/S0022377818000624.

- J. Niemiec and M. Ostrowski. Cosmic-Ray Acceleration at Relativistic Shock Waves with a “Realistic” Magnetic Field Structure. *ApJ*, 610(2):851–867, Aug. 2004. doi: 10.1086/421730.
- J. Ortuño-Macías and K. Nalewajko. Radiative kinetic simulations of steady-state relativistic plasmoid magnetic reconnection. *MNRAS*, 497(2):1365–1381, Sept. 2020. doi: 10.1093/mnras/staa1899.
- J. Ortuño-Macías, K. Nalewajko, D. A. Uzdensky, M. C. Begelman, G. R. Werner, A. Y. Chen, and B. Mishra. Kinetic Simulations of Instabilities and Particle Acceleration in Cylindrical Magnetized Relativistic Jets. *ApJ*, 931(2):137, June 2022. doi: 10.3847/1538-4357/ac6acd.
- E. N. Parker. Sweet’s Mechanism for Merging Magnetic Fields in Conducting Fluids. *Journal of Geophysical Research*, 62(4):509–520, Dec. 1957. doi: 10.1029/JZ062i004p00509.
- A. Pasetto et al. Reading M87’s DNA: A Double Helix Revealing a Large-scale Helical Magnetic Field. *ApJL*, 923(1):L5, Dec. 2021. doi: 10.3847/2041-8213/ac3a88.
- E. S. Perlman et al. Optical Polarimetry of the Jets of Nearby Radio Galaxies. I. The Data. *ApJ*, 651(2):735–748, Nov. 2006. doi: 10.1086/506587.
- M. Petropoulou and L. Sironi. The steady growth of the high-energy spectral cut-off in relativistic magnetic reconnection. *MNRAS*, 481(4):5687–5701, Dec. 2018. doi: 10.1093/mnras/sty2702.
- M. Petropoulou, S. Dimitrakoudis, P. Padovani, A. Mastichiadis, and E. Resconi. Photohadronic origin of γ -ray BL Lac emission: implications for IceCube neutrinos. *MNRAS*, 448(3):2412–2429, Apr. 2015. doi: 10.1093/mnras/stv179.
- M. Petropoulou, D. Giannios, and L. Sironi. Blazar flares powered by plasmoids in relativistic reconnection. *MNRAS*, 462(3):3325–3343, Nov. 2016. doi: 10.1093/mnras/stw1832.
- M. Petropoulou, L. Sironi, A. Spitkovsky, and D. Giannios. Relativistic Magnetic Reconnection in Electron-Positron-Proton Plasmas: Implications for Jets of Active Galactic Nuclei. *ApJ*, 880(1):37, July 2019. doi: 10.3847/1538-4357/ab287a.
- V. Petrosian. Stochastic Acceleration by Turbulence. *Space Science Reviews*, 173(1-4):535–556, Nov. 2012. doi: 10.1007/s11214-012-9900-6.
- H. E. Petschek. Magnetic Field Annihilation. In *NASA Special Publication*, volume 50, page 425. 1964.
- T. Piran. The physics of gamma-ray bursts. *Reviews of Modern Physics*, 76(4):1143–1210, Oct. 2004. doi: 10.1103/RevModPhys.76.1143.
- W. J. Potter and G. Cotter. Synchrotron and inverse-Compton emission from blazar jets - I. A uniform conical jet model. *MNRAS*, 423(1):756–765, June 2012. doi: 10.1111/j.1365-2966.2012.20918.x.
- P. L. Pritchett. Particle-in-Cell Simulation of Plasmas - A Tutorial. In J. Büchner, C. Dum, and M. Scholer, editors, *Space Plasma Simulation*, volume 615, pages 1–24. 2003.
- A. B. Pushkarev, Y. Y. Kovalev, M. L. Lister, and T. Savolainen. MOJAVE - XIV. Shapes and opening angles of AGN jets. *MNRAS*, 468(4):4992–5003, July 2017. doi: 10.1093/mnras/stx854.

- P. Rani, C. S. Stalin, and S. Rakshit. X-ray flux variability of active galactic nuclei observed using NuSTAR. *MNRAS*, 466(3):3309–3322, Apr. 2017. doi: 10.1093/mnras/stw3228.
- M. J. Rees. The M87 jet: internal shocks in a plasma beam? *MNRAS*, 184:61P–65P, Sept. 1978. doi: 10.1093/mnras/184.1.61P.
- G. B. Rybicki and A. P. Lightman. *Radiative processes in astrophysics*. 1979.
- A. A. Schekochihin. *Lectures on Kinetic Theory and Magnetohydrodynamics of Plasmas*. Jan. 2020.
- K. M. Schoeffler, T. Grismayer, D. Uzdensky, R. A. Fonseca, and L. O. Silva. Bright Gamma-Ray Flares Powered by Magnetic Reconnection in QED-strength Magnetic Fields. *ApJ*, 870(1):49, Jan. 2019. doi: 10.3847/1538-4357/aaf1b9.
- M. Sikora, M. C. Begelman, and M. J. Rees. Comptonization of Diffuse Ambient Radiation by a Relativistic Jet: The Source of Gamma Rays from Blazars? *ApJ*, 421:153, Jan. 1994. doi: 10.1086/173633.
- M. Sikora, M. C. Begelman, G. M. Madejski, and J.-P. Lasota. Are Quasar Jets Dominated by Poynting Flux? *ApJ*, 625(1):72–77, May 2005. doi: 10.1086/429314.
- M. Sikora, Ł. Stawarz, R. Moderski, K. Nalewajko, and G. M. Madejski. Constraining Emission Models of Luminous Blazar Sources. *ApJ*, 704(1):38–50, Oct. 2009. doi: 10.1088/0004-637X/704/1/38.
- L. Sironi and A. Spitkovsky. Particle Acceleration in Relativistic Magnetized Collisionless Electron-Ion Shocks. *ApJ*, 726(2):75, Jan. 2011. doi: 10.1088/0004-637X/726/2/75.
- L. Sironi and A. Spitkovsky. Relativistic Reconnection: An Efficient Source of Non-thermal Particles. *ApJL*, 783(1):L21, Mar. 2014. doi: 10.1088/2041-8205/783/1/L21.
- L. Sironi, A. Spitkovsky, and J. Arons. The Maximum Energy of Accelerated Particles in Relativistic Collisionless Shocks. *ApJ*, 771(1):54, July 2013. doi: 10.1088/0004-637X/771/1/54.
- L. Sironi, M. Petropoulou, and D. Giannios. Relativistic jets shine through shocks or magnetic reconnection? *MNRAS*, 450(1):183–191, June 2015. doi: 10.1093/mnras/stv641.
- L. Sironi, D. Giannios, and M. Petropoulou. Plasmoids in relativistic reconnection, from birth to adulthood: first they grow, then they go. *MNRAS*, 462(1):48–74, Oct. 2016. doi: 10.1093/mnras/stw1620.
- L. Sironi, M. E. Rowan, and R. Narayan. Reconnection-driven Particle Acceleration in Relativistic Shear Flows. *ApJL*, 907(2):L44, Feb. 2021. doi: 10.3847/2041-8213/abd9bc.
- M. D. Smith. *Astrophysical Jets and Beams*. 2012.
- A. Spitkovsky. Simulations of relativistic collisionless shocks: shock structure and particle acceleration. In T. Bulik, B. Rudak, and G. Madejski, editors, *Astrophysical Sources of High Energy Particles and Radiation*, volume 801 of *American Institute of Physics Conference Series*, pages 345–350, Nov. 2005. doi: 10.1063/1.2141897.

- H. C. Spruit, F. Daigne, and G. Drenkhahn. Large scale magnetic fields and their dissipation in GRB fireballs. *A&A*, 369:694–705, Apr. 2001. doi: 10.1051/0004-6361:20010131.
- L. Stawarz and M. Ostrowski. Radiation from the Relativistic Jet: A Role of the Shear Boundary Layer. *ApJ*, 578(2):763–774, Oct. 2002. doi: 10.1086/342649.
- P. A. Sweet. The Neutral Point Theory of Solar Flares. In B. Lehnert, editor, *Electromagnetic Phenomena in Cosmical Physics*, volume 6, page 123, Jan. 1958.
- M. Takamoto. Evolution of Relativistic Plasmoid Chains in a Poynting-dominated Plasma. *ApJ*, 775(1):50, Sept. 2013. doi: 10.1088/0004-637X/775/1/50.
- A. Tchekhovskoy and O. Bromberg. Three-dimensional relativistic MHD simulations of active galactic nuclei jets: magnetic kink instability and Fanaroff-Riley dichotomy. *MNRAS*, 461(1):L46–L50, Sept. 2016. doi: 10.1093/mnrasl/slw064.
- C. M. Urry and P. Padovani. Unified Schemes for Radio-Loud Active Galactic Nuclei. *Publications of the Astronomical Society of the Pacific*, 107:803, Sept. 1995. doi: 10.1086/133630.
- R. C. Walker, P. E. Hardee, F. B. Davies, C. Ly, and W. Junor. The Structure and Dynamics of the Subparsec Jet in M87 Based on 50 VLBA Observations over 17 Years at 43 GHz. *ApJ*, 855(2):128, Mar. 2018. doi: 10.3847/1538-4357/aaafcc.
- J. Wardle. The Variable Rotation Measure Distribution in 3C 273 on Parsec Scales. *Galaxies*, 6(1):5, Jan. 2018. doi: 10.3390/galaxies6010005.
- G. R. Werner and D. A. Uzdensky. Nonthermal Particle Acceleration in 3D Relativistic Magnetic Reconnection in Pair Plasma. *ApJL*, 843(2):L27, July 2017. doi: 10.3847/2041-8213/aa7892.
- G. R. Werner, D. A. Uzdensky, B. Cerutti, K. Nalewajko, and M. C. Begelman. The Extent of Power-law Energy Spectra in Collisionless Relativistic Magnetic Reconnection in Pair Plasmas. *ApJL*, 816(1):L8, Jan. 2016. doi: 10.3847/2041-8205/816/1/L8.
- G. R. Werner, D. A. Uzdensky, M. C. Begelman, B. Cerutti, and K. Nalewajko. Non-thermal particle acceleration in collisionless relativistic electron-proton reconnection. *MNRAS*, 473(4):4840–4861, Feb. 2018. doi: 10.1093/mnras/stx2530.
- K. Yee. Numerical solution of initial boundary value problems involving maxwell’s equations in isotropic media. *IEEE Transactions on Antennas and Propagation*, 14(3):302–307, May 1966. doi: 10.1109/TAP.1966.1138693.
- Y. Yuan, K. Nalewajko, J. Zrake, W. E. East, and R. D. Blandford. Kinetic Study of Radiation-reaction-limited Particle Acceleration During the Relaxation of Unstable Force-free Equilibria. *ApJ*, 828(2):92, Sept. 2016. doi: 10.3847/0004-637X/828/2/92.
- R. T. Zavala and G. B. Taylor. A View through Faraday’s Fog. II. Parsec-Scale Rotation Measures in 40 Active Galactic Nuclei. *ApJ*, 612(2):749–779, Sept. 2004. doi: 10.1086/422741.

- A. A. Zdziarski and M. Bottcher. Hadronic models of blazars require a change of the accretion paradigm. *MNRAS*, 450:L21–L25, June 2015. doi: 10.1093/mnrasl/slv039.
- H. Zhang, X. Li, F. Guo, and D. Giannios. Large-amplitude Blazar Polarization Angle Swing as a Signature of Magnetic Reconnection. *ApJL*, 862(2):L25, Aug. 2018. doi: 10.3847/2041-8213/aad54f.
- H. Zhang, L. Sironi, and D. Giannios. Fast Particle Acceleration in Three-dimensional Relativistic Reconnection. *ApJ*, 922(2):261, Dec. 2021. doi: 10.3847/1538-4357/ac2e08.
- E. G. Zweibel and M. Yamada. Magnetic Reconnection in Astrophysical and Laboratory Plasmas. *Annual Review of Astronomy and Astrophysics*, 47(1):291–332, Sept. 2009. doi: 10.1146/annurev-astro-082708-101726.